Università degli Studi di Trieste

XXVI Ciclo del Dottorato di ricerca in
Environmental and Industrial Fluid Mechanics

A Numerical Framework of Multiple Phase Cloud Microphysics in Regional and Global Atmospheric Models

Settore scientifico-disciplinare: FIS/06

Ph.D. Student:	Rita Nogherotto
Ph.D. Program Director:	Prof. Vincenzo Armenio
Thesis Supervisor:	Dr. Adrian Mark Tompkins

Academic Year 2013–2014

"It's a strange kind of beauty,
It's cold and austere,
And whatever it was that ye've done to be here,
It's the sum of yr hopes yr despairs and yr fears,
When the last ship sails."
Thomas Sumner *The last ship*

Abstract

The Regional Climate Model RegCM4 (Giorgi et al., 2012) treats nonconvective clouds and precipitation following the Subgrid Explicit SUBEX parameterization (Pal et al., 2000). This scheme includes a simple representation for the formation of raindrops and solves diagnostically the precipitation: rain forms when the cloud water content exceeds the autoconversion threshold, that is an increasing function of the temperature and assumes different values over the land and over the ocean to account for the difference in number of the cloud condensation nuclei over continental and oceanic regions. The SUBEX scheme does not account for the presence of clouds ice, and the fraction of ice is diagnosed as a function of temperature in the radiation scheme. Due to the increasing emphasis on cloud representations in the climate community and the forthcoming increasing resolution due to the inclusion, in the close future, of a non-hydrostatic compressible core, the treatment of the ice microphysics and a prognostic representation of the precipitation is required in RegCM4. This thesis presents the new parameterization for stratiform cloud microphysics and precipitation implemented in RegCM4. The approach of the new parameterization is based on an implicit numerical framework recently developed and implemented into the ECMWF operational forecasting model (Tiedtke, 1993). The new parameterization solves 5 prognostic equations for the water vapour, the liquid water, the rain, the ice and the snow mixing ratios. It allows a proper treatment of mixed-phase clouds and a more physically realistic representation of the precipitation as it is no more an instantaneous response to the microphysical processes occurring in clouds and is subjected to the horizontal advection. A first discussion of the results contains an evaluation of the vertical distributions of the main microphysical quantities, such as the liquid

and ice water mixing ratios and the relative fractions. It also presents a series of sensitivity tests to understand how the moisture and radiation quantities respond to the variation of the microphysical parameters used in the scheme, such as the fall speeds of the falling categories, the autoconversion scheme and the evaporation coefficient. Cloud properties are afterwards evaluated through the implementation for RegCM4 of the new cloud evaluation COSP tool (Bodas-Salcedo et al., 2011), developed by the Cloud Feedback Model Intercomparison Project (CFMIP), that facilitates the comparison of simulated clouds with observations from passive and active remote sensing by diagnosing from model outputs the quantities that would be observed from satellites if they were flying above an atmosphere similar to that predicted by the model. Different hypothesis are presented to explain the reasons for RegCM4 biases in representing different types of clouds over the tropical band and new prospectives for the future investigations designed to answer to the open questions are outlined.

Contents

Introduction

The scientific assessment on the possible effects of CO_2 on climate, released by Charney et al. (1979), represents an early modelling investigation that aimed to estimate the increase of the carbon dioxide by the end of the 21^{st} Century and its effects on the global mean surface temperature. Charney estimated that the CO_2 concentration would double and the temperature would increase approximately of 3°C with larger increases at higher latitudes. Charney summarised the main contributors to the predicted warming and also noted the important role of radiative feedback in the existence of large inter-model uncertainties in projections of future climate change.
The four most important radiative feedbacks observed can be listed as follows:

- Water vapour feedback: it represents the most consistently important feedback accounting for the warming predicted by general circulation models in response to a doubling of CO_2. As the atmosphere gets warmer, the saturation vapour pressure increases and the amount of water vapour will tend to increase. Being the water vapour a greenhouse gas, its increase will cause additional warming. This is an example of what is called "positive feedback".

- Temperature lapse rate feedback: models predict enhanced warming in the upper tropical troposphere in response to an increase in the concentration of greenhouse gases. This would lead to a reduction of the tropical temperature lapse rate, and thus to an increase of the outgoing longwave radiation. The system will therefore tend to lose more energy, so inducing a negative feedback. At mid and high latitudes a larger low level warming is projected, providing a positive feedback due to an

increase of the downward longwave radiation. The two effects are opposite but in average the influence of the tropics dominates, leading to a negative feedback.

- Cloud feedback: clouds can create both positive and negative feedback. In a warmer atmosphere, an increase of low clouds and a decrease of high clouds would lead to a cooling (negative feedback), while an increase of high clouds and a decrease of low clouds would lead to a warming (positive feedback). It is necessary to know how the clouds will evolve in order to establish the overall effect. Models do not agree in the intensity or even in the sign of the cloud feedback (Dufresne and Bony, 2008; Cess et al., 1996).
- Surface albedo feedback: a warmer atmosphere would lead to the melting of the ice caps, implying a decrease of the reflection at the surface and thus to a even warmer atmosphere. Overall this is a positive feedback.

The past three decades have seen growing interest in trying to infer the future climatic change associated with the projected increases in the concentration of greenhouse gases by means of three-dimensional general circulation models (GCMs). Nowadays climate models exhibit a wide range of values for the radiative feedbacks and for the climate sensitivities (Andrews et al., 012b). For a doubling of carbon dioxide, models predict a range of different warming scenarios that are proportional to the radiative feedbacks that enforce as temperature increases (Zelinka et al., 2013).
Dufresne and Bony (2008) investigate how much the main atmospheric radiative feedbacks contribute to a multi-model mean and spread of global warming estimates, by imposing to the climate system a radiative forcing, such as the change in the greenhouse gas concentration. They hence analyse the change of surface temperature ΔT_s in response to the radiative forcing imposed predicted by an ensemble of 12 coupled atmosphere-ocean GCMs participating in the Cloud Model Intercomparison Project CMIP3/Intergovernamental Panel on Climate Change (IPCC) Fourth Assessment Report (AR4) (Meehl et al., 2004; Randall et al., 2007). Figure 1 shows that each model responds differently to the forcing, and the difference is more pronounced for the cloud feedback contribution: the inter-model standard deviation of the total temperature change due to cloud feedbacks represents the 70% of the standard

deviation of the total temperature change. Cloud feedbacks therefore constitute the primary source of uncertainty for present climate sensitivity estimates. Despite the increases in computing power, the wide range of temporal and spatial scales involving cloud processes still require parameterizations to allow a proper representation of clouds in current GCMs and RCMs.

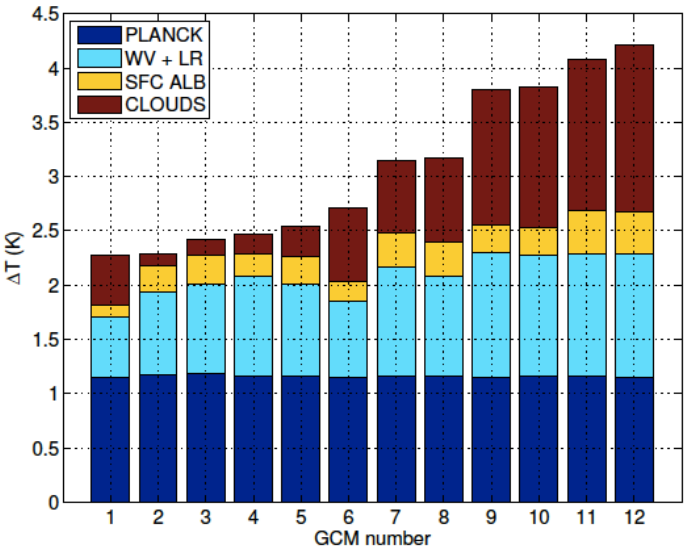

Figure 1: Equilibrium temperature change associated with the Planck response and the various feedbacks, computed for 12 CMIP3/AR4 AOGCMs for a 2×CO2 forcing of reference (3.71W m^2). The GCMs are sorted according to ΔT_s. Source: Dufresne and Bony (2008).

Randall et al. (2007) show that most of the spread in model-based estimates of equilibrium climate sensitivity is owed to differences in the response of low clouds and this result holds in the Cloud Model Intercomparison Project CMIP5 models (Vial et al., 2013). The spread is usually associated to how shallow cumulus and stratocumulus clouds (Williams and Tselioudis, 2007; Williams and Webb, 2009) are parameterized in GCMs. The large grid spacing of climate models, indeed, requires the use of parameterizations to reproduce the subgrid processes. Convective clouds are represented by convective parameterizations, which mostly focus on the dynamics and treat the microphysics in a very simple way. Stratiform clouds are represented by the microphysics parameterizations, which focus more on a detailed treatment of the microphysics through the prediction of one or more species of cloud water. The prediction can be implemented either by solving a *prognostic* equation, i.e. an

equation that contains time derivatives, or by simply deducing a variable from the prognostic variables or solving what is called a *diagnostic* equation, i.e. an equation that does not involve time change.
Simpler microphysics schemes treat the cloud water prognostically and diagnose the precipitating water (e.g. Rotstayn, 1997; Pal et al., 2000). The amount of cloud ice is also diagnosed from the cloud water as a function of temperature (e.g. DelGenio et al., 1996). Complex microphysics schemes treat separately the cold and the warm cloud by solving prognostic equations for liquid and ice (e.g. Fowler et al., 1996; Lohmann and Roeckner, 1996). A prognostic treatment of ice and liquid is highly advantageous because they undergo different microphysical and thermodynamical processes, precipitate with different fall speeds and have different optical properties.

The regional climate model RegCM is an hydrostatic, compressible, sigma-p vertical coordinate model, originally developed at the National Center for Atmospheric Research (NCAR), and now under development at the International Centre for Theoretical Physics (ICTP) in Trieste (for a detailed description of the model and of its parameterizations the reader is referred to Appendix A). The large scale and precipitation scheme implemented in the model is based on the Subgrid Explicit Moisture Scheme SUBEX parameterization of Pal et al. (2000). The scheme includes a simple representation for the formation of raindrops and solves diagnostically the precipitation: rain forms when the cloud water content exceeds the autoconversion threshold, that is an increasing function of the temperature and assumes different values over the land and over the ocean to account for the difference in number of the cloud condensation nuclei over continental and oceanic regions. The scheme does not account for the presence of clouds ice, and the fraction of ice is diagnosed as a function of temperature in the radiation scheme. Due to the increasing emphasis on cloud representations in the climate community and the forthcoming increasing resolution due to the inclusion, in the close future, of a non-hydrostatic compressible core, the treatment of the ice microphysics and a prognostic representation of the precipitation is required in RegCM.
In this thesis the new parameterization for stratiform cloud microphysics and precipitation is described, that solves 5 prognostic equations for the water vapour, the liquid water, the rain, the ice and the snow mixing ratios.
The new parameterization seeks the following:

- a separate treatment of cold and warm clouds, allowing to reproduce mixed-phase clouds and thus a more physically realistic representation of precipitation;
- a flexible numerical framework that easily allows the addition of new variables keeping a reasonable level of simplicity and computational efficiency;
- a robust fully implicit numerical framework that allows the use of longer timesteps and thus to reduce the computational cost;
- a prognostic treatment of precipitating categories (rain, snow and ice) allowing them to be advected by the wind, removing the assumption in which there was an instantaneous response of surface precipitation to the microphysical processes occurring in clouds;

Chapter 1 provides an overview of the role played by clouds in the atmosphere-earth system, followed by the introduction of the concept of "cloud radiative forcing", and thus by a short analysis of the impact of clouds on the global radiative budget. The motivations that imply the use of parameterizations of clouds processes in General Circulation Models (GCMs) are then presented, followed by a brief history of cloud parameterizations, from the early schemes with a fixed geographical distribution of cloud fraction and cloud properties (in the 1960s) to the more recent two-moment prognostic schemes. The present large-scale cloud and precipitation scheme used in the regional climate model RegCM4 (described in the Appendix A) is explained, and the motivations for the implementation of a new scheme are outlined.
Chapter 2 gives a description of the cloud microphysics for both the warm and cold clouds. Concepts of homogeneous and heterogeneous nucleation are presented together with an overview of the processes that govern the formation of precipitation and that need to be parameterized in order to be represented by climate models.
Chapter 3 describes the numerics and the microphysics of the new large scale precipitation scheme, built upon the European Centre for Medium Weather Forecast's Integrated Forecast System (IFS) (Tiedtke, 1993; Tompkins, 2007).
Chapter 4 shows results of the new scheme and presents sensitivity studies to assess the importance of the choice of the parameterization's coefficients and of the fall speed of the precipitable categories.

A great deal of research has been conducted in the last decades into producing satellites retrievals of many variables, such as water vapour, cloud properties and atmospheric temperature to analyze the performance of the new cloud parameterization schemes. Validation, in fact, still constitutes an issue due to the scarcity of cloud observations until recently: aside from the International Cloud Climatology Project's data, available since 1983, most of the satellite observations are available since the beginning of the 2000s. Moreover, the definition of clouds differs among observations and between models and observations (e.g. models are able to predict clouds at any atmospheric level where condensation occurs, while satellites may not observe clouds overlapped by thick high clouds) and satellite sensors have limitations that are sources of uncertainties in the retrievals. With the aim of reducing ambiguities in the comparison between models and observations a new approach has been introduced: the development of satellite "simulators" that rewrite model outputs miming observational processes, including the knowns satellites biases. The first simulator to be developed was the International Satellite Cloud Climatology Project (ISCCP, Rossow and Schiffer (1999)) and has been extensively used to evaluate the performance of climate models in reproducing clouds (e.g. Klein and Jakob, 1999; Zhang et al., 2005). More recently the same approach has been applied to the active sensors, lidar and radar (e.g. Bodas-Salcedo et al., 2008; Chepfer et al., 2008), and to the Multiangle Imaging Spectroradiometer MISR (Marchand et al., 2010).

The Cloud Feedback Model Intercomparison Project has recently developed an integrated satellite simulator, the CFMIP Observation Simulator Package (COSP) that includes simulators for datasets produced by five different satellites. It reproduces what would be observed from space if satellites where flying above the atmosphere predicted by the model.

Chapter 5 introduces more in detail the COSP tool and provides an evaluation of the performance of RegCM4 and the new microphysics scheme in the representation of the horizontal and vertical distributions of clouds in the tropical rain band by means of the CALIPSO (Winker et al., 2010), MISR (Diner et al., 1998) , MODIS (King et al., 2003), ISCCP satellites simulators (Rossow and Schiffer, 1999).

Chapter 1

Clouds in Climate Models

1.1 Clouds and Climate

Clouds represent the main character in governing the weather and the climate of the Earth's atmosphere. As they cover almost the 60-70% of the planet at any given time, they influence the atmosphere-earth system in a large variety of weather phenomena:

- Radiation: clouds interact with solar and terrestrial radiative fluxes through reflection, absorption and emission processes. In order to quantify the influence of clouds on radiation, the cloud radiative forcing (CRF) is used, defined as the difference between total and clear-sky broadband fluxes, called the shortwave (SW) and longwave (LW) respectively (Ramanathan et al., 1989).
- Latent Heat: the latent heat released or absorbed, associated with the phase changes that occur inside clouds, is an important source of atmospheric energy that, for instance, is needed for storms, thunderstorms or hurricanes to form.
- Surface Hydrology: the precipitation generated in clouds determines the surface hydrology.

Clouds constitute an important regulator of the amount of solar energy absorbed by the earth-atmosphere system and of infrared energy radiated to space. They modulate the radiative energy exchange within the atmosphere by interacting with the short wave radiation coming from the sun and with the

long wave radiation emitted by the earth and by the atmosphere. The quantity used to define the amount of a cloud within the grid cell is the cloud cover fraction. The effect of the cloud cover on the short wave radiation depends on the optical thickness of the cloud and on the size and the phase of the particles. The effect on the long wave radiation depends on the temperature at the top of the cloud, which is a function of cloud height and on emissivity, also related to the optical thickness.

A technical report by London (1957) represents one of the early attempts to quantify the effect of clouds on the earth radiation's budget by comparing the radiative fluxes in overcasted conditions to those in clear-sky conditions: the difference between the two has been termed **cloud radiative forcing** (Ellis, 1978).

Before discussing the total cloud effect on the Earth's radiation budget, it seems appropriate to provide a brief description of the role played by different types of clouds:

- The high thin cirrus clouds are highly transparent to the shortwave radiation coming from the Sun and are opaque to the longwave infrared radiation coming from the Earth's surface that they absorb and then emit both out to space and back to the Earth's surface. Because cirrus clouds are cold, the energy radiated to outer space is much lower than it would be without them. The high thin cirrus clouds greenhouse forcing is therefore large and its effect results in warming the atmosphere.
- Low stratocumulus clouds are usually thicker than high cirrus clouds and they are not transparent to the shortwave radiation incoming from the sun. They therefore do not let much solar energy reach the Earth's surface but they reflect much of the solar energy back to space. Their impact on the top of the atmosphere (TOA) long wave radiation budget is on the other hand low (Ramanathan, 1987) because their temperature is approximately the same as the earth's surface temperature. They thus radiate at nearly the same intensity as the surface and do not greatly affect the infrared radiation emitted to space.
- Deep convective clouds tops are very high and cold, thereby the infrared energy radiated to the space is less than it would be in clear sky conditions.

London found that clouds have a net cooling effect on the climate system, reducing the net energy input during the spring and the summer seasons, with an annual average effect of 35 $W\ \mathrm{m}^{-2}$.
Further experiments (e.g. Budyko, 1969; Schneider, 1972; Ellis, 1978; Ramanathan, 1976; Hartmann et al., 1991; Bony et al., 1997), aiming to study the effects that clouds have on the TOA radiation budget, have confirmed a cooling of about 20 $W\mathrm{m}^{-2}$ (Ellis, 1978), larger over the oceans than over land. Most of these studies are based on the data furnished by the Earth Radiation Budget Experiment (ERBE Barkstrom and Smith, 1986).
Before analysing the radiative cloud forcing, some informations about the clouds radiative effects can be drawn from Figure 1.1, that shows the TOA annual mean net radiation balance from the ERBE experiment.

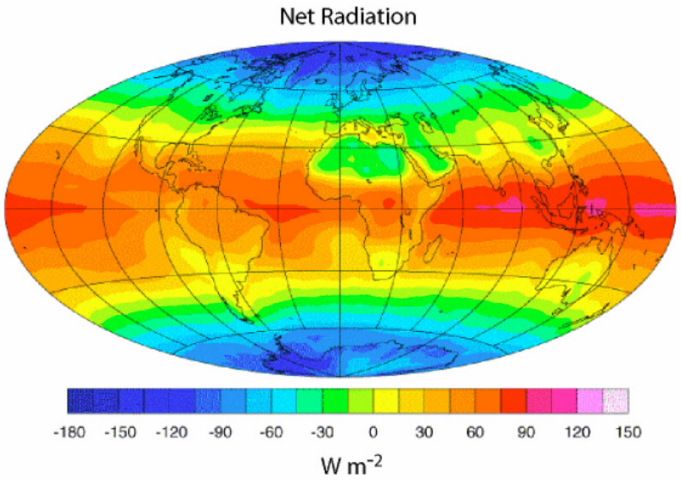

Figure 1.1: The annual mean TOA net radiation balance from the Earth Radiation Budget Experiment (ERBE), 1985-1986. Source: Graphic by D. Hartmann and M. Michelsen, University of Washington.

The figure shows that there is a latitudinal decrease of the net radiation from the equator towards the poles. This is due to the incoming SW solar radiation that is stronger on the equator respect to on the poles. It is also due to the temperature meridional gradient, affecting the LW budget, but to a lesser extent. By a more accurate analyses of the plot it is possible to notice that there is a deficit of radiation over the deserts, due to the high albedo that strongly reduces the incoming SW radiation. A deficit of radiation is seen also in the eastern sides of the Atlantic and Pacific oceans. This is where stratiform clouds

form, at the top of the convective planetary boundary layers PBL. These low clouds have a very high reflectivity, as previously highlighted and they thus reduce the SW incoming radiation while not having a strong impact on the LW budget.

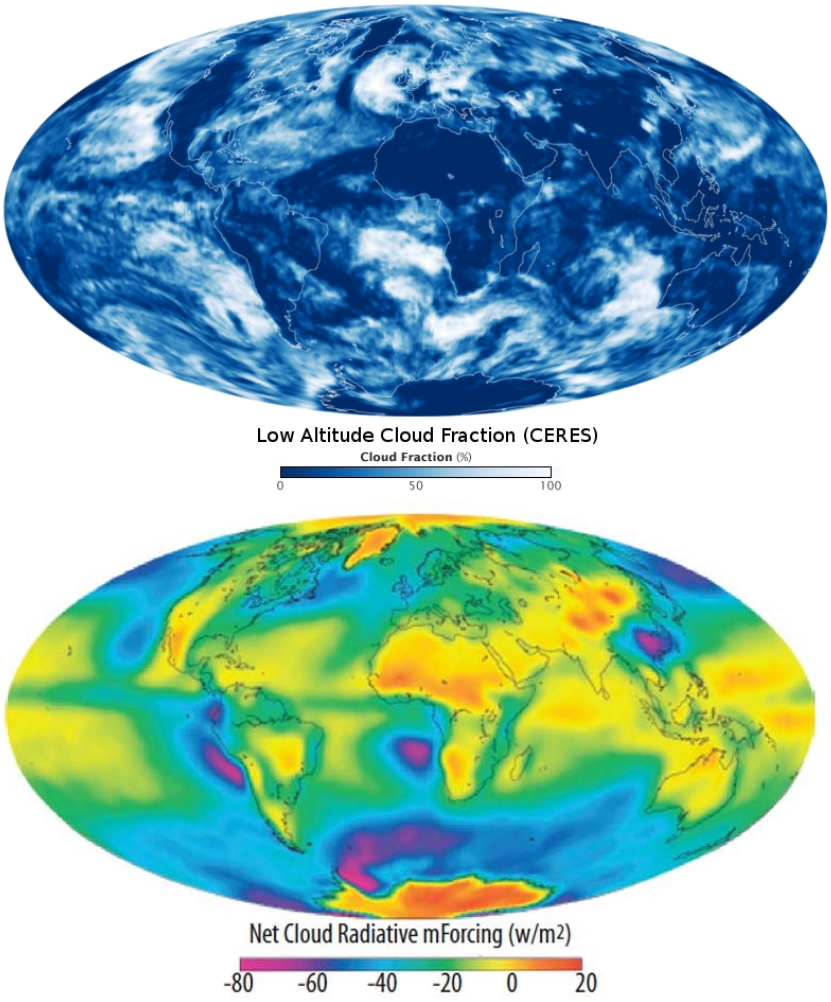

Figure 1.2: The top panel shows the the fractional area coverage by low clouds as measured by CERES sensors on NASA's Terra and Aqua satellites on December 2008. The bottom panel shows the TOA net radiative cloud forcing annually averaged from the Earth Radiation Budget Experiment (ERBE). Source: Graphic by D. Hartmann and M. Michelsen, University of Washington

The overall impact of clouds on the radiation budget is given by Figure 1.2 that compares the global distribution of low clouds (measured by CERES sensors on NASA's Terra and Aqua satellites) and the annually averaged net radiative cloud forcing (observed by ERBE). The results from ERBE indicate that in

the global mean clouds reduce the radiative heating of the planet, and that the cooling is a function of the season and ranges from approximately -14 to -21 Wm^{-2}. In the figure negative blue and violet colours indicate the area where the cooling is more pronounced. These areas are located at the eastern subtropical oceans, where stratocumulus clouds form in regions of large-scale subsidence. The close correspondence between the low clouds over the ocean and negative cloud forcing is clear from the figure.

1.2 Clouds and Climate Models

As previously highlighted, clouds are involved in several important and complex processes, strongly influencing the atmosphere-earth system. Therefore clouds need to be implemented in the atmospheric models used to predict the weather and the climate. The General Circulation Models (GCMs) solve the hydrodynamic equations that govern the atmospheric processes in discrete form after partitioning the atmosphere into grid cells of finite extent both in the horizontal and in the vertical directions. The discrete form of the continuous differential equations that describe the atmospheric motions can only represent processes on spatial scales of the order of twice the grid size. Clouds exist on a large range of both temporal and spatial scales. For example an individual small cumulus cloud's size is of the order of a few hundred meters in the horizontal and vertical and generally has a lifetime of less than an hour. On the other hand a cumulonimbus cloud may extend several thousands meters and can have a lifetime of several hours.
Cloud's processes range from the micro-scale (e.g. condensation and evaporation of individual cloud droplets), into the synoptic scale (e.g. clouds formation in frontal systems associated with mid-latitude baroclinic systems), but mostly cloud features are smaller than the grid size that can be afforded.
For this reason, describing accurately the intricate dynamic of the individual cloud would require either the use of a grid size of the order of meters (or even less, that would be computationally very expensive) or the representation of clouds subgrid processes with the use of a parameterization, expressing the description of those processes in terms of the grid scale. This technique finds the parameters that describe the statistical effect of the subgrid processes on the grid box-mean state. In order to guarantee a proper representation of the

effect that clouds have on the atmospheric dynamics the parameters commonly chosen are:

- the portion of the grid that is covered by the cloud (the cloud cover);
- the vertical extent of the cloud;
- the cloud moisture content;
- the sources and sinks of the cloud variables (such as evaporation, condensation, freezing, melting, etc);
- the amount of heat, moisture and momentum that is transferred through the advection.

A good treatment of clouds is, moreover, important for a good treatment of the radiation processes. For this reason a good cloud parameterization, in addition to properly describe the generation of the precipitation, needs to provide the radiation parameterization with an accurate knowledge of the effects of clouds on the radiative fluxes. Before going deeper into understanding properly how models deal with cloud processes, a brief history of the evolution of cloud parameterisations is presented.

1.3 Overview of the cloud parameterizations

Parameterizations of cloud processes are mainly divided into two groups:

- Convective clouds parameterizations, which focus on the representation of the redistribution of moisture and temperature in a grid column associated with the updraft and downdraft fluxes occurring within convective systems, and on the role of convection in drying and warming the large-scale atmospheric flow.

- Large-scale parameterizations, which treat those processes (mainly cloud formation and precipitation) that remove excess of moisture resulting from the dynamical fields resolved by the model (wind, temperature and moisture). One of the main role of this parameterization is to create the input to the radiation's budget calculation of the model.

Initially (**1960/70s**) the geographical distribution of cloud fraction and cloud optical properties was derived from zonal mean climatological values prescribed by early satellites or ground-base observations, like for example those of London (1957), and they were not varying in time (Smagorinsky et al., 1965; Holloway and Manabe, 1971). In these models clouds were having a role in influencing the climate only through effects on longwave and shortwave radiation, but their influence was considered to be small.
Later in the 70s the first diagnostic cloud parameterizations were implemented: models already included an evolution equation for humidity so that the only step forward was to insert a simple condensation scheme for which when the relative humidity was overtaking a saturation threshold, as previously suggested by Smagorinsky (1960), a condensate was formed and removed instantaneously as precipitation. Any occurring supersaturation was immediately readjusted back to saturation. Hence it was not clouds but precipitation that was assumed to form and thus there was no necessity of describing the microphysical processes.
Later in the **1970/80s**, thanks to the increasing computational power, the clouds radiative effects and the interaction of cloud processes with the other model variables started to be included in models (Charney et al., 1979; Somerville and Remer, 1984; Wetherald and Manabe, 1980).
Three mechanisms were identified by Randall et al. (1989) to describe the effects that clouds exert on the atmosphere: the *cloud radiative forcing* Ramanathan (1987), that describes how clouds interact with the radiative fluxes coming from the sun and from the Earth's surface, the *cloud latent forcing*, which concerns the impact of latent heat release and absorption on the precipitation, and finally the *cloud convective forcing*, which includes the transport of heat, moisture and momentum in convective clouds.
A new generation of cloud parameterizations started to diagnose cloud cover as a function of the relative humidity. These schemes are often referred to as **relative humidity schemes**. According to them if the grid-mean relative humidity exceeds a threshold, usually fixed to 80%, cloud starts to form. As soon as the RH reaches the saturation value of 100%, the entire grid is assumed to be covered by clouds. This new approach for the first time allowed the representation of subgrid-scale humidity. The relative humidity schemes are also referred to as the "diagnostic schemes", as the cloud cover and the amount of

condensate are derived diagnostically from the grid-averaged quantities.
The main credit of these schemes is that they have introduced a link in the description of cloud radiative and cloud latent heat forcing, that were previously treated by separate parameterization schemes.
The first to introduce a prognostic equation for cloud condensate was Sundqvist (1978), thus introducing the temporal and spatial variations of cloudiness due to microphysical processes. Diagnostic schemes started therefore to be gradually replaced by **prognostic schemes** during the **1980/1990s** with the introduction of simple descriptions of some intuitive parameterization for the mechanism for which rain droplets form on the account of cloud water (e.g. the processes of autoconversion and collection that will be discussed in the following chapters).
In contrast to the diagnostic approach, where clouds are considered to be a byproduct of other computed variables, the main advantages of using prognostic equations are that they represent the temporal evolution of clouds, allowing to storage the cloud water variables and thus giving a more realistic representation of their processes. Moreover computing prognostic falling species allows their horizontal and vertical advection, that is a required process when dealing with higher resolutions.

1.4 Parameterization of Clouds

1.4.1 The Cloud Cover

The cloud cover represents the fraction of the grid cell that is obscured by clouds. It is worth pointing out that a partial coverage of a grid-cell is only possible if a sub-grid variability in humidity and/or temperature exists.
As shown in Figure 1.3 if the cell is characterised by an homogeneous distribution of humidity and/or temperature, the cloud fraction is either one (i.e. in overcast conditions) or zero (i.e. in clear sky conditions). Because of their simplicity, these "all-or-nothing" parameterizations were mostly used in GCM models (Ose, 1993; Fowler et al., 1996) but are not appropriate for the spatial resolution they use.
Another problem of this approach is that when condensation occurs a new cloud is formed and the grid is filled in, but in the next time step the cloud

cover might be less than unity yielding an high-frequency “on-off” cloud activity. It is therefore more adequate to consider the partial coverage, so an inhomogeneous distribution of humidity and/or temperature.

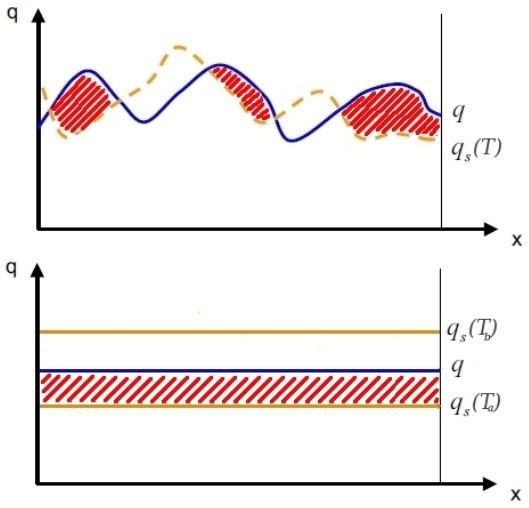

Figure 1.3: Schematics that illustrates in the upper plot an example of how subgrid fluctuations of water vapor q and/or of $q_s(T)$ allow the formation of partial coverage of the grid-cell. The bottom plot shows an uniform subgrid distribution of water vapor and the saturation mixing ratio for two different temperatures T_a and T_b that would respectively give rise to overcast conditions and clear sky conditions. Source: Tompkins (2005). Modified.

From Figure 1.3 it is clear that, in presence of humidity (and/or temperature) subgrid variability, if humidity exceeds the saturation value, and if it is assumed that no supersaturation with respect to water is considered (the excess of humidity is immediately converted into cloud), a partial cloud cover is associated with a mean-grid relative smaller than 1. This leads to positive correlation between the relative humidity RH and the cloud fraction C.
It is important to emphasise that all the schemes that are able to produce a partial coverage must make an assumption concerning the fluctuation of humidity and/or temperature on the subgrid-scale, and they can do it either implicitly, assuming knowledge about the time-mean statistics of the fluctuations (and they are called Relative Humidity Schemes), or explicitly, by specifying the probability density function for the total water at each grid cell (the so called "Statistical Schemes"). Relative humidity schemes (e.g. Sellers, 1976; Gates and Schlesinger, 1977; Sundqvist, 1978; Sundqvist et al., 1989; Slingo, 1980; DelGenio et al., 1996) define a diagnostic relationship between the cloud cover

and the relative humidity such that the cloud cover begins to increase monotonically from zero, at a critical value RH_{crit} at which cloud is assumed to form, until the clouds fills the entire grid box, at RH=1. This RH_{crit} represents a measure of the sub-grid variability and usually depends on the height, on the model resolution and on the cloud processes. Since these schemes form cloud when $RH < 100\%$, they implicitly assume subgrid-scale variability for the total water q_t.

Statistical Schemes, (Smith, 1990; Lohmann et al., 1999; Tompkins, 2002), directly represent the the Probability Density Function (PDF) of the total water mixing ratio. The cloud cover C is thus defined as the integral over the part of the PDF for which $q_t > q_s$. The cloud water content is calculated assuming the the number of cloud condensation nuclei (CCN) is sufficient to remove any supersaturation. Unfortunately the distribution functions are not known neither unique, so that the main task of the statistical schemes is the specification of the PDF and of its moments.

1.4.2 The vertical extension of clouds

As previously highlighted, a cloud parameterization has to provide the radiation parameterization with information regarding the cloud effects on the radiative budget. This is strictly related to how cloud layers are connected with respect to each other along the vertical. Cloud parameterizations have to make assumptions on how the spatial relationship among the cloud fractions of each layer. GCMs deal the overlapping problem mainly with three different approaches: the random overlap, the maximum overlap and the maximum-random overlap (see Figure 1.4).

In the maximum overlap assumption two clouds in adjacent layers overlap as much as possible. If $k = 1, 2, ..., kz$ is an index for the discrete vertical levels, from 1 at the top of the atmosphere to kz at the surface level, and letting C_k be the cloud fraction of layer k located between layers $k-1$ and $k+1$, the maximum overlap assumption gives:

$$C_k = \max(C_1, C_2, ..., C_{k-1}) \tag{1.1}$$

In the random overlap assumption all cloud layers are independent from each other, and the combine cloud fraction is given by:

$$C_k = 1 - \prod_{j=1,k-1} (1 - C_j) \tag{1.2}$$

In the maximum-random assumption the max-overlap is applied for adjacent layers while the random overlap for distant layers.

$$C_k = 1 - \prod_{j=1,k-1} \left(\frac{1 - \max(C_j, C_{j-1})}{1 - C_{j-1}} \right) \tag{1.3}$$

Different assumptions on the cloud overlap, as shown in Figure 1.4, lead to large differences in the resulting total cloud cover predicted by the models even if the cloud fraction at each level is the same.

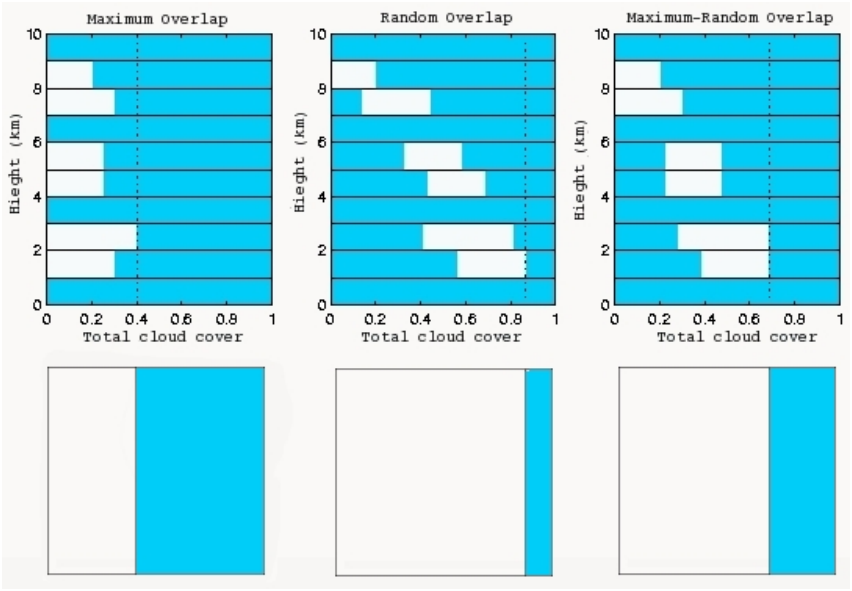

Figure 1.4: Schematics of the various cloud overlap assumptions. The clouds are shown as rectangular white blocks filling the vertical extent of a layer. The total cloud fraction from the top of the atmosphere down to a given level is given by the dotted line on the right and by the three plots at the bottom, showing the resulting grid cell total cloud cover. (Source: Hogan and Illingworth (2000). Modified.)

The example shown in the figure, for example, the random overlap assumption tends to produce a large total cloud cover, while the maximum overlap assumption tends to reduce it.

Hogan and Illingworth (2000), using high vertical resolution cloud radar data to study the overlap characteristics of clouds, found that vertically continuous clouds tend not to be maximally overlapped as most models assume and

the overlap of clouds at two levels tends to fall exponentially as their vertical separation is increased. They found that the overlap becomes random for separations greater than 4 km. They thus derived a new overlap assumption, the exponential-random overlap (EXP-RAN) , that is a combination of the max-random and the random overlap and that is a function of the level separation Δz. According to the exponential-random overlap the cloud cover C of layer k is given by:

$$C_k^{EXP-RAN} = \alpha\, C_k^{MAX-RAN} + (1-\alpha) C_k^{RAN} \tag{1.4}$$

where α is a overlap parameter defined as

$$\alpha = e^{\frac{\Delta z}{L}} \tag{1.5}$$

and L is a length scale called "decorrelation" distance estimated from observations.

Tompkins and Di Giuseppe (2007) extended the EXP-RAN scheme, to allow the large-scale models's radiation schemes to account for the apparent change of the cloud field geometry, on which shortwave radiative transfer depends, with the decreasing of the solar zenith angle (SZA). They thus introduces an adjustment factor K to account for the declining sun angle, such that the decorrelation distance L defined by Hogan and Illingworth (2000) is given by $L = KL_0$, where L_0 is the decorrelation distance for the sun overhead case.

1.4.3 The cloud microphysics

Cloud microphysics processes are those processes that control the formation of the cloud droplets and of the ice crystals, their growth and fallout as precipitation. Microphysics in clouds plays a key role in climate and weather models as it involves:

- the latent heating/cooling associated with the changes of phase (condensation, evaporation, deposition , sublimation , freezing, melting);
- the precipitation;
- the radiative transfer (absorption/emission of LW, reflection of SW);
- the cloud- aerosols-precipitation interactions.

Microphysics schemes can be separated into two groups according to the approach they use: the **bulk parameterization** schemes and the **spectral parameterization** schemes.
Spectral parameterization schemes (e.g. Stevens et al., 1996) describe each species of cloud hydrometeors (e.g. cloud droplets, rain droplets, ice crystals, graupel and hail) using a size distribution function containing several tens of bins of masses whose shape is prognosed during the model integration.
Bulk microphysical parameterization schemes predict several moments of the size distributions, rather than the distribution itself. The moments represent the bulk cloud characteristics such as the mass contents (e.g. the mixing ratios) and the concentration of the hydrometeors. Once predicted the bulk quantities they diagnose a functional form for the particle size distribution. Being computationally cheaper than the spectral schemes, the bulk schemes were initially developed to be used in mesoscale models (e.g. Lin et al., 1983) and they included prognostic equations for only one moment of the distribution, the mixing ratios of clouds species (e.g. cloud liquid, rain, ice, snow, hail) treating only the precipitation and evaporation/condensation processes. Later also implemented in climate models (Fowler et al., 1996; Lohmann et al., 1999), such schemes are referred to as "one-moment" schemes.
Schemes that predict also the concentration of the hydrometeors are referred to as "two-moments" schemes (e.g. Levkov et al., 1992; Meyers et al., 1997; Reisner et al., 1998; Morrison et al., 2005).

1.4.4 The Numerics: Explicit vs Implicit

Both explicit and implicit numerical methods are used in cloud parameterization schemes. The principal reason for using an implicit solution method, even if it is more complex and computationally more expensive, is that it allows the use of larger timesteps respect to those used in explicit solution methods. For explicit methods there is a limit on the size of the timestep used and their are therefore said to be conditionally stable. For implicit methods solutions exist for any size timestep and they are thus said to be unconditionally stable.

1.5 The SUBEX scheme used in RegCM4

This section provides a description of the large-scale cloud and precipitation scheme that is implemented in the Regional Climate Model RegCM4 (see Appendix A for the description of the model), that is based on the Subgrid Explicit Moisture Scheme SUBEX parameterization of Pal et al. (2000). A schematic of the structure of the scheme is provided in 1.5, showing that it calculates the contribution of water vapour and cloud liquid water through the evaporation and condensation processes, and includes a diagnostic formation of the raindrops (the shaded circle indicates a diagnostic variable while white circles indicate prognostic variables).
The scheme accounts for the sub grid variability by linking the average grid cell relative humidity to the cloud fraction following the work of Sundqvist et al. (1989) and includes a simple parameterization for the formation of the raindrops and for evaporation. Each model grid cell is divided into a clear sky and a cloud portion, and every variable V is the average of the values in the clear and in the cloudy part of the grid cell, V_{clr} and V_{cld} respectively, weighted by the cloud fraction C by the following relationship:

$$V = CV_{cld} + (1 - C)V_{clr} \tag{1.6}$$

At first the fraction C of the grid cell covered by clouds is calculated as a function of the local relative humidity RH, the relative humidity RH_{max} at which C reaches unity and the relative humidity at which the cloud begins to form RH_{min} according to :

$$C = 1 - \sqrt{\frac{RH_{max} - RH}{RH_{max} - RH_{min}}}, \tag{1.7}$$

$$RH_{min} = RH_{max} - \frac{(RH_{max} - RH)}{1 + 0.15 \cdot (T_0 - T)} \tag{1.8}$$

where $T_0 = 273.16K$. Typical values of RH_{min} range from 60% to 100%.

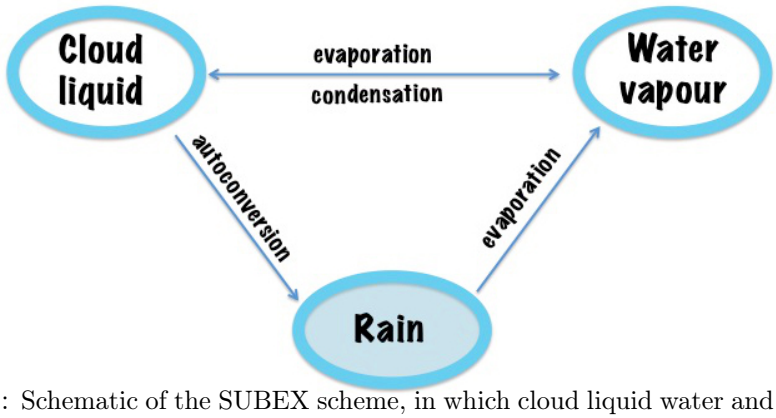

Figure 1.5: Schematic of the SUBEX scheme, in which cloud liquid water and water vapour were treated prognostically, while rain (in a shaded square) was diagnostically computed from the cloud liquid. The scheme was pretty simple and the ice and snow phases were not treated directly.

Where the cloud fraction C is different from zero, the cloud water content q_c is turned into precipitation P when greater than a threshold

$$q_c^{th} = c_{acs} \cdot 10^{-0.49+0.013T} \tag{1.9}$$

according to:

$$P = c_{ppt}\left(\frac{q_c}{C} - q_c^{th}\right) \tag{1.10}$$

where $\frac{1}{c_{ppt}}$ is the characteristic time for which cloud droplets are converted into raindrops and $\frac{q_c}{C}$ represents the in-cloud value value of q_c. Once precipitation is formed it is assumed to fall instantaneously.

There is no difference in the representation of the accretion process over the ocean and over the land, even if it would be necessary to distinguish the two processes to take into account the known variation in concentration of the CCNs over land and over oceans: over the land the concentration is higher so that there are more droplets with a smaller size, while over oceans larger cloud droplets tend to result in more collisions and coalescence giving rise to less thick clouds repect to the continental ones for the same probability of precipitation.

Accretion of cloud droplets by falling rain is parameterized following Beheng (1994) and it takes place only in the cloudy portion of the grid.

The accreted cloud water P_{acc} is given by:

$$P_{acc} = c_{acc} q_c P_{sum} \tag{1.11}$$

where c_{acc} is the accretion rate coefficient and P_{sum} is the accumulated precipitation, that is assumed to be uniformly distributed across the grid cell. This assumption often causes an overestimation of the accretion rate, as the process does not consider that portion of the grid where precipitation was formed before starting accreting.
Evaporation of raindrops is treated along the Sundqvist et al. (1989), for which the amount of evaporated precipitation P_{evap} is given by:

$$P_{evap} = c_{evap}(1 - RH)\sqrt{P_{sum}} \tag{1.12}$$

The higher is the subsaturation $(1-RH)$, the more efficient is the evaporation. As for the accretion, evaporation occurs only in the portion of the grid where there is no cloud.
Although SUBEX provides an accurate representation of the fields that are important for the energy and water budgets, the treatment of the ice microphysics is needed when considering that the model has been rapidly developing in the last years, and is going towards the use of higher resolutions with the inclusion, in the close future, of a non-hydrostatic compressible core.
In the current study a new one-moment large-scale cloud scheme is implemented into RegCM4, introducing an improvement of the cloud microphysics due to the separate treatment of the water and the ice phases, allowing the existence of mixed-phase clouds. A robust implicit numerics is needed to guarantee the use of larger timesteps, thus reducing the computational cost required for the use of higher spatial resolutions. A prognostic treatment of precipitating categories needs to be implemented to remove the assumption for which there is an instantaneous response of surface precipitation to the microphysical processes occurring in clouds, and to allow the precipitating species, such as rain snow and cloud ice, to be advected by the three-dimensional wind.

Chapter 2

Microphysics of clouds

2.1 Warm clouds physics

2.1.1 Nucleation and change of phase

Warm clouds are defined as clouds that are purely made of liquid water. The probability density function (PDF) of the droplet size distribution describes the wide range of droplets radii residing in a warm cloud. However the PDF is not a smooth function from the smallest to the largest radius, but it shows distinct peaks corresponding to distinct droplets radii that identify what are conventionally called the "bulk quantities".

Figure 2.1 illustrates the typical sizes and concentrations of the bulk quantities in warm clouds: the aerosols, the cloud droplets and the rain droplets. The smallest particles shown are the aerosols, indicated as Condensation Cloud Nuclei (CCN) in the figure, having a mean radius of 0.1μm. Typical observed CCN concentrations range roughly between 10-10^2cm^{-3} over the oceans and 10^2-10^3 cm^{-3} over the land (Wang, 2013). Aerosols are much smaller than cloud droplets that, with a mean radius of 10 μm, have a lower concentration of about 10^2 cm^{-3} in marine clouds. The figure shows also that the mean concentration of raindrops, with radii of about 1 mm, is much lower than the concentration of cloud droplets, suggesting that not all the cloud droplets become raindrops: the conversion from droplets into raindrops is indeed not obvious, and needs a proper description.

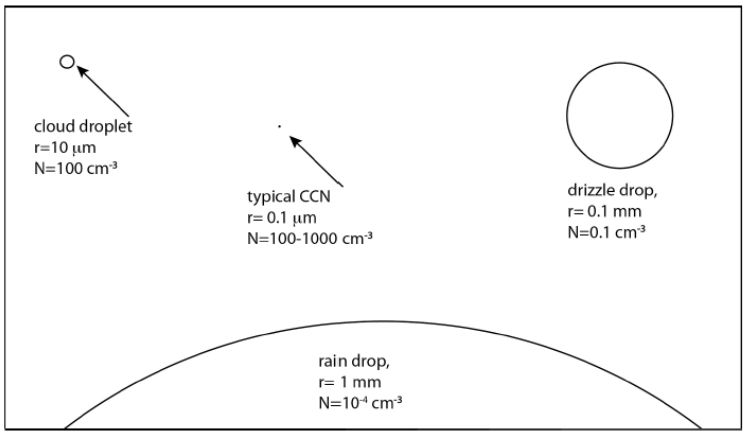

Figure 2.1: A wide spectra of droplet sizes can be treated in bulk categories having a typical radius and a typical concentration. Source: Rogers and Yau (1989).

Cloud droplets, in order to form, require a phase change to occur. The beginning of the physical change of phase lies in the process called *nucleation* and in the atmosphere it occurs in the formation of the cloud droplets and the ice crystals. Phase transitions in most cases occur at constant temperature T and constant pressure p and it is proven that the equilibrium state of a system kept at constant T and p is the state of minimum Gibbs free energy

$$G = H - TS \tag{2.1}$$

where $H = U + pV$ is the enthalpy of the system, and S is the entropy.
The variation of G indicates which is the "direction" of the phase change and whether the transformation is spontaneous or not.
Figure 2.2 shows the variation of G as a function of the volume V for three different partial pressures e_1, e_2 and e_3 that represent respectively a subsaturated ($e < e_s$), saturated ($e = e_s$) and supersaturated ($e > e_s$) system, where e_s is the saturation pressure:
For each partial pressure, the Gibbs free energy exhibits two minima, corresponding to the two thermodynamic equilibria of the substance in the liquid and in the gas phase. The state with higher G represents a metastable state: a state in which the substance tends to change the phase, under given circumstances, to reach the stable equilibrium.

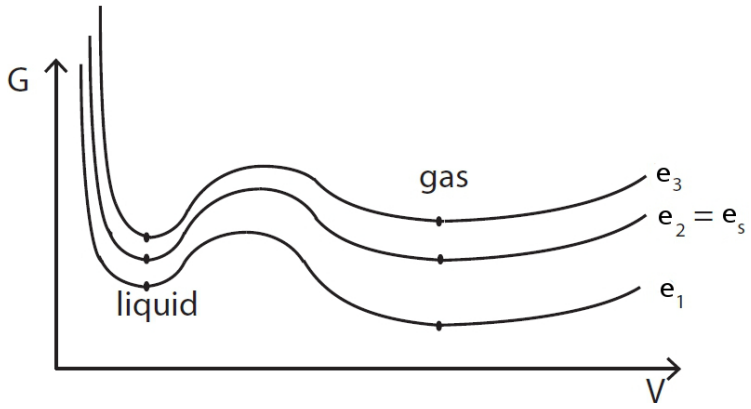

Figure 2.2: Variation of the free Gibbs energy G as a function of the volume V for three different systems: a subsubsaturated (e_1), a saturated (e_2) and a supersaturated (e_3). Source: Kashchiev (2000)

Considering as an example the phase change between gas and liquid, for supersaturated conditions, i.e. for $e > e_s$, the Gibbs free energy of the gas is greater than the Gibbs free energy of the liquid: the gas is supersaturated and hence tends to condensate into the liquid state. The opposite happens for undersaturated conditions $e < e_s$, in which the Gibbs free energy of the gas is lower than the Gibbs free energy of the liquid.
Metastable states and stable states are separated by an energy barrier. This means that the change of phase is inhibited as it does not occur spontaneously. All the phase transitions such as condensation, evaporation, melting and freezing exhibit the presence of an energy barrier.
Nucleation provides the most likely pathway of a phase transition, as it does not involve all the molecules of the system and the energy barrier is thus reduced: in the nucleation process the new phase starts locally in a small cluster of n molecules within an old phase environment.

2.1.2 Homogeneous Nucleation and the Kelvin's Theory

Let's consider the change of phase from an initial state of N_{tot} molecules of water vapour to a state where a spherical cluster of N_l molecules of liquid has formed. Being μ_v and μ_l the free Gibbs energies per molecule of the water vapour and of the liquid water respectively, the two Gibbs free energies G_1

and G_2 of the initial and of the final states can be expressed as follows:

$$G_1 = N_{tot}\mu_v \tag{2.2}$$
$$G_2 = (N_{tot} - N_l)\mu_v + N_l\mu_l + 4\pi r^2\sigma \tag{2.3}$$

where r is the cluster radius and σ is the free energy associated with the formation of a unit area of interface between the liquid and the vapour phase. The variation of the Gibbs free energy is therefore given by:

$$\begin{aligned}\Delta G &= G_2 - G_1 \\ &= 4\pi r^2\sigma + N_l\Delta\mu \end{aligned} \tag{2.4}$$

It can be shown that for the condensation of the water vapour phase into liquid:

$$\Delta\mu = -kT\ln\left(\frac{e}{e_s(T)}\right) \tag{2.5}$$

leading to:

$$\begin{aligned}\Delta G &= 4\pi r^2\sigma - N_l kT\ln\left(\frac{e}{e_s}\right) \\ &= 4\pi r^2\sigma - \frac{4\pi r^3}{3\alpha_l}R_v T\ln\left(\frac{e}{e_s}\right)\end{aligned} \tag{2.6}$$

where R_v is the gas constant of water vapour, and α_l is the specific volume of liquid water. Figure 2.3 shows two curves of ΔG as a function of the droplet radius r, for a subsaturated and supersaturated environment.

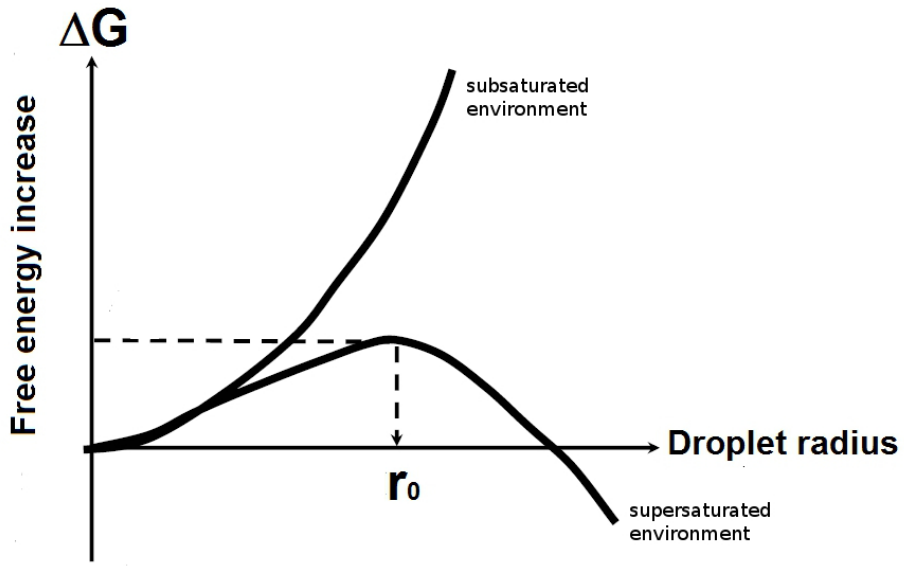

Figure 2.3: Schematic of the Gibbs free energy of a substance as a function of the volume that the substance occupies for three different pressure levels at a given T. Source: Kashchiev (2000)

In subsaturated conditions, for which $e < e_s$, the Gibbs free energy increases with r. This means that every increase of the droplet will lead to an increase of the free energy of the system. As stated, a system at constant temperature and pressure tends to go towards states with a minimum value for G: in a subsaturated environment the growth of the droplet is thus unfavourable and the droplets will tend to evaporate.
In supersaturated conditions, for which $e > e_s$, the Gibbs free energy instead exhibits a maximum for $r = r_0$. This radius represents a critical threshold: embryos with radii smaller than this value will evaporate, those with radii greater that this value will tend to grow by diffusion and they are said to be *activated*.
The critical value for the radius can be obtained by differentiating (2.6) with respect to r and setting the derivative equal to zero:

$$\begin{aligned} \frac{\partial \Delta G}{\partial r} &= 8\pi r_0 \sigma - \frac{4\pi r_0^2 R_v T}{\alpha_l} \\ &= 0 \end{aligned} \tag{2.7}$$

giving the Kelvin's formula:

$$r_0 = \frac{2\sigma}{nkTln(\frac{e}{e_s})} \tag{2.8}$$

stating that the greater is e with respect to e_s, the higher the supersaturation, the smaller is the critical radius beyond which droplets become activated.
The Kelvin's equation can be rearranged as:

$$e_s(r) = e_s(\infty) \exp\Big(\frac{2\sigma}{\rho_w R_v T r}\Big), \tag{2.9}$$

where $e_s(r)$ is the vapour pressure at which a droplet of radius r is in equilibrium, and $e_s(\infty)$, the vapour pressure of a flat water surface is in equilibrium. Equation (2.9) states that the saturation vapour pressure is larger over a drop with finite radius than over a flat surface (thought as a drop with infinite radius). The curvature of the droplet thus has the effect of increasing the equilibrium vapour pressure. This is easy to understand due to the fact that molecules at a curved surface have less neighbouring molecules than those at a flat surface. They are therefore less tied and less energy is required to break the bindings and to release the molecules into the gas phase as compared to a plane surface.
The processes for which a droplet forms and grows spontaneously is called **homogeneous nucleation**. A droplet with a radius of $0,01$ μm can be activated and grow only in an environment with at least the 300% of supersaturation. In the atmosphere the maximum values of supersaturation with respect to water observed are around the 1%: this means that the homogenous nucleation can not explain the formation of clouds.

2.1.3 Heterogeneous Nucleation and the Köler curve

The key process governing the formation of cloud droplets is the **heterogeneous nucleation**, that involves particles distributed in the atmosphere, some of which are soluble or wettable and are called Cloud Condensation Nuclei (CCN).
While the equilibrium vapour pressure increases with the curvature of a water surface, it can decrease if the water contains a dissolved soluble substance.
This effect is important because it reduces the supersaturation required in order to form cloud droplets and is described by the Raoult's law.
Let's consider a solution composed by n_0 water molecules and n solute molecules.

According to the law, the ratio between the equilibrium vapour pressure e^* over a planar surface ($r \to \infty$) of the solution and the equilibrium vapour pressure e over a planar surface of the solvent, in this case water, is given by:

$$\frac{e^*(\infty)}{e_s(\infty)} = \frac{n_0}{n + n_0}. \tag{2.10}$$

This equation states that if the vapour pressure of the solute is less than that of the solvent, and if the number of molecules is unchanged, the vapour pressure over the solution is reduced in proportion to the amount of solute present. In other words, as the number n of solute molecules increases, e^* decreases. This can be visualised by recalling that the saturation water vapour pressure is only related to the exchange of liquid molecules between the water droplet and the vapour phase. As the solute increases, the number of water molecules at the surface decreases, reducing the number of those that are able to leave the surface by evaporation.
Considering a droplet containing a mass M_s of solute with molecular weight m_s, the number of ions dissolved into the solute is given by:

$$n = \frac{iN_0M_s}{m_s} \tag{2.11}$$

where N_0 is the Avogadro's number and i is the degree of ionic dissociation. The number of water molecules with molecular weight m_w in a mass M_w is likewise given by:

$$n_0 = \frac{N_0M_w}{m_w}. \tag{2.12}$$

Applying the Raoult's law to a solution droplet of radius r, with density ρ_s, its mass can be written as:

$$M = M_s + M_w = \frac{4}{3}\pi r^3\rho_s. \tag{2.13}$$

Assuming that M_s is much smaller than M_w, for dilute solutions gives rise to:

$$\frac{e^*(\infty)}{e_s(\infty)} \approx 1 - \frac{n}{n_0} = 1 - \frac{3iM_sm_w}{4\pi m_s\rho_w r^3} = 1 - \frac{b}{r^3} \tag{2.14}$$

that allows to say that the smaller the droplet the larger is the effect played by the presence of the solute in decreasing the equilibrium vapour pressure requires. On the other hand the Kelvin effect stated that the smaller the droplet

the bigger is the curvature and thus the greater the equilibrium vapour pressure.

The balance between the two effects is well described by the Köhler curve:

$$\frac{e^*(r)}{e(\infty)} = 1 + \frac{a}{r} - \frac{b}{r^3} \tag{2.15}$$

The Köhler curve, shown for a sample solution in Figure 2.4, is a combination of the Kelvin's equation and the Raoult's law and displays the equilibrium vapour pressure as a function of the droplet radius. Every aerosol particle that serves as a CCN has its own Köhler curve.

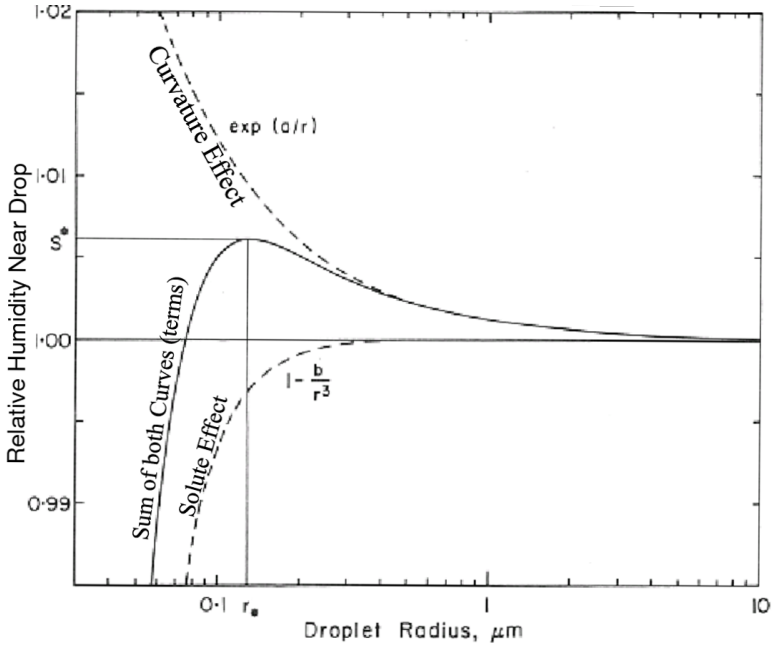

Figure 2.4: Equilibrium saturation ratio of a solution droplet formed on an ammonium sulphate condensation nucleus of mass 10^{-6}g.

Due to the solute and curvature effects, it is possible to have condensation for relative humidities $RH < 100\%$. Aerosols are indeed observed to act as Cloud Condensation Nuclei (CCN) forming haze as $RH \approx 78\%$.

Let's consider in Figure 2.4 a droplet in equilibrium with $r < r_0$. If a small perturbation slightly increases the size of the droplet, and thus for an atmosphere that is subsaturated with respect to the droplet, this will cause molecules to evaporate and force the droplet back to the curve.

Applying, on the other hand, a small perturbation that removes some molecules from the droplet will reduce its radius, and the atmosphere will be supersaturated with respect to the droplet giving rise to condensation of the and water

vapour molecules on the droplet until it will be back on the curve.
For a droplet with radius $r > r_0$, a small increase in RH will cause the drop to be supersaturated with respect to the equilibrium curve and to grow. However, doing so, it will not reach the equilibrium with the environment and the drop will simply continue to grow without bounds. Once reached its critical size, the droplet is said to be activated and starts to grow by diffusion of water vapour onto its surface.

2.1.4 Growth by diffusion

As the droplet is activated it continues growing by diffusion of water vapour toward the droplet. The flux of water vapour is described by the Fick's law:

$$F = 4\pi n^2 D \frac{d\rho_v}{dn} \tag{2.16}$$

where D is the diffusion coefficient for water vapour and ρ_v is the density of water vapour in the area surrounding the droplet.
Assuming that the water vapour is the only contributor to the increase of the mass droplet M:

$$\begin{aligned} \frac{dM}{dt} &= 4\pi D n^2 \frac{d\rho_v}{dn} \\ \frac{dM}{dt} \int_r^\infty \frac{dn}{n^2} &= 4\pi D \int_{\rho_v(r)}^{\rho_v(\infty)} d\rho_v \\ \frac{dM}{dt} &= 4\pi D r(\rho_v(\infty) - \rho_v(r)) \end{aligned} \tag{2.17}$$

and, using $M = \frac{4}{3}\pi r^3 \rho_w$, with ρ_w the density of water, and using (2.15) it is easy to obtain:

$$\frac{dr}{dt} = \frac{D e_s^\infty}{\rho_w r R_v T}(S-1) \tag{2.18}$$

where S is the supersaturation defined as $S = \frac{e}{e_s}$.
Equation (2.18) states that the growth rate decreases as the drop radius increases.
Diffusion process is, however, very slow because of the latent heating associated with the condensation, that increases e_s and slows down the growth.
Diffusion plays its main role in activating the cloud droplets, but another process is responsible for their growth and for the formation of rain droplets: the collision-coalescence.

2.1.5 Growth by Collision and Coalescence

The process for which droplets collide and stick together forming a larger drop, is called collision-coalescence. This process represents the dominant growth mechanism for drops of radius larger than about 10 μm (Davis and Sartor, 1967) and occurs when two cloud droplets of different sizes come into contact because of their different terminal velocities.
Let's consider a large droplet of radius R falling through a cloud of smaller droplets of radius r, and let's assume for simplicity that any droplet in the path of the large droplet is collected by the large droplet. The mass accumulation rate is given by:

$$\frac{dM}{dt} = L\pi(R+r)^2(V-v), \tag{2.19}$$

where L is the liquid water content of the small droplet.
Assuming that the large droplet has a radius much bigger than the radius of the droplets that it collects, therefore $R >> r$ and $V >> v$, and using $M = \frac{4}{3}\pi r^3 \rho_w$, the rate of change of the radius R is derived as follows:

$$\frac{dR}{dt} = \frac{LV}{4\rho_w}. \tag{2.20}$$

Droplets of radius $R < 30\mu m$ have a terminal velocity $V = X_1 R^2$, with $X_1 = 1.2 \cdot 10^{-8}$, so that the equation becomes:

$$\frac{dR}{dt} = \frac{LX_1R^2}{4\rho_w}. \tag{2.21}$$

The growth rate due to collision is thus proportional to the square of the droplet radius, while the diffusional rate, as seen previously, is proportional to the inverse of the radius. Figure 2.5 shows that when a droplet starts to grow the dominant growing process is the diffusion (blue line), that is replaced by collision (red line) once the droplet has reached a size threshold (e.g. 20μm in the figure).

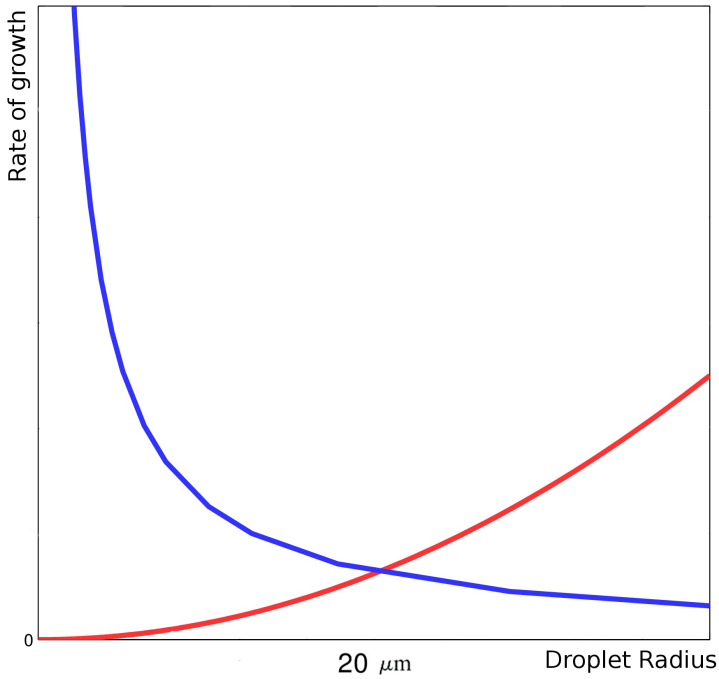

Figure 2.5: Conceptual model of the rate of growth of cloud droplet radius by condensation and collision-coalescence in warm clouds. At the beginning, when the droplet has just formed the growth is governed by diffusion (a). Once reached a size threshold, diffusion is replaced by collision (b).

2.2 Cold clouds physics

When clouds extend to altitudes with temperatures below 0° ice crystals may form either by freezing of a cloud droplets or by deposition of water vapour to the solid phase. Both the processes are nucleation processes because a stable cluster of ice phase has to form from an existing parent phase, vapour or liquid. Unlike for warm clouds, in cold clouds both the homogeneous and the heterogeneous nucleations can occur and are observed in the atmosphere. Heterogeneous nucleation requires the presence of an ice nucleus (IN) and is the dominant ice-formation process in mixed-phase clouds, i.e. clouds in which both ice crystals and supercooled liquid water coexist, and form at temperatures between 0 and -40°. Air is said to be saturated with respect to ice when the deposition rate (vapour into ice) equals sublimation rate (ice into vapour). As the intermolecular bonding energy in ice is greater than that in liquid water, at a given temperature the evaporation rate is larger than the sublimation rate. For this reason the saturation vapour pressure with respect to ice is smaller than the saturation vapour pressure with respect to water $e_{si}(T) < e_{sw}(T)$ (see Figure 2.6).

2.2.1 Homogeneous Nucleation of Ice from Liquid

Homogeneous nucleation of ice is analogous to homogeneous cloud droplet nucleation. Nucleation occurs when an initial crystal or ice germ forms by statistical fluctuations of the liquid molecular arrangement and forms a stable lattice structure. If the germ is over a critical size, other water molecules bind to it and the water body freezes rapidly. The formation of the ice germ has more probability to occur in a pond rather than in a cloud droplet, and the probability increases with lower temperatures. For this reason it is possible to find liquid cloud droplets existing at temperature below 0°C and these droplets are referred to as "supercooled droplets". Both theoretical results and observation prove that cloud liquid droplets freeze spontaneously by homogeneous nucleation at temperature lower than about -38°.

2.2.2 Homogeneous Nucleation of Ice from Vapour

In order to form an ice crystal directly from the vapour phase, very high supersaturations would be required (S>1000%). In nature these supersaturations are not observed as air would be supersaturated with respect to water forming droplets that would freeze.
Analogously of what found for the warm clouds (see eq. 2.6), the energy barrier to be overcome for the phase change vapour-ice is given by the Kelvin's law:

$$\Delta G_{i,v} = 4\pi r^2 \sigma_{i,v} - \frac{4\pi r^3 R_v T}{3\alpha_i} \ln S_i \tag{2.22}$$

where $G_{i,v}$ is the free Gibbs energy for the phase change from vapour to ice and $\sigma_{i,v}$ is the surface tension between ice and vapour, and α_i is the specific volume of ice. Being that $\alpha_i > \alpha_l$, as ice occupies a greater volume than water, and that $\sigma_{i,v} > \sigma_{l,v}$, the homogeneous nucleation of ice from vapour is even more unlikely than homogeneous cloud droplet nucleation.

Figure 2.6 shows the supersaturations vapour pressures with respect to water and ice as functions of temperature.

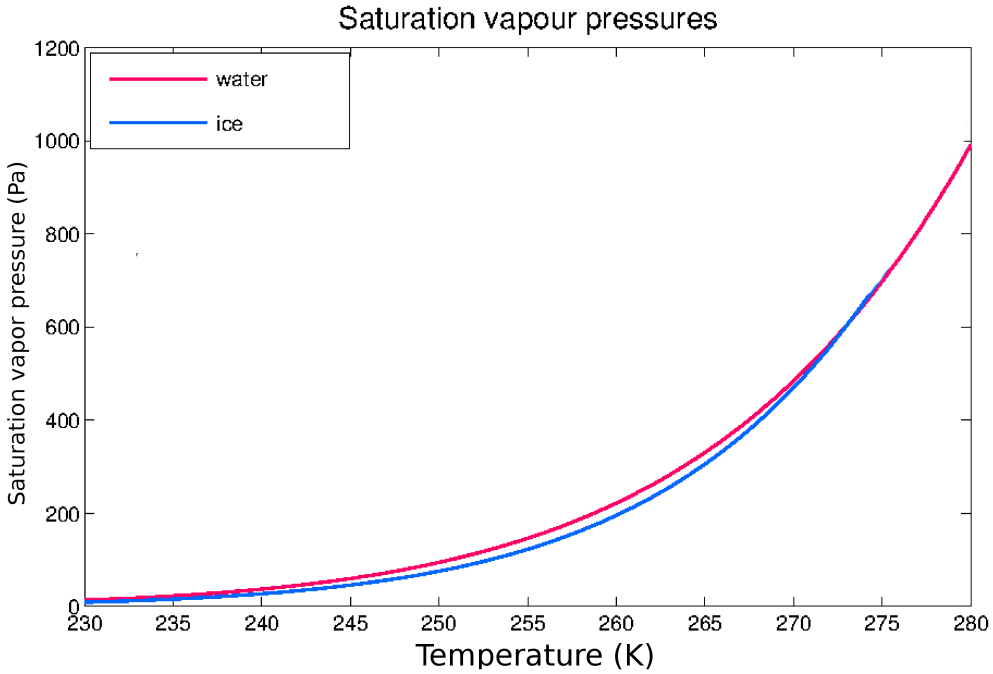

Figure 2.6: Saturation vapour pressure with respect to water and to ice. Ice saturation vapour pressure is smaller than water vapour saturation pressure.

A consequence of the fact that $e_{si}(T) < e_{sw}(T)$ is that air can be supersaturated with respect to ice without forming ice cloud. There is, however, an upper limit for the amount of ice supersaturation set by the vapour pressure at which liquid droplets start to form and then freeze spontaneously if the temperature is below -38°. As seen in the warm cloud physics section, haze start to form at RH=78% due to the Kelvin effect. For this reason the upper limit for ice supersaturation is lower than the saturation vapour pressure e_{sw}. The limit has been studied by Koop et al. (2000) and found to be equal to 45% ice supersaturation at T=-38° C increasing to 67% at T=-83°C.

2.2.3 Heterogeneous Nucleation of Ice

Heterogeneous nucleation initiates freezing with the help of the ice nuclei (IN), that favours freezing over homogeneous freezing because it reduces the energy barrier to the formation of a critical ice germ. Aerosols can act as IN if their molecular structure is similar to the lattice structure of ice crystals. For this reason IN are much less common than CCN. There is, however, a dependence of the number of IN on the temperature and on the supersaturation: as ice supersaturation increases and temperature lowers the number of aerosols with the ability of acting as ice nuclei increases.

2.2.4 Ice crystals growth

In mixed phase clouds, ice crystals mainly grow by the Wegener-Bergeron-Findeisen process. As previously discussed a cloud that is saturated with respect to water is supersaturated with respect to ice. For this reason in mixed phase clouds, where supercooled water droplets and ice crystal coexist, if a supercooled droplet freezes the ice crystal will grow by diffusion of water vapour toward the ice crystal. This causes a decrease of the water vapour pressure e to values below the water vapour saturation pressure with respect to water e_{sw}. The liquid droplets find themselves in subsaturated conditions (with respect to water) and therefore evaporate. Figure 2.7 shows on the left a sketch of the process for which ice grow at the expense of liquid. On the right a laboratory photo illustrating the result of the WBF-effect.

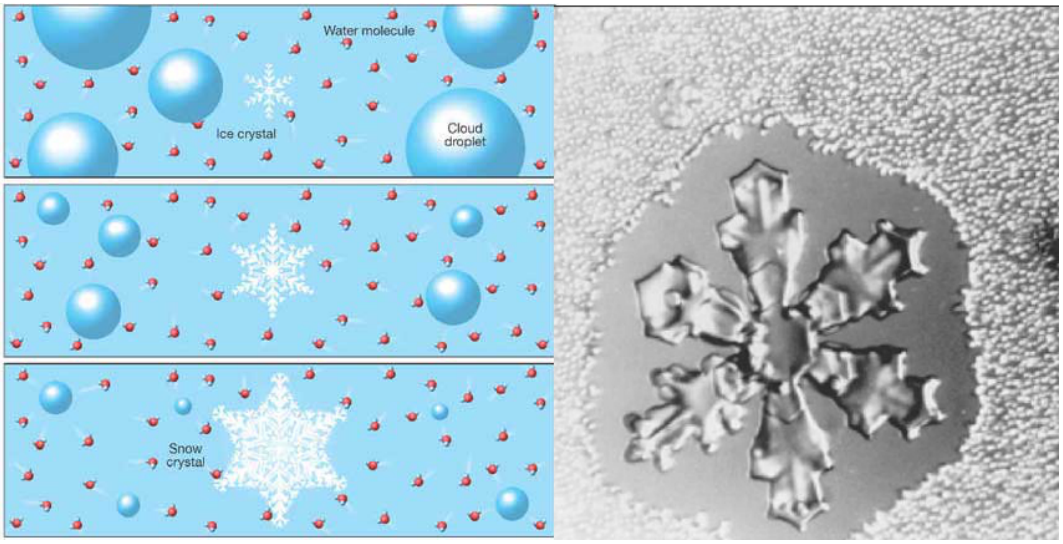

Figure 2.7: (left) sketch of the growth of ice at the expenses of liquid; (right) photo of the Bergeron-Findeisen effect by R.Potter.

Chapter 3

The New Microphysics Cloud Scheme

3.1 The Numerics

The new large scale precipitation scheme is built upon the European Centre for Medium Weather Forecast's Integrated Forecast System (IFS) (Tiedtke, 1993; Tompkins, 2007) and is going to replace the previous scheme that, as pointed out in the Chapter 2, involves two prognostic variables, the water vapour and the cloud liquid water, while ice and snow processes are a function of temperature only as they are formed diagnostically when temperature is below $T = 0°C$.

In the new scheme liquid and ice water content are independent, allowing the existence of supercooled liquid water and mixed-phase clouds. The other important achievement of the new scheme is the new prognostic rain and snow precipitate with a fixed, finite, terminal fall speed and can therefore be advected by the three dimensional wind.

The new one-moment scheme solves implicitly 5 prognostic equations for water vapour, cloud liquid water, rain, ice and snow and it is also easily suitable for a larger number of variables.

Each variable is expressed in terms of the grid-mean mixing ratio q_x(kg kg^{-1}), defined as:

$$q_x = \frac{1}{V} \int_V \frac{\rho_x}{\rho} dV \tag{3.1}$$

where ρ_x is the density of the variable q_x, ρ is the density of the moist air and V is the total volume of the grid box.

The mixing ratios of each water category (q_v for the water vapour, q_c for the

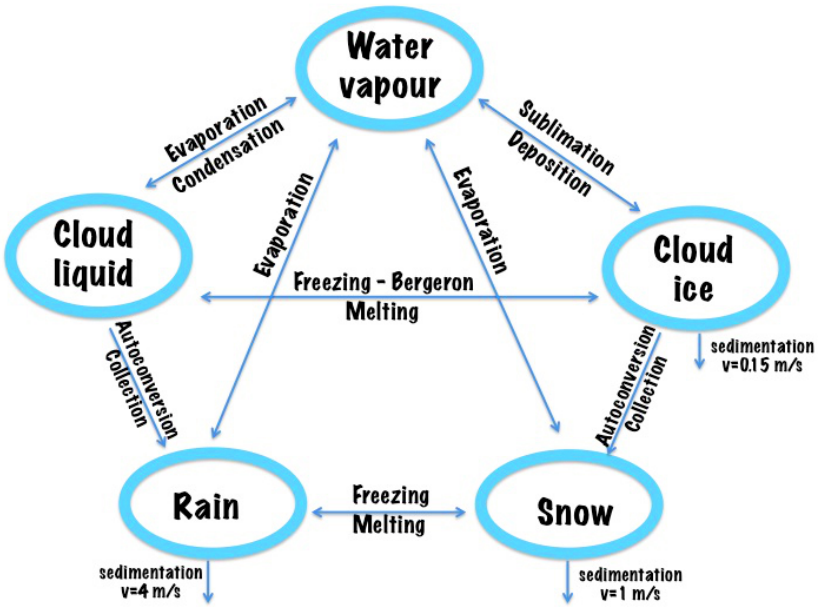

Figure 3.1: Schematics of the new scheme, showing the 5 prognostic variables and how they are related to each other through microphysical processes.

cloud droplet, q_r for the rain , q_i for the ice and q_s for the snow) are governed by a conservation equation of the form:

$$\frac{\partial q_x}{\partial t} = S_i + \frac{1}{\rho}\frac{\partial}{\partial z}(\rho V_x q_x) \tag{3.2}$$

Where S_i is a term that includes the source and sink terms for the water categories, thus all the conversion of water substance through microphysical pathways from one category to another (see Figure 3.1), and the second term on the RHS represents the source of the category q_x from the layer above due to the gravitational sedimentation of the species falling with velocity V_x.
The sources and sinks contributors are divided in two groups, A and B, according to the duration of the process they describe. Processes that are considered to be fast relative to the timestep of the model (like for example the autoconversion), are treated implicitly and are all included in the matrix B, that is positive-definite off the diagonal, with $B_{xx} = 0$ by definition. A positive term B_{xy} represents a process that is a source of q_x and a sink of q_y.
On the other hand, processes that are considered to be slow with respect to the timestep of the model (like for example melting and freezing) are treated explicitly and are included in the matrix A whose elements A_x represent the net contribution to the variable q_x by the explicit processes.

Unlike implicit terms, explicit terms are able to reduce a cloud category to zero or to negative values. In order to avoid this, and to therefore ensure that all variables remain positive definite at the end of the time step the initial vector $\vec{A}$ containing the explicit source and sink terms is generalised using an antisymmetric matrix A, whose elements $A_{xy} > 0$, as for the analogous implicit terms, represent a source of the variable q_x and a sink of q_y:

$$\begin{pmatrix} A_{11} & A_{21} & A_{31} \\ -A_{12} & A_{22} & A_{32} \\ -A_{13} & -A_{23} & A_{33} \end{pmatrix}$$

All the terms in the diagonal, A_{xx}, represent the external sources of the variable, such as the cloud water detrainment given as an input from the convection scheme. For each timestep, before calling the solvers, the sum of all sinks of each variable is scaled to avoid negative values. This method avoids negative values guaranteeing conservation.
The equations are solved using the upstream approach, that uses the forward difference quotient in time and the backward difference quotient in space.
For the timestep n the equations can therefore be rewritten as:

$$\frac{q_x^{n+1} - q_x^n}{\Delta t} = A_x + \sum_{x=1}^{m} B_{xy} q_y^{n+1} - \sum_{x=1}^{m} B_{yx} q_x^{n+1} + \frac{\rho_{k-1} V_x q_{x,k-1}^{n+1} - \rho V_x q_x^{n+1}}{\rho \Delta z}. \quad (3.3)$$

The equations are integrated from the top to the bottom layer of the model, so that the index $k-1$ represents the level above the present level at which the variable was calculated. The solution method assumes that vertical sedimentation acts only in the downward direction.
This considerably reduces the dimensions of the matrix equation that, for a 3-variable system is:

$$\begin{pmatrix} 1 + \Delta t(\frac{V_1}{\Delta z} + B_{21} + B_{31}) & -\Delta t B_{12} & -\Delta t B_{13} \\ -\Delta t B_{21} & 1 + \Delta t(\frac{V_2}{\Delta z} + B_{12} + B_{32}) & -\Delta t B_{23} \\ -\Delta t B_{31} & -\Delta t B_{32} & 1 + \Delta t(\frac{V_3}{\Delta z} + B_{13} + B_{23}) \end{pmatrix} \cdot \begin{pmatrix} q_1^{n+1} \\ q_2^{n+1} \\ q_3^{n+1} \end{pmatrix} =$$

$$= \begin{pmatrix} q_1^n + \Delta t\Big(A_1 + \frac{\rho_{k-1} V_1 q_{1,k-1}^{n+1}}{\rho \Delta z}\Big) & q_1^n + \Delta t\Big(A_2 + \frac{\rho_{k-1} V_2 q_{2,k-1}^{n+1}}{\rho \Delta z}\Big) & q_3^n + \Delta t\Big(A_3 + \frac{\rho_{k-1} V_3 q_{3,k-1}^{n+1}}{\rho \Delta z}\Big) \end{pmatrix}$$

For each microphysical pathway the change of phase is associated with a release or an absorption of latent heat, that has a significant impact on the temperature budget.

The impact is calculated using the conservation of liquid water temperature T_L defined as:

$$T_L = T - \frac{L_v}{C_p}(q_l + q_r) - \frac{L_s}{C_p}(q_i + q_s). \tag{3.4}$$

Being that $\frac{dT_L}{dt} = 0$, the rate of change of the temperature is given by the following equation:

$$\frac{\partial T}{\partial t} = \sum_{x=1}^{m} \frac{L(x)}{C_p}\Big(\frac{dq_x}{dt} - D_{q_x} - \frac{1}{\rho}\frac{\partial}{\partial z}(\rho V_x q_x)\Big) \tag{3.5}$$

where $L(x)$ is the latent heat (of fusion or evaporation depending on the processes considered), D_{q_x} is the convective detrainment and the third term in the brackets is the sedimentation term.

At the end of each timestep a routine checks the conservation of the total water and of the moist static energy $h = C_P T + gz + Lq_x$.

3.1.1 The code

In order to solve the system of equations (3.3), but for five variables, the numerics of the scheme are structured in the following way:

- Get in input from the model the initial profiles for q_v, q_c, q_r, q_i and q_s;
- Calculate the initial enthalpy and total water;
- Define supersaturation with respect to water and with respect to ice;
- Adjust supersaturation and evaporate where there is no cloud;
- Get the convective detrainment from convection;
- Calculate the erosion by turbulent mixing;
- Calculate the variation of the saturation vapour pressure dq_{sat}/dt;
- Calculate the evaporation of clouds;
- Calculate the condensation;
- Calculate the growth of ice by vapour deposition;
- Calculate the sedimentation of the falling species;
- Calculate the precipitation overlap;
- Calculate the autoconversion of rain and snow;
- Calculate the melting of snow and ice;
- Calculate the freezing of rain and snow;
- Calculate the evaporation of the falling categories (ice, rain and snow);
- Numerical solvers - truncates explicit sinks to avoid negative values;
- Numerical solvers - LU decomposition for the 5 species;
- Update the tendencies of the 5 categories and of the temperature;
- Calculate precipitation fluxes;
- Calculate the final enthalpy and total water to ensure conservation.

3.2 The Microphysics of the new scheme

As mentioned at the beginning of this chapter, the new microphysics scheme is built upon the European Centre for Medium Weather Forecast's Integrated Forecast System (IFS). However some differences reside between the two codes. The main difference is that RegCM4 cloud fraction is not prognostic. The diagnostic approach has the advantage of simplifying the implementation and saving the computational cost and memory. The simplification does not imply that the local cloud properties are independent of the local dynamics but cloud generation is not directly linked to physical processes and is diagnosed from the relative humidity and from the cloud condensate as presented in section 3.2.3. Another difference between the codes resides in the treatment of the autoconversion process, i.e. the mechanism for which rain droplets form on the account of cloud droplets. As this process plays a crucial role in the development of the precipitation the new code offers the choice between four different parameterizations of the autoconversion, as described in section 3.2.7. The new code, as the IFS, contains a simplified treatment of the sedimentation, with constant values for the hydrometeors fall speeds that avoid the numerical "shocks" occurring when using long timesteps and a physical mass related fall speeds. The new code does not adjust the fallspeeds of ice and snow to account for variations in temperature and pressure as done in the IFS code, following Heymsfield and Iaquinta (2000).
The following sections describe the equations used to parameterise the cloud and precipitation processes.

3.2.1 Saturation vapor pressures

According to Teten's formula described by Murray (1967) the saturation vapour pressures with respect to water e_{sw} and with respect to ice e_{si} (in hPa) are defined as the following:

$$e_{sw} = 610.78 \exp 17.269\Big(\frac{T - 273.16}{T - 35.86}\Big) \tag{3.6}$$

$$e_{si} = 610.78 \exp 21.874\Big(\frac{T - 273.16}{T - 7.66}\Big) \tag{3.7}$$

The saturation mixing ratio, or saturation specific humidity, is a function of

the saturation water vapour pressure and is defined as:

$$q_{sat} = \frac{\epsilon e_s}{p - \Big(1 - \epsilon\Big) e_s} \tag{3.8}$$

where ϵ is the ratio between the gas constant for dry air R_d and the gas constant for water vapor R_v.

3.2.2 Mixed phase

As previously highlighted both ice and water can coexist in clouds at temperature below 0°C, in amounts that are prognostically calculated solving equations (3.3). For the convective detrainment, however, the phase of the cloud is determined as a function of temperature, as in Tiedtke (1993).
For this process the fraction of liquid water in the total condensate is described as:

$$\alpha = \begin{cases} 0 & T \leq T_{ice} \\ \left(\frac{T - T_{ice}}{T_0 - T_{ice}}\right)^2 & T_{ice} < T < T_0 \\ 1 & T \geq T_0 \end{cases} \tag{3.9}$$

where T_0 = 273.16 K and T_{ice} =250.16 K is the temperature below which clouds are assumed to contain pure ice.

3.2.3 The Cloud Fraction

The cloud fraction parameterization has changed from the previous scheme. In the SUBEX scheme the cloud fraction is calculated diagnostically from the relative humidity following Sundqvist et al. (1989):

$$C = 1 - \sqrt{\frac{RH_{max} - RH}{RH_{max} - RH_{min}}} \tag{3.10}$$

where RH_{min} is the relative humidity threshold at which clouds begin to form, and RH_{max} is the relative humidity where C reaches unity. As mentioned before, large-scale RH is the most frequent predictor for determining the cloud amount in existing diagnostic parameterizations (e.g. Smagorinsky, 1960; Slingo, 1980; Sundqvist, 1978).
Xu and Randall (1996) developed a semiempirical cloudiness parameterization that uses the large-scale relative humidity RH but considers the large-scale

average condensate (cloud water and cloud ice) mixing ratios $\bar{q_l} = q_l + q_i$ as the primer predictor:

$$C = \begin{cases} RH^p[1 - \exp(-\frac{\alpha_0 \bar{q_l}}{[(1-RH)q_s}]^\gamma] & \text{if } RH < 1 \\ 1 & \text{if } RH \geq 1 \end{cases} \tag{3.11}$$

where the values of p, α_0 and γ are empirically determined as, respectively, 0.25, 0.49 and 100. Using a cloud ensemble model (CEM) they showed that even if RH and C have a high correlation coefficients in the upper troposphere, the range of the variation C for a given RH is extremely large. They addressed the large variation to the presence of different amounts of cloud water/ice for a given RH. They also showed that there is not a unique RH threshold for zero cloud fraction C at any level. Studying the correlation between $\bar{q_l}$ and C they proved that the grid-averaged mixing ratio of condensate is a much better predictor for stratiform cloudiness than the grid-averaged RH, that is also used in the parameterization but as secondary predictor.
The cloud fraction is used to calculate the specific cloud water and ice contents per cloud area:

$$q_l^{cld} = \frac{q_l}{C}, \quad q_i^{cld} = \frac{q_i}{C} \tag{3.12}$$

that represents the "in-cloud" humidity: the bigger the cloud, the lower the in-cloud humidity.

3.2.4 Condensation

In this section the formation of stratiform clouds associated with large-scale lifting of moist air or with radiative cooling, is treated as a function of the variation in time of the saturation mixing ration, folllowing Tiedtke (1993). In fact if the saturation mixing ratio decreases, condensation occurs while as it increases evaporation takes place (see Figure 3.2).

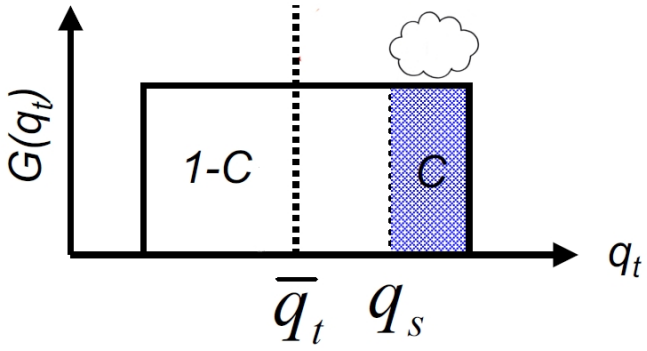

Figure 3.2: Graphical aid to the saturation mixing ratio's variation as a key factor in regulating the condensation or evaporation occurrence. q_t is the total water amount and $G(q_t)$ is the Probability Density Function for q_t. Source: Tompkins (2005). Modified.

The variation in time of the saturation mixing ratio can be written as:

$$\begin{aligned}\frac{dq_{sat}}{dt} &= \frac{\partial q_{sat}}{\partial T}\frac{DT}{Dt} \\ &= \frac{\partial q_{sat}}{\partial T}\left[\frac{\partial T}{\partial t} + \omega\frac{\partial T}{\partial p}\right] \\ &= \frac{\partial q_{sat}}{\partial T}\frac{\partial T}{\partial t} + \left[\frac{\partial q_{sat}}{\partial T}\omega\frac{\partial T}{\partial p}\right] \\ &= \frac{\partial q_{sat}}{\partial T}\frac{\partial T}{\partial t}\Big|_{diab} + \frac{\partial q_{sat}}{\partial p}\Big|_{ma}\omega \end{aligned} \tag{3.13}$$

This equation shows that the rate of change of the saturation mixing ratio is linked to diabatic cooling $(dT/dt)_{diab}$ and to the vertical motion with a grid mean vertical velocity ω, where $(dq_{sat}/dp)_{ma}$ is the variation of q_{sat} along a moist adiabat.

As previously mentioned, condensation occurs when:

$$\frac{dq_{sat}}{dt} < 0 \tag{3.14}$$

The condensation rate C_1 is proportional to the amount of cloud and is equal to:

$$C_1 = -C\frac{dq_{sat}}{dt}, \qquad \frac{dq_{sat}}{dt} < 0 \tag{3.15}$$

and all the increase of cloud is a source of cloud water unless the process occurs within cold clouds, in which case condensation is a source of ice as homogeneous freezing takes place.

3.2.5 Condensation from detrainment

As an input from the convection scheme the microphysics scheme receives the detrained mass flux D that is assumed to condensate into cloud water or into ice diagnostically as a function of temperature using the coefficient defined in equation 3.9. This process is applied for all types of convection, namely deep, shallow and mid-level and represents an important extension of the model's cumulus parameterization.
The source of water/ice cloud content is given by:

$$\frac{\partial q_x}{\partial t} = \alpha D + (1 - \alpha) D \tag{3.16}$$

where x represents either ice or liquid according to the value of α.

3.2.6 Evaporation of cloud water and ice

The scheme treats two processes that induce evaporation: the large scale descent and the diabatic heating, giving rise to E_1, and the turbulent mixing of cloud air with drier environmental air, producing E_2, so that the total evaporation E is given by:

$$E = E_1 + E_2 \tag{3.17}$$

As opposed to condensation, evaporation is proportional to the increase of the saturation mixing ratio and to the amount of cloud following:

$$E_1 = C \frac{dq_{sat}}{dt}, \qquad \frac{dq_{sat}}{dt} > 0 \tag{3.18}$$

It is reasonable to assume that the cloud water content within clouds is homogeneously distributed in the horizontal direction, therefore the evaporation is not changing the cloud cover until it reduces to zero.
As assumed by Tiedtke (1991), the evaporation by turbulent mixing is considered proportional to the subsaturation of the environment so that:

$$E_2 = kC(q_{sat} - q_v) \tag{3.19}$$

where $k = 3 \cdot 10^{-6} \mathrm{s}^{-1}$ is the diffusion coefficient per unit area.

3.2.7 Autoconversion of cloud water to rain

Droplets with radius smaller than about 20μm grow by diffusion of water molecules from the vapour onto their surface. Vapour diffusion alone is how-

ever too slow at larger droplet size. In fact for radii greater than 20μm gravity begins to take over, and the droplets fall slowly and irregularly, growing through collision and coalescence by collecting smaller droplets.
Autoconversion is the mechanism for which rain or snow droplets form on the account of cloud water or cloud ice. This process plays a crucial role in the development of the precipitation and is rather efficient given that a raindrop of 1 mm is the result of $\sim 10^5$ collisions (Rogers and Yau, 1989).
The first approach in autoconversion's parameterization was suggested by Kessler (1969). Kessler assumed that "up to some threshhold, clouds are stable, and that above that threshold, a certain fraction of the cloud changes to rain per unit time". His scheme therefore parameterizes the autoconversion as a function of the mean cloud water content in the grid box and autoconversion starts once a critical cloud water content is exceeded (e.g. 1 g m^{-3}).
All the autoconversion's parameterization approaches use a form like the following:

$$P = P_0 \cdot T \tag{3.20}$$

where P is the autoconversion rate, P_0 the autoconversion rate once the autoconversion has started, and $T \leq 1$ a function that describes the threshold behaviour (Liu and Daum, 2004).
Kessler (1969) was the first to propose a simple parameterization that assumes a critical value q_{crit} that represents a threshold for the occurrence of autoconversion: for cloud liquid water contents greater than q_{crit} the autoconversion rate is linearly related to q_l, while for values below q_{crit} no autoconversion occurs:

$$\frac{\partial q_l}{\partial t} = k \cdot (q_l - q_{crit}) \tag{3.21}$$

with $k = 10^{-3}$ s^{-1} and $q_{crit} = 0.5$ gm^{-3}.
This can be referred to as an "all-or-nothing" approach, and it does not accurately represent the threshold behaviour.
Sundqvist (1978) proposed an alternative approach without discontinuities that uses a smoother threshold function. :
The rate of change of cloud liquid water q_l results to be given by:

$$\frac{\partial q_l}{\partial t} = c_0 F_1 q_l \left\{ 1 - \exp\left[- \left(\frac{q_l^{cld}}{q_l^{crit}} \right)^2 \right] \right\} \tag{3.22}$$

and it depends on $c_0 = 1.67 \cdot 10^{-4}$ s^{-1}, a characteristic time scale for conversion

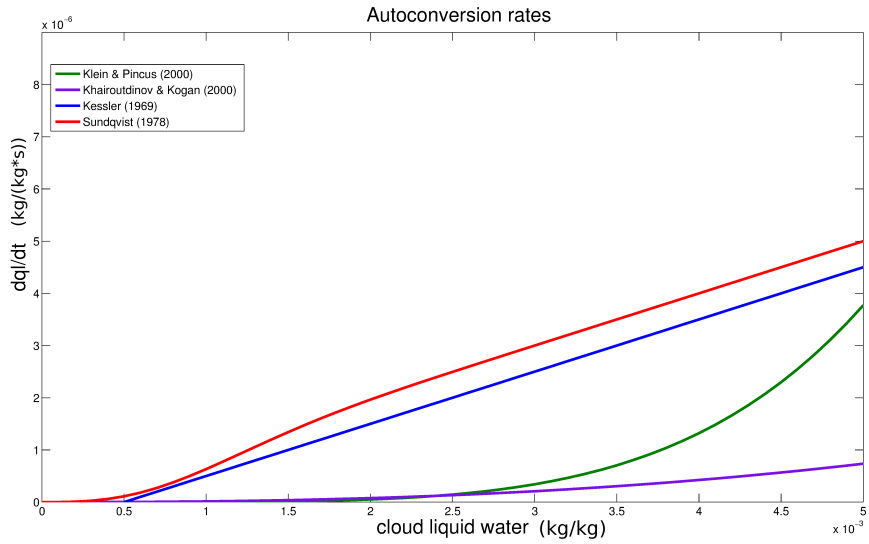

Figure 3.3: Options for the autoconversion parameterizations. For plotting the Sundqvist rate, the accretion term F_1 was set to 1 in order to be compared to the other rates.

of cloud liquid droplets into rain drops, on q_l^{crit}, a typical cloud water content at which the generation of precipitation begins to be efficient that assumes different values over land (0.5 g kg^{-1}) and over ocean (0.3 g kg^{-1}), and an accretion term F_1, defined as:

$$F_1 = 1 + b_1\sqrt{P_{loc}} \tag{3.23}$$

where P_{loc} is the local cloudy precipitation rate, b_1=100 kg m^{-2}s^{-1}
A different threshold function was proposed by Pincus and Klein (2000)

$$\frac{\partial q_l}{\partial t} = c_{kp} \cdot q_l^{3.3} \tag{3.24}$$

where $c_{kp} = 2.461 \cdot 10^5$ s^{-1} and another by Khairoutdinov and Kogan (2000)

$$\frac{\partial q_l}{\partial t} = c_{kk} \cdot q_l^{2.47} \tag{3.25}$$

where $c_{kk} = 0.355$ s^{-1}.
The new scheme allows the choice of the autoconversion treatment within the four parameterizations above described and shown in Figure 3.3.
A sensitivity of the model to this choice will be presented in the results chapter.

3.2.8 Autoconversion of cloud ice to snow

The parameterization used for autoconversion of ice has the same form as 3.22 but with different parameters more appropriate for ice: according to Lin et al. (1983) c_0 is a function of the temperature T:

$$c_0 = 10^{-3} \exp(0.025 \cdot (T - 273.15)) \tag{3.26}$$

and q_{crit}=4·10^{-5}kg kg^{-1}.

3.2.9 Precipitation fraction and evaporation of rain and snow

The use of a precipitation fraction is needed if considered that precipitation processes behave differently in clear and cloudy conditions. Microphysical processes are indeed very distinct from each other in these different regions.
In the cloudy part of the grid condensation, accretion, collection processes play the main role, whereas in the clear part the relevant process is the evaporation of precipitation.
The precipitation fraction in the grid-box is then described as

$$C_P = C_P^{cld} + C_P^{clr} \tag{3.27}$$

The total precipitation fraction at the k level $C_{P,k}$ is calculated using a maximum overlap for clouds in adjacent levels and random overlap for clouds separated by clear levels:

$$C_{P,k} = 1 - \Big(\frac{(1 - C_{P,k-1})(1 - \max(C_k, C_{k-1}))}{1 - \min(C_{k-1}, 1 - \epsilon)}\Big) \tag{3.28}$$

(for a more detailed description see the IFS Documentation, Cy40r1, Part IV: Physical Processes)
The clear sky precipitation fraction is then given by:

$$C_P^{clr} = C_P - C \tag{3.29}$$

where C is the cloud cover, defined as:

$$C = \frac{1}{V}\int_V \delta dV, \qquad \delta = \begin{cases} 1, & \text{in clouds} \\ 0, & \text{otherwise} \end{cases} \tag{3.30}$$

From eq. (3.28) it is clear that the precipitation fraction is a diagnostic variable strictly related to the cloud fraction. This faces a problem considering that rain and snow are prognostic variables with a finite fall speed, because they can be advected by the wind to areas outside the grid-cell in which they were produced. For this reason a precipitation fraction is specified, with the minimum value of 30%, for areas with no cloud fraction above.
According to the parameterization proposed by Kessler, evaporation occurs in the part of the grid-box where no cloud is present.
Defining q_e, with $0 < q_e < q_v$ as

$$q_e = \max\left\{\left(\frac{q_v - Cq_{sat}}{1-C}\right), 0\right\} \tag{3.31}$$

and the mean fall speed of rain drops as

$$V_{rain} = \alpha_2(\rho_{rain}^{clr})^{1/8}\sqrt{\frac{p}{p_0}} \tag{3.32}$$

where ρ_{rain}^{clr} is the density of rain in clear air defined as

$$\rho_{rain}^{clr} = \frac{P_{clr}}{V_{rain}} \tag{3.33}$$

$$= \frac{P_{clr}}{\alpha_2(\rho_{rain}^{clr})^{1/8}}\sqrt{\frac{p_0}{p}} \tag{3.34}$$

$$= \left(\frac{\sqrt{\frac{p_0}{p}}P_{clr}}{\alpha_2}\right)^{8/9} \tag{3.35}$$

Following Kessler (1969) the evaporation rate of rain is given by:

$$\frac{\partial q_v}{\partial t} = C_P^{clr} \quad \alpha_1(q_{sat} - q_e)(\rho_{rain}^{clr})^{13/20} \tag{3.36}$$

$$= C_P^{clr} \quad \alpha_1(q_{sat} - q_e)\left(\left(\frac{\sqrt{\frac{p_0}{p}}P_{clr}}{\alpha_2}\right)^{8/9}\right)^{13/20} \tag{3.37}$$

$$= C_P^{clr} \quad \alpha_1(q_{sat} - q_e)\left(\frac{\sqrt{\frac{p_0}{p}}P_{clr}}{\alpha_2}\right)^{0.5777} \tag{3.38}$$

where $\alpha_1 = 5.44 \cdot 10^{-4}\mathrm{s}^{-1}$ and $\alpha_2 = 5.09 \cdot 10^{-3}$.
Defining a critical humidity RH_{crit} as

$$RH_{crit} = RH_{max} + (1 - RH_{max}) \cdot \frac{C_P^{clr}}{(1-C)} \tag{3.39}$$

the scheme imposes a limit for the environmental humidity, in order to allow evaporation of rain and snow only when the grid mean relativity humidity is below a threshold value, to prevent the grid-box saturating when evaporation is limited to a part of the grid-box: $q_e < RH_{crit} \cdot q_{sat}$.

3.2.10 Superstaturation with respect to ice and ice nucleation

The liquid water and ice saturation ratios are defined as:

$$S_w = \frac{e}{e_{sw}} \tag{3.40}$$

$$S_i = \frac{e}{e_{si}} \tag{3.41}$$

At cold temperatures, the difference between the liquid water and ice saturation vapour pressures become significant and large ice supersaturations are possible, and the relative humidity with respect to ice can exceeds 150% before the activation of the nucleation process. These large saturation ratios over ice (1.4-1.7 in the temperature range 235-195 K)(e.g. Tabazadeh et al., 2000; Koop et al., 2000) are required by the homogeneous freezing in order to occur. For temperatures below the homogeneous nucleation temperature (defined as -38°C), the cloud scheme makes some assumptions to allow the supersaturation with respect to ice in the clear-sky portion of the grid-cell. Koop et al 2000 have studied the value of the relative humidity at which homogeneous ice nucleation initiates and it has been empirically rearranged by Kärcher and Lohmann (2002) giving the relation:

$$RH_{homo} = 2.583 - \frac{T}{207.8} \tag{3.42}$$

When this threshold is *locally* reached, ice nucleation is assumed to initiate. However, as the clear-sky humidity fluctuations are assumed to be uniformly distributed with a fixed constant variance, nucleation can occur when the grid-mean RH exceeds a threshold that is lower than this local criterion, and is given by $RH_{crit} \cdot RH_{homo}$.

For temperatures warmer than $-38°C$, when supercooled liquid and ice are coexistent, the liquid water saturation mixing ratio can be lower than this threshold and the cloud formation over a timestep results entirely in liquid cloud.

Cloud formation thus occurs when

$$RH > RH_{crit} \cdot \min\left(RH_{homo}, \frac{q_{sw}}{q_{si}}\right) \tag{3.43}$$

For temperatures lower than -38°C the deposition process is considered to be sufficiently rapid relative to the model time-step that it can be approximated by a diagnostic adjustment to exactly ice saturated conditions inside the cloud.

3.2.11 Growth of cloud ice by vapor deposition in mixed phase clouds (T>-38°C)

Below the homogeneous nucleation threshold of -38°C water droplets are assumed to freeze instantaneously. When, for temperature above this threshold, supercooled water and ice are allowed to coexist, they are assumed to be well mixed and distributed uniformly through the cloud.

The ice crystal is then assumed to grow at the expense of the water droplets through the Wegener-Bergeron-Findeisen process. This process occurs when the vapour pressure falls between the saturation vapour pressure over water and the saturation water pressure over ice, thus when $e_{si} < e < e_{sw}$. Air is then supersaturated with respect to ice and subsaturated with respect to water. This results in a rapid evaporation of liquid water and rapid ice crystal growth through vapour deposition. The process continues with ice growth until the water droplets are completely evaporated.

The deposition process is therefore a sink of liquid cloud and a source of ice cloud. Following Rotstayn et al. (2000) the growth rate of an ice crystal of mass M_i is given by

$$\frac{dM_i}{dt} = \frac{4\pi C(S_i - 1)}{A'' + B''} \tag{3.44}$$

where C is the capacitance of the particle and

$$A'' = \frac{L_s}{K_a T}\Big(\frac{L_s}{R_v T} - 1\Big) \tag{3.45}$$

represents the heat conduction, being K_a the heat conductivity of air.

The other therm, $B'' = R_v T/\chi e_{si}$, represents the vapor diffusion, and χ is the diffusivity of water vapor in air, which is inversely proportional to the pressure as $\chi = 2.21/p$.

If N_i is the concentration of ice crystals at a grid point and each particle is assumed to have a mass M_i, the local cloud ice mixing ratio is $q_i = N_i M_i/\rho$. If the air is at water saturation, so that $S_i - 1 = \frac{e_{sw} - e_{si}}{e_{si}}$ and the rate of change of q_i is then:

$$\frac{dq_i}{dt} = \frac{N_i}{\rho}\frac{4\pi C(e_{sw} - e_{si})}{e_{si}(A'' + B'')} \tag{3.46}$$

Considering the crystals with spherical shape of diameter D_i and constant density ρ_i, the capacitance C is equal to $D_i/2$, where $D_i = (6M_i/\pi\rho_i)^{1/3}$.

The equation becomes then:

$$\frac{dq_i}{dt} = 7.8\Big(\frac{N_i}{\rho}\Big)^{2/3} \frac{q_i^{1/3}(e_{sw} - e_{si})}{e_{si}(A'' + B'')\rho_i^{1/3}} \tag{3.47}$$

The change of temperature during a time step, due to the release of latent heat of fusion, is very small and can be assumed to be constant for simplicity. Integrating the last () with respect to time yields:

$$q_i(t) = \Big(\frac{2}{3}c_{vd}^{st} + q_{i0}^{2/3}\Big)^{3/2}, \tag{3.48}$$

where

$$c_{vd}^{st} = 7.8\Big(\frac{N_i}{\rho}\Big)^{2/3} \frac{(e_{sw} - e_{si})}{\rho_i^{1/3} e_{si}(A'' + B'')} \tag{3.49}$$

and $q_{i0} = M_{i0}N_i/\rho$ is the initial mixing ratio of cloud ice in the part of the cloud that contains supercooled liquid water. Following Rutledge and Hobbs (1983) it is assumed that $M_{i0} = 10^{-12}$ kg, while according to Ryan et al. (1976) a reasonable value for ice crystal density is $\rho_i = 700$ Kg m^{-3}.

3.2.12 Freezing

All rain freezes in a timestep if the temperature is lower than 0°C. This process represents a sink for rain and a source for snow. Since freezing would lead to an increase of temperature due to the latent heating of the process an expedient ensures that the temperature does not overcome the 0°C threshold.

3.2.13 Melting

The melting of ice and snow is parameterized taking also the cooling due to the evaporation of the liquid water during the melting process. Therefore, instead of the dry-bulb temperature, the wet-bulb temperature is used. Melting occurs if the wet-bulb temperature is greater than 0°C. The part of the box containing precipitation is allowed to cool to T_{melt}=0 °C over a time scale τ. The rate of change of liquid and rain is for this process given by:

$$\frac{\partial q_l}{\partial t} = \frac{c_p}{L_f}\frac{T_w - T_{melt}}{\tau} \tag{3.50}$$

where

$$\tau = \frac{\tau_m}{1 + 0.5(T_w - T_{melt})} \tag{3.51}$$

where τ_m=11800 s and the wet-bulb temperature T_w is a numerical approximation suggested by Wilson and Ballard (1999):

$$T_w = T_d - (q_s - q)(1329.31 + 0.00746(p - 085 \cdot 10^{-3}) - 40.637(T_d - 275)) \quad (3.52)$$

function of the subsaturation $q_s - q$ and of the pressure p.
This process represents a source of cloud liquid water and rain at expense of ice and snow respectively.

3.2.14 Sedimentation

The scheme allows the precipitating categories (rain, snow and ice) to sediment with a fixed fall speed that is assumed to be constant (for the rain w_r=4 m s^{-1}, for the snow w_s=1 m s^{-1} and for the ice w_i=0.15 m s^{-1}).
The numerical formulation of the sedimentation follows an implicit upstream approach, as shown in (3.3).

Chapter 4

Cloud simulations and sensitivities tests

As outlined in the introduction, the primary objectives for the implementation of a new large-scale microphysics cloud scheme can be summarised as following:

- a more physically based representation of the microphysics, with a separate treatment of cold and warm clouds, allowing the representation of mixed-phase clouds;
- a prognostic treatment of the precipitating categories, allowing them to be advected by the wind;
- a robust fully implicit numerical framework that allows the use of longer timesteps to retain efficiency.

Keeping in mind these main objectives, the discussion of the results will be divided into three parts: a first part will focus on the evaluation of the distributions of the main microphysical quantities, such as the liquid and ice water mixing ratios and the relative fractions. A second part will discuss the new prognostic approach analysing a wind event over the Alpine domain, showing how the new prognostic approach affects the precipitation pattern distribution. The third part presents a series of sensitivity tests to understand how the moisture and radiation quantities respond to the variation of the microphysical parameters used in the scheme, such as the fall speeds of the falling categories, the autoconversion scheme and the evaporation coefficient.

4.1 The microphysics

An appropriate representation of the mixing ratios distributions as functions of temperature and height is the first important step to be investigated in order to prove that the cloud microphysics is properly reproduced by the scheme. To reach this aim a three-month simulation (JJA 2000) has been performed over the African domain, with an horizontal resolution of 50 km (shown in figure Figure 4.1). The initial and lateral boundary conditions are obtained from the new ERA-intereim 0.75°x0.75° reanalysis (Simmons et al., 2007; Dee et al., 2011) and convective clouds are parameterized by the mass flux convection scheme by Tiedtke (1989). The black square in the figure represents the area over which the plotted variables have been averaged. The reasons for choosing this region reside in the importance of improving its climatology representation: the West African monsoon event has been under study in the last decades since African Sahel provides the most dramatic example of multi-decadal climate variability that has been measured (Hulme, 2001).

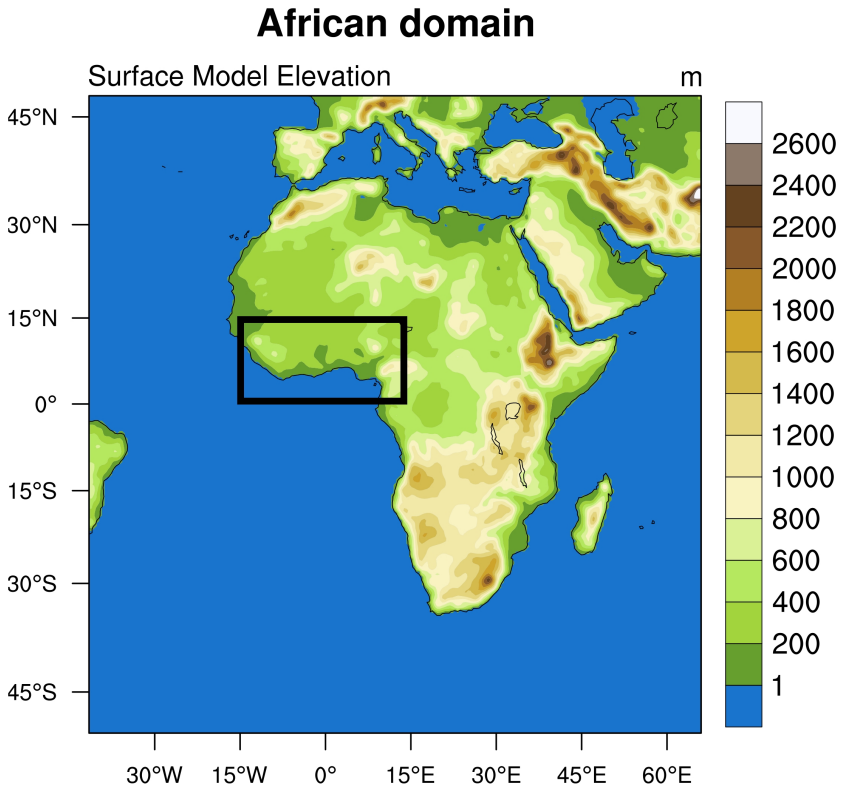

Figure 4.1: Domain used for the simulation. The box is the area over which the results are averaged.

Figures 4.2 and 4.3 show liquid water and ice contents obtained, averaged in time and in space over a selected box positioned on the Guinea coast, where the InterTropical Convergence Zone (ITCZ) is located during the northern hemisphere summer. The modelled contents show a realistic variation with temperature and pressure and exhibit the allowance of mixed-phase clouds: supercooled liquid water coexists with ice for temperature greater than -38°C, that is the threshold temperature for homogeneous freezing. Small ice fractions at temperature greater than 0°C are due to the fact that ice is allowed to fall with a finite fall speed and takes time to melt.

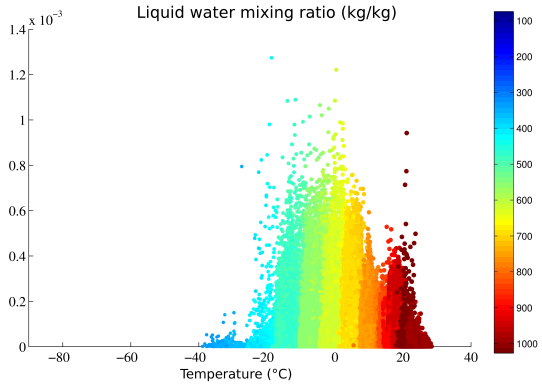

Figure 4.2: Liquid water scatter plot as a function of temperature (°C) and pressure (hPa).

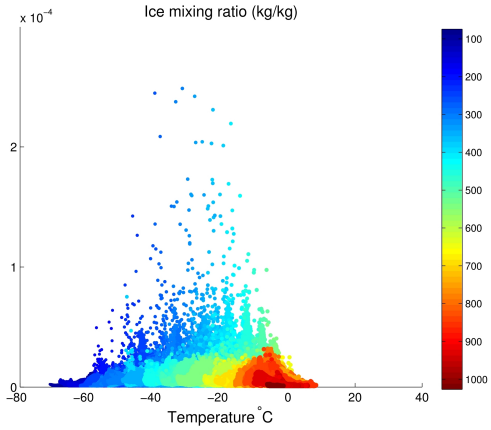

Figure 4.3: Cloud ice scatter plot as a function of temperature (°C) and pressure (hPa).

The liquid water fraction represents the partition between liquid and ice in mixed phase clouds and is defined as:

$$f_l = \frac{q_l}{q_l + q_i} \tag{4.1}$$

and is therefore equal to 1 when only liquid is present in the cloud, and equal to 0 when only ice exists. The liquid water fraction generated by the previous diagnostic temperature-dependent scheme to be passed to the radiation scheme, is plotted as a function of temperature in 4.4, with colour dots representing data from different level pressures. The figure shows that below -30°C all of the clouds are completely glaciated while above -10°C the clouds are made of only liquid. Moreover, at each temperature only one liquid water fraction characterises the cloud existing at each altitude level.

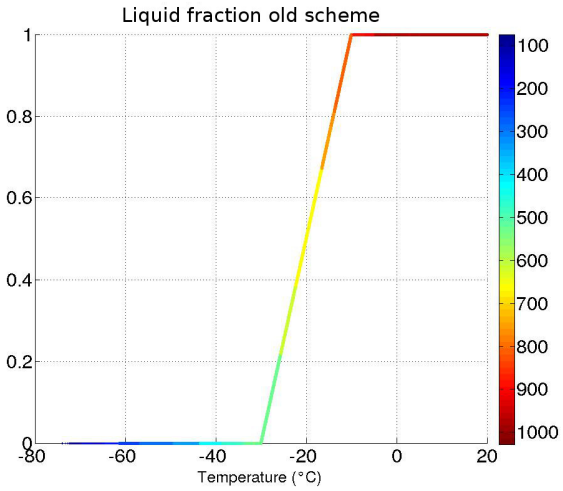

Figure 4.4: Liquid water fraction cloud condensate for the previous diagnostic temperature-dependent mixed-phase scheme SUBEX scheme in the West African JJA 2000 as a function of temperature (°C) and pressure (hPa).

Figure 4.5 shows the liquid water fraction generated by the new prognostic microphysics scheme. As measurements for this period over the West African domain are not available, aircraft observations taken in frontal stratiform clouds by the UKMO Meteorological Research Flight are taken and drawn in Figure 4.6 to compare the distribution of the liquid water fraction as a function of temperature. The liquid water fractions obtained with the new scheme look realistic when compared with observations. Compared to the previous scheme, which was setting automatically to zero all the liquid water below -30°C, this scheme allows the existence of liquid water at temperatures lower than that threshold. It also allows the existence of ice for temperatures greater than -10°C and liquid water fractions different from 1 even at temperatures greater than 0°C since, as seen in 4.3, ice falls and takes a finite time to melt. At each temperature, with the new scheme, coexists a wider variability of clouds: for

example at -15°C the clouds can vary from all ice to all water through varying fractions of supercooled liquid water.

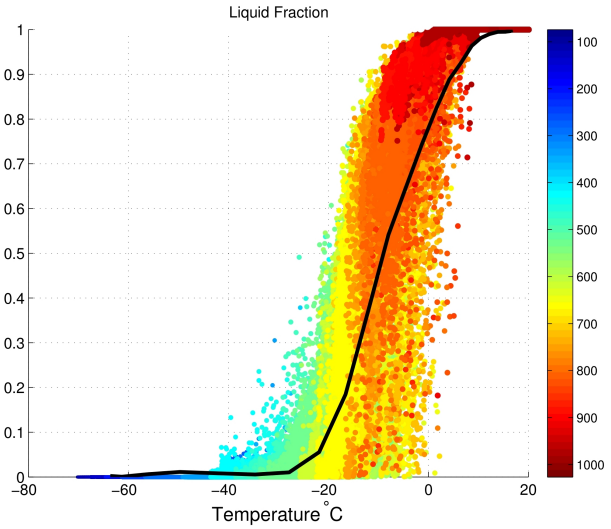

Figure 4.5: Liquid water fraction cloud condensate for the new prognostic microphysics scheme as a function of temperature (°C) and pressure (hPa). Solid black line represents the horizontal spatial average of the liquid water of the West African JJA 2000.

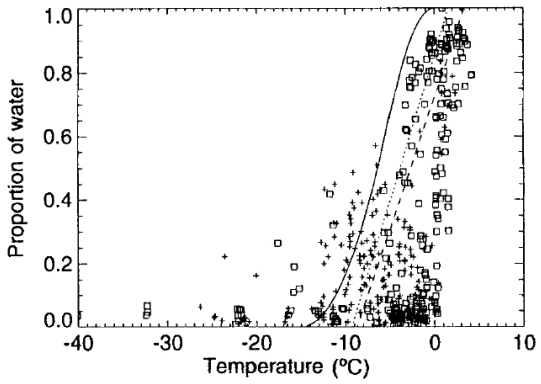

Figure 4.6: Plot of aircraft observations of the proportion of liquid water as a function of temperature in stratiform clouds. Crosses indicate clouds in continental air masses and squares indicate clouds in maritime air masses. Source: Rotstayn (1997)

To focus on the vertical moisture more closely, the relative humidity, the liquid water mixing ratio (and ice mixing ratio for the new parameterization) and cloud cover obtained using the old and the new scheme are shown in Figures 4.7 and 4.8 respectively. Figure 4.9 shows the same quantities as produced by the reanalyses ERA Interim (Dee et al., 2011) for the same area (the box indicated in Figure 4.1) and for the same period (JJA 2000). The new relative humidity

profile has improved respect to that obtained with the SUBEX parameterization as it is able to reproduce the minima and the maxima of relative humidity represented by the reanalyses (minimum at 400 hPa and maximum at the top of the troposphere and at 900 hPa). The old scheme reproduces a too moist middle troposphere with relative humidities almost constant along the column with values around 70%. Both the previous and the new schemes are too moist at the top of the troposphere, reaching peaks of $\sim 90\%$ while the reanalyses locate the peak at $\sim 70\%$. This peak consists of the detrainment coming from the convective activity and represents a link between the convective clouds scheme and the new large-scale cloud scheme.

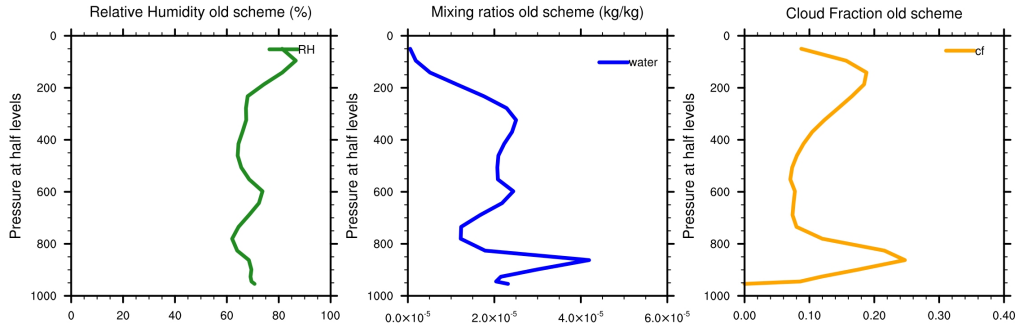

Figure 4.7: Vertical profile, obtained with the old scheme of the relative humidity, liquid water mixing ratio (in kg/kg) and cloud fraction for the JJA 2000 simulation averaged over the box indicated in Figure 4.1.

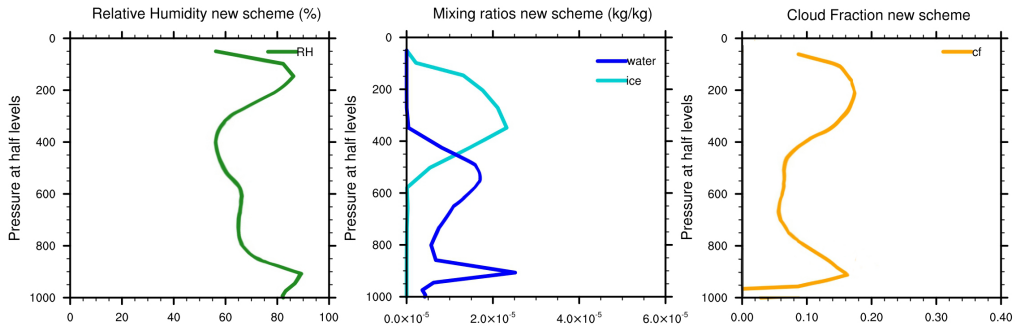

Figure 4.8: Same as Figure 4.7 but for the new scheme.

The bulges in RH are consistent with the cloud fraction, that shows two peaks for both the new and the old schemes, one at 900 and one between 400 and 200 hPa, corresponding to the shallow convective activity and the detrainment level of deep convection. The anvil cloud associated with the deep convection

covers about the 20% of the domain. This small value is justified by the fact that the considered box is wider than the region of convective activity, including parts of clear sky. For both the schemes the profile of the cloud fraction is consistent with the vertical profile of the predicted mixing ratios. However, the comparison with the reanalyses shows that the new cloud fraction at low levels is improved as the old scheme tended to overestimate the shallow convection peak.

The mixing ratios vertical profiles obtained with the new scheme show a reasonable distribution of liquid and ice with height as ice melts for temperatures greater than 0°C at 600 hPa while supercooled liquid droplets coexist with ice above the homogeneous freezing threshold. The comparison with the reanalyses shows an overestimation of the ice mixing ratio and an underestimation of the liquid water mixing ratio for the new scheme at low levels, and an overestimation of the liquid water mixing ratio at higher levels for the old scheme.

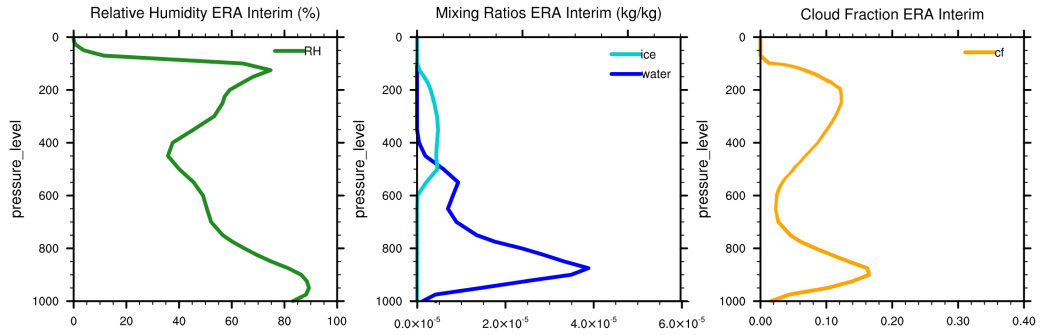

Figure 4.9: ERA-Interim reanalysis atmospheric relative humidity, mixing ratios of water and ice and cloud fraction as functions of pressure for JJA 2000 (Dee et al., 2011).

4.2 Test cases - the prognostic approach

In order to evaluate the differences given by implementing a prognostic precipitation, a south-westerly wind event associated with a cyclonic atmospherical configuration over the southern United Kingdom has been selected from the 2000-2001 European winter. As the precipitation is now a prognostic variable the rain and the snow are stored from time step to time step and are advected by the wind. The considered domain is centred on the Alps, with an horizontal resolution of 20 km using the semi-lagrangian advection scheme presented in

Diro et al. (2013). The choice of this region is due to the fact that the advection of precipitation can be more significant in regions of orographic forcing; the choice of the period, as well as for the occurrence of a strong south-westerly wind event, is related to the presence of the snow that has a lower fall speed respect to rain and hence is more subjected to the advection. The impact of having a prognostic precipitation is therefore expected to be more pronounced. As the new scheme still needs to undergo a tuning procedure, the comparison with the old scheme precipitation and with observations is beyond the scope of this section. The idea of this test is to appreciate that a prognostic precipitation is not falling instantaneously and can be blown by the wind being subjected to a transportation.

In order to appreciate the differences given by the prognostic approach, Figure 4.10 shows in the upper panel (a) the precipitation (mm/day) and surface winds (m/s) obtained in a "simulated diagnostic" experiment, in which the new scheme is used having switched off the advection of the rain and of the snow. Figure 4.10 (b), displays the precipitation and surface winds obtained with the new scheme and active advection of rain and snow. Figure 4.10 (c) shows the difference of precipitation between the two experiments: the precipitation pattern changes from the "simulated diagnostic" to the prognostic scheme as the precipitation subjected to advection is able to reach the lee side of Alps instead of accumulating at the upwind side.

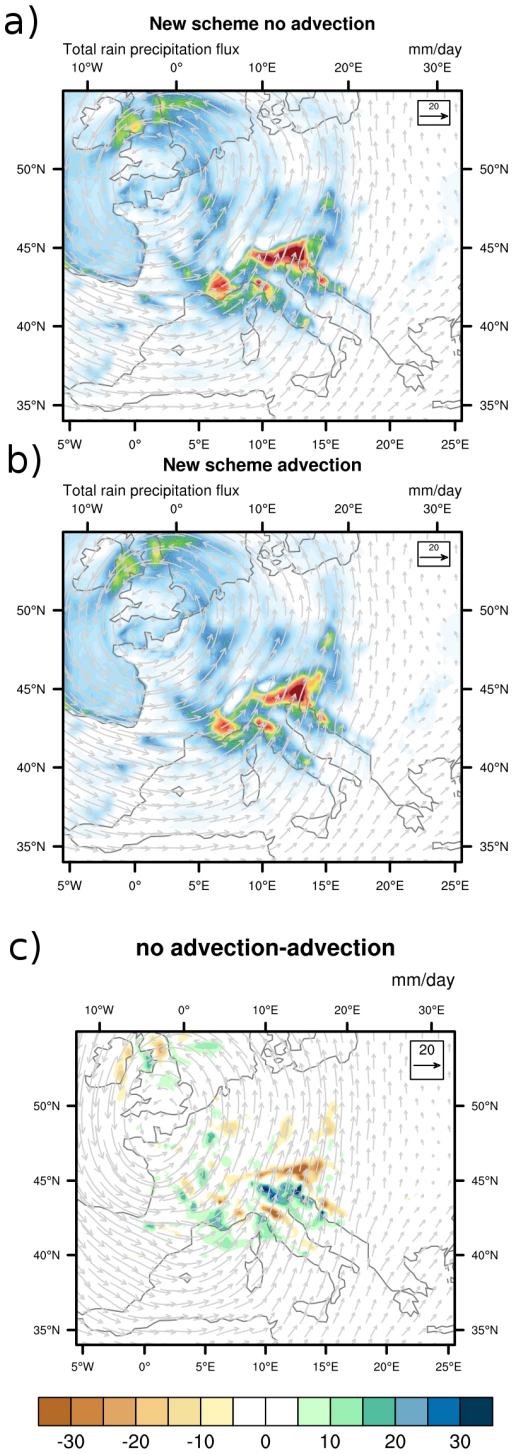

Figure 4.10: Total rain precipitation flux (in mm/day) and winds (m/s) for a south-westerly wind event over the Alps obtained using the new scheme without advection of rain and snow (plot a) and the new scheme with advected rain and snow (plot b). Plot c) shows the difference of precipitation (m/s).

4.3 Sensitivity tests

In order to determine how the simulated clouds depend on the variation of microphysics parameters a set of numerical experiments has been conducted over the tropical band to test the sensitivity of moisture and radiation variables to the change of the coefficients used in the autoconversion, evaporation and sedimentation parameterizations. The chosen domain is the entire tropical band (shown in Figure 4.11) with 23 vertical levels and a horizontal resolution of 100 km.

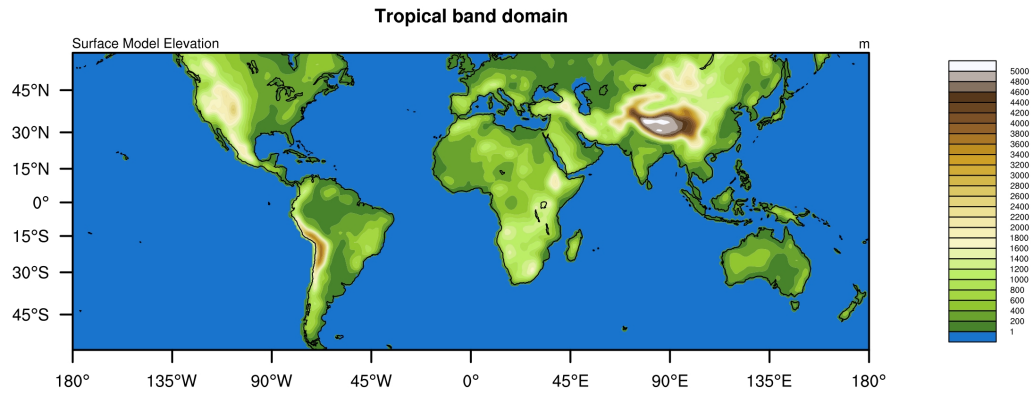

Figure 4.11: Domain used for the simulation.

At any run a single parameter has been modified to see the response of the following quantities:

- liquid water path;
- ice water path;
- cloud radiative forcing;
- precipitation.

The liquid water path is a measure of the total amount of liquid water contained in a vertical column of atmosphere. It represents a critical quantity for understanding the radiative transfer as it varies significantly depending on the type of clouds. Studying the sensitivity of the liquid water path is the most intuitive way to understand how the cloud optical properties change with the variation of some parameters used in the microphysics scheme, such as the fall speeds of the precipitating categories, the autoconversion parameterization choice, the coefficients for the autoconversion and evaporation processes.

The ice water path is a measure of the total amount of ice contained in a vertical column of atmosphere. Usually expressed in g/m^2, it also varies greatly from cloud to cloud and is particularly important for the radiation as cirrus clouds, mainly formed by ice, play an crucial role in the balance of the Earth's energy dynamics.
The cloud radiative forcing (CRF), as already introduced in Chapter 1, is the difference between the radiation budget F^{LW} and F^{SW} components in cloudy conditions and the radiation budget components in clear-sky conditions:

$$CRF_{net} = F^{LW}_{cloudy} - F^{LW}_{clear} + F^{SW}_{cloudy} - F^{SW}_{clear} \tag{4.2}$$

where F^{LW} and F^{SW} are the outgoing long wave and shortwave radiation respectively. The results from ERBE experiment (Barkstrom and Smith, 1986) quantify the global mean CRF ranging from approximately -14 to -21 W m^{-2}. The balance between the LW and SW components of the CRF depend on many factors, including the microphysical cloud properties (Ramanathan et al., 1989).

Sensitivity to the fall speeds

A series of 1-week simulations (first week of July 2000) has been performed assuming different values for the rain, snow and ice fall speed. For the rain, the chosen values are $v_1 = 1.0$ m/s, $v_2 = 4.0$ m/s, $v_3 = 8.0$ m/s and $v_4 = 12.0$ m/s. For the snow $v_1 = 0.1$ m/s, $v_2 = 1.0$ m/s, $v_3 = 2.0$ m/s and $v_4 = 4.0$ m/s and for the ice $v_1 = 0.1$ m/s, $v_2 = 0.5$ m/s, $v_3 = 1$ m/s and $v_4 = 1.5$ m/s.
The sensitivities results are shown in Figure 4.12 - 4.16.
The parameter to which both the columnar water paths and the cloud radiative forcing seem to be more sensitive is the value of the ice fall speed (Figure 4.12). Increasing the fall speed of ice removes ice faster and less ice remains suspended in the atmospheric column. The ice water path is thus reduced and the same is experienced by the liquid water content due to the removal of an important source of liquid through the ice melting.

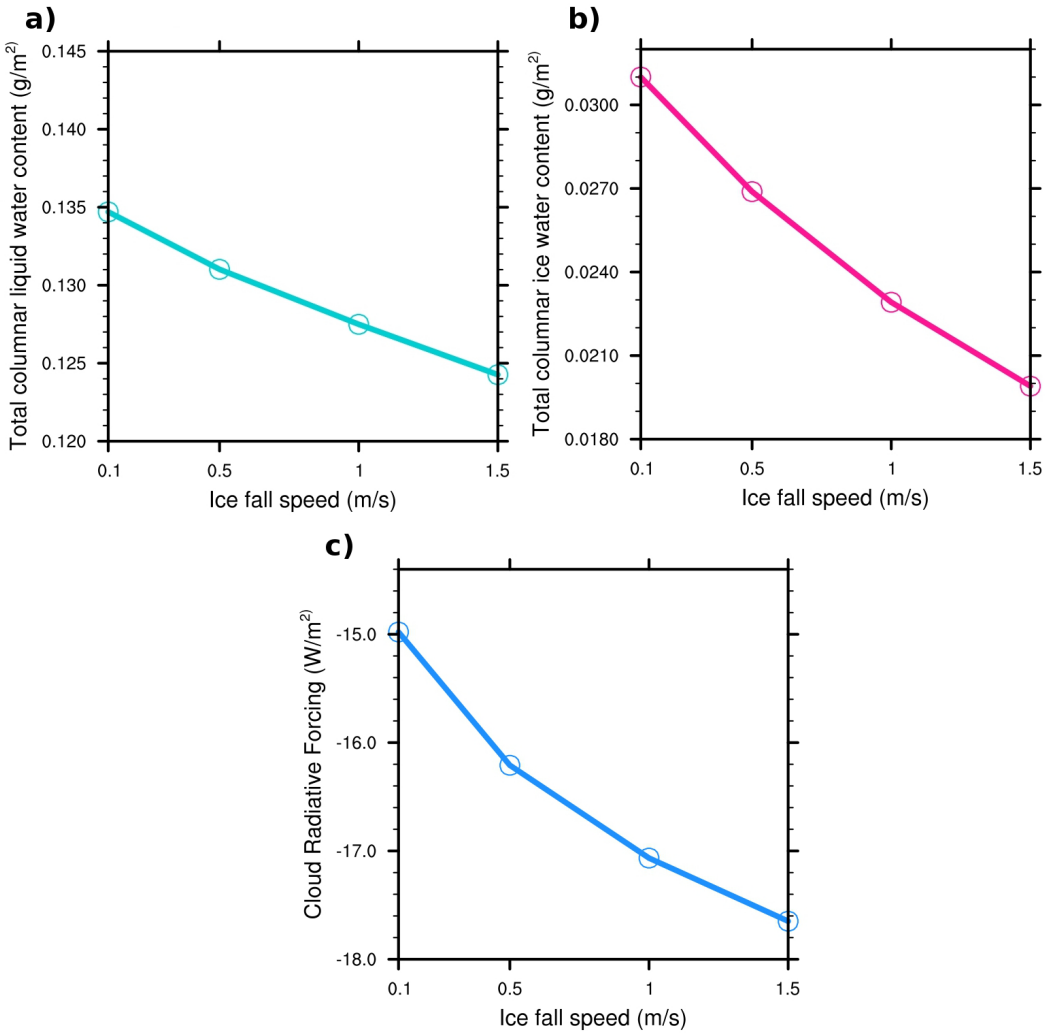

Figure 4.12: Sensitivity of the liquid water path (a), ice water path (b) and cloud radiative forcing (c) to the change in ice fall speed.

The reasons for which the cloud radiative forcing decreases as the ice fall speed increases are more complex and need to be investigated further by understanding how the liquid and ice water optical thicknesses change for both high (100-400 hPa), medium (450-700 hPa) and low (700-1000 hPa) clouds (Figure 4.13) because, as already introduced in Chapter 1, high and low clouds play a different role in the radiation budget. Figure 4.13 shows that while for high and for medium clouds, (a)-(b)-(c) and (d), both ice and liquid decrease, for low clouds, (e) and (f), the liquid water increases because of the amount of ice falling faster from above and melting in the lower layers. Low clouds result therefore to be optically thicker and reflect more solar radiation, giving rise to a lower net SW radiation in cloudy conditions F^{SW}_{cloudy} and thereby to a lower

CRF.

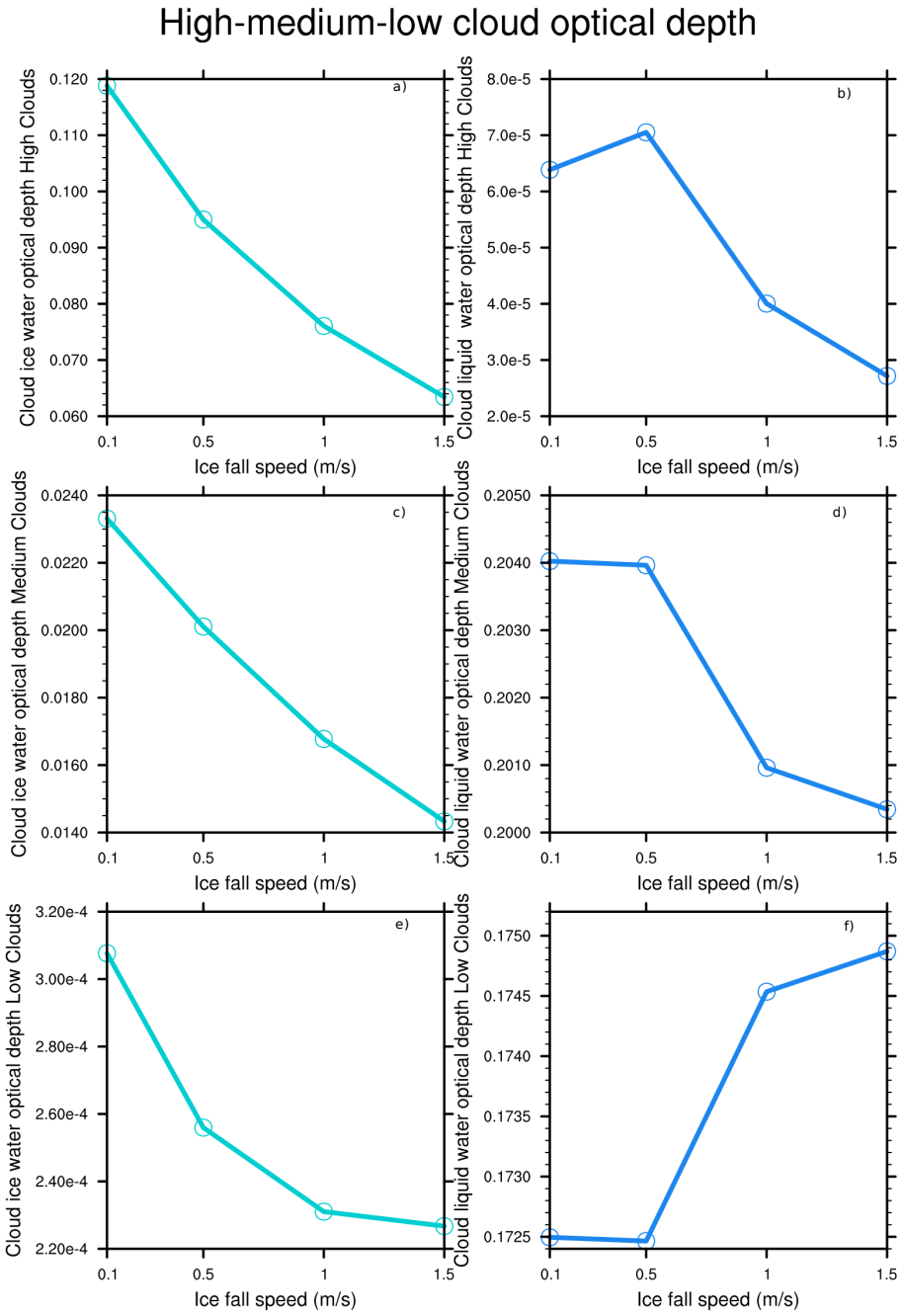

Figure 4.13: Sensitivity to the ice fall speed of the cloud ice water optical depth for high clouds (a) and for low clouds (c), and of the cloud liquid optical depth for high clouds (b) and low clouds (d).

The ice fall speed, respect to snow and rain fall speeds, is also the parameter to which the precipitation is more sensitive (see Figure 4.16 (a), (b) and (c)): as the ice speed increases the precipitation increases over the band. This is in

line with the trend of ice water and liquid water paths shown in 4.12 a) and b). Moreover higher ice fall speeds not only reduce the amount of ice in the atmospheric column, but also the snow by inhibiting the snow autoconversion. Figure 4.14, shows the variation in snow mixing ratios (a) and ice mixing ratios (b) with different fall speeds.

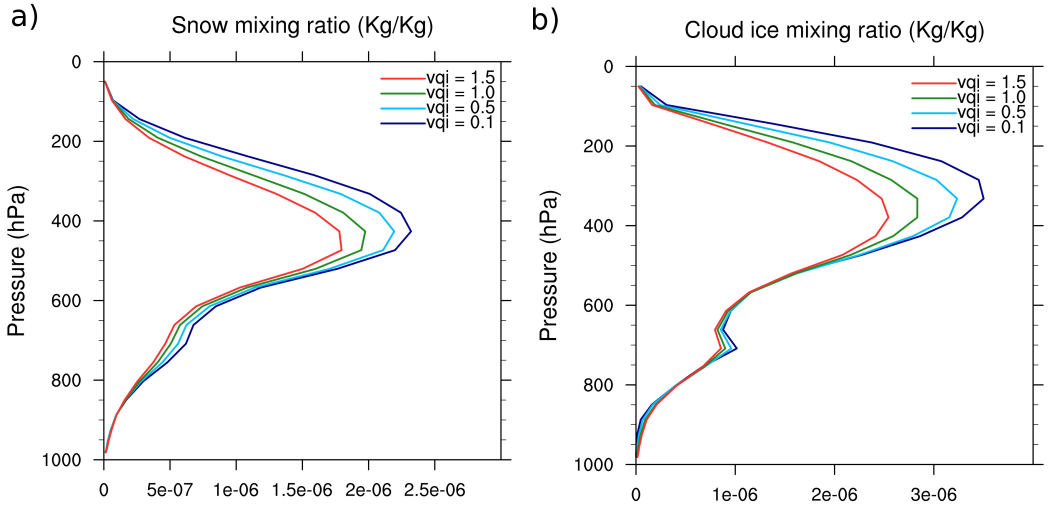

Figure 4.14: Sensitivity of the snow mixing ratio (a) and cloud ice mixing ratio (b) to the variation of the ice fall speed.

The sensitivity of the precipitation to the rain fall speed is much smaller, as the fall speeds are so fast that the majority of the rain falls out the column within a timestep. As a consequence the sensitivity to the coefficient of evaporation of rain is also not pronounced (see 4.16 (f)). It is important to highlight that the same behaviour would not be the case for higher resolution simulations and further analyses need to be done in view of the forthcoming increasing resolution due to the inclusion of a non-hydrostatic core for RegCM4.
Precipitation is also sensitive to the snow fall speed: as the snow fall speed increases the precipitation increases while the ice and liquid water content do not vary significantly (see Figure 4.15). This happens because as the snow falls faster, it is less subjected to evaporation and therefore contributes to an increase in the precipitation without altering the ice and the liquid categories.

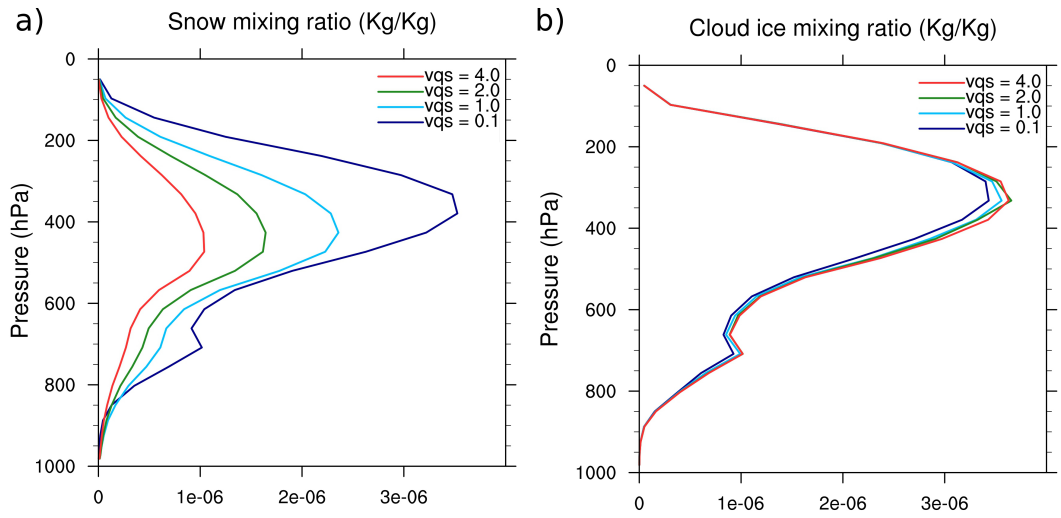

Figure 4.15: Sensitivity of the snow mixing ratio (a) and cloud ice mixing ratio (b) to the variation of the snow fall speed.

Sensitivity to the autoconversion scheme

It may be useful to recall that the autoconversion is the process that is responsible for the formation of rain at the expense of the cloud droplets. An overview of the differences in the efficiencies of the four options for the autoconversion parameterization implemented in the scheme is presented in Figure 3.3.
In Figure 4.16 (d) it is possible to notice that the predicted amounts of precipitation are weakly sensitive to the choice of the autoconversion scheme, as with the chosen timestep, dt=120 s most of the cloud water is converted into rain. For all the considered regions the Sundqvist conversion scheme represents the moistest one. This is due to the fact that the Sundqvist scheme for autoconversion is the only, in the options range, that explicitly treats the accretion of raindrops (see 3.22 and 3.23). Because of the threshold form of Sundqvist parameterization for autoconversion, another parameter taken into account for the sensitivity test is the threshold value q_l^{crit} at which the cloud droplets starts to form the rain. Figure 4.16 (e) shows that as this value increases the precipitation decreases as expected.

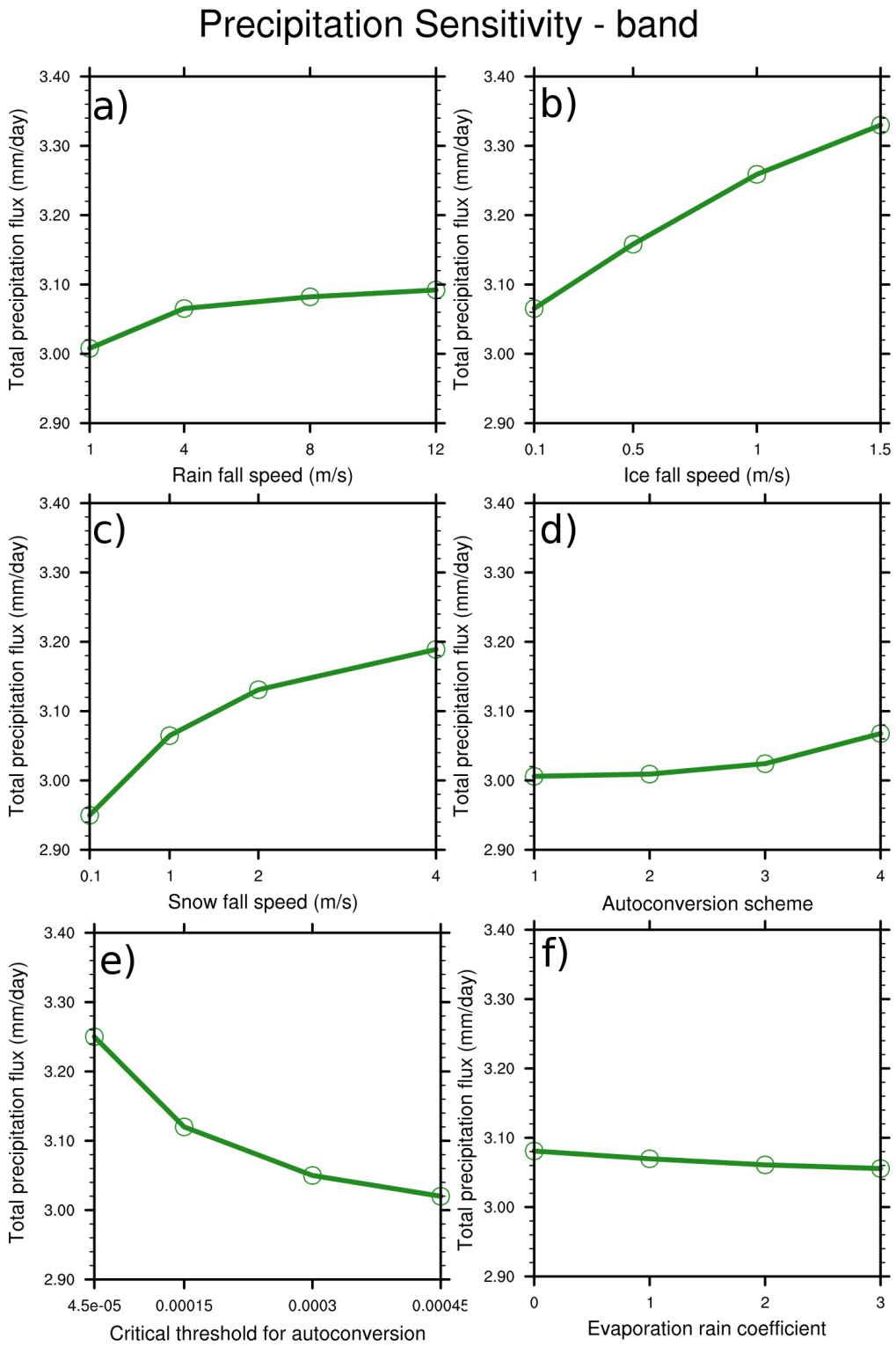

Figure 4.16: Sensitivity of the total tropical band mean precipitation flux (in mm/day) to the rain, ice and snow fall speeds, to the choice of the autoconversion scheme (1=Pincus and Klein (2000) , 2= Khairoutdinov and Kogan (2000) , 3=Kessler(1969), 4=Sundqvist (1978)), to the Sudqvist threshold value for the liquid water and to the evaporation coefficient.

Chapter 5

Evaluation through the CFMIP Observation Simulator Package

Satellites provide a representative global sample of all meteorological conditions and therefore are helpful tools to evaluate the subgrid processes such as the microphysics of clouds. The comparison of modelled data with satellites data is however not trivial as satellites do not measure directly the modelled quantities but the intensity of radiation coming from a particular area and direction in a particular wavelength range from the ultraviolet (10^{-7} m) to radio frequencies (1 m). Inverse modelling, generally called satellite retrievals, is used to get information about many geophysical quantities such as water vapour, atmospheric temperature, cloud properties and land surface products (Randel et al., 1996; Schaaf et al., 2002) from the measured radiation. The comparison of the extracted variables and modelled variables can be nevertheless ambiguous because of the difference in definitions of the variables under study between the models and the satellite retrievals. Moreover satellite measurements have limitations due to the finite sensitivity of the instruments, bringing uncertainties into the retrievals.

In the last two decades a new approach has been proposed by the development of what are called "simulators": tools able to rewrite models outputs miming the observational processes, taking into account instrument's biases (e.g. Yu et al., 1996) and therefore minimising the effects of different definitions and observational limitations. This method guarantees that differences between models and observations are mainly due to model problems rather than satellite artefacts, and constitutes an optimal tool for modelled clouds evaluation.

Despite the previous diagnostic scheme, the new microphysics cloud schemes provides all the needed variables to allow a proper evaluation of the simulated clouds. A thorough evaluation of both the stratiform and convective clouds modelled by RegCM4 is undertaken in the next sections, preceded by a description of the CFMIP Observation Simulator Package COSP and of the satellites used for the validation.

5.1 Description of COSP

The Cloud Feedback Model Intercomparison Project community has developed an integrated satellite simulator, the CFMIP Observation Simulator Package (COSP), that includes 5 observational products. Table 5.1 shows the datasets produced by each satellite's simulator included in the current version of COSP:

- the cloud profiling radar (CPR) on board *CloudSat* (Stephens et al., 2002);
- the Cloud-Aerosol Lidar with Orthogonal Polarization (CALIOP) lidar on board Cloud-Aerosol Lidar and Infrared Pathfinder Satellite Observations, CALIPSO, (Winker et al., 2010);
- the International Satellite Cloud Climatology Project, ISCCP (Rossow and Schiffer, 1999);
- the Multi-angle Imaging SpectroRadiometer, MISR (Diner et al., 1998);
- the Moderate Resolution Imaging Spectroradiometer, MODIS (King et al., 2003).

COSP is a tool that receives in input the gridbox mean vertical profiles of temperature, humidity, hydrometeor mixing ratios, cloud optical depths, emissivities, surface temperature, pressure from the model output and therefore produces a new rewritten output that is comparable with the satellites data. The production line consists in three steps (see the scheme in Figure 5.1):

1. COSP addresses the mismatch between the scale of the climate model's grid box (usually of sizes up to 150 km) and the scale of a satellite pixel by creating a fictitious subgrid variability: through the SCOPS software, Klein and Jakob (1999), it breaks each gridbox mean profile into subcolumns in which the cloud fraction is assigned to be zero or one at

every model level. At each model level, for each subcolumn the choice between a overcast or clear grid is entirely consistent with the cloud overlap assumption used by the model. As already specified, in the case of maximum-random overlap clouds in adjacent levels are maximally overlapped; therefore clouds are assigned to those subcolumns that contain clouds in the layer immediately above rather than to those subcolumns that do not contain cloud in the layer immediately above. Moreover the assignment of cloudy subcolumns begins from the subcolumn farthest to the "left" that fulfills the previous condition. Each cloudy subcolumn is subsequently filled with the same amount of condensate, assuming a constant in-cloud water and ice l^k_{cld} within the subcolumns, defined as

$$l^k_{cld} = \frac{l^k}{a^k_{int}} \tag{5.1}$$

where l^k is the total condensate for the level k and a^k_{int} the fraction of sub columns at each level that contain cloud. For a more detailed treatment of the SCOPS software please refer to Klein and Jakob (1999).

2. The subcolumn's profiles are passed to each satellite's simulator; for each simulator a different algorithm is applied to calculate the signal that the satellites would have observed if they were flying above an atmosphere similar to that predicted by the model.

3. Statistical modules collect the outputs from all the instruments and build diagnostics that can be compared to observations.

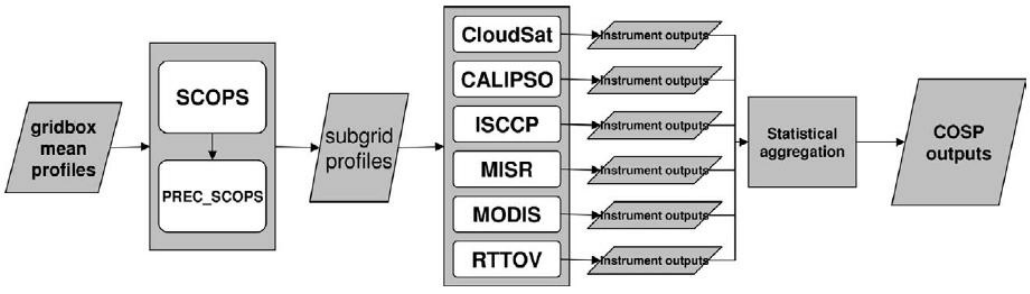

Figure 5.1: COSP schematic. Source: Bodas-Salcedo et al. (2011)

Simulator	Output diagnostics
CloudSat	Radar reflectivity
	Height-reflectivity histograms
CALIPSO	Low-level cloud fraction (CTP $>$ 680 hPa)
	Midlevel cloud fraction (440$<$CTP$<$680 hPa)
	High-level cloud fraction (CTP$>$440 hPa)
	3D cloud fraction
	Total cloud fraction
ISCCP	Mean cloud albedo
	Mean cloud optical depth
	Total cloud fraction
	CTP-τ histograms
MISR	CTH-τ histograms
MODIS	Total cloud fraction
	Liquid cloud fraction
	Ice cloud fraction
	High-level cloud fraction
	Midlevel cloud fraction
	Low-level cloud fraction
	Total cloud optical depth
	Liquid cloud optical depth
	Ice cloud optical depth
	CTP-τ histograms
	Cloud liquid water path
	Cloud ice water path
	Cloud area fraction

Table 5.1: List of diagnostics for each simulator available in COSP version 1.3

5.2 Description of the satellite instruments

Before introducing the satellite's instruments used for the evaluation of RegCM4, it is important to recall that there are two different types of satellite sensors: active and passive sensors. Active sensors emit radiation towards the earth surface, in order to monitor the atmospheric features. Radar satellites for example use short pulses of electromagnetic radiation in the microwave spectral range and they record the signal reflected and retrieve information on the structure of the earth surface, or of the reflecting object the signal met while reaching the surface. Active sensors are for instance CloudSat and CALIPSO. Passive sensors do not emit their own radiation but detect reflected or radiated energy in the visible and infrared of the electromagnetic spectrum. Passive sensors are for instance ISCCP, MISR and MODIS.

5.2.1 ISCCP

The International Satellite Cloud Climatology Project (ISCCP) represents the first project of the World Climate Research Programme (WRCP) and constitutes the longest record of satellite-derived cloud properties available over a global coverage. With the basic objective of inferring the global distribution of cloud radiative properties in order to improve the modelling of cloud effects on climate it has been collecting, since 1983, the infrared (11μ m, 1-4-km resolution) and visible (0.6 μ m, 1-km resolution) radiances obtained from imaging radiometers. ISCCP assumes the cloud top radiates like a blackbody and entirely covers the satellite pixel. To derive the cloud top temperature it uses the observed infrared brightness temperature: using an atmospheric profile of temperature and pressure, the cloud top pressure is therefore inferred. The optical depth is retrieved from the observed visible radiance assuming a one-dimensional single-layer cloud with a fixed effective radius (10 μm for water and 30 μm for ice) and it does not consider the aerosols.
ISCCP first identifies whether a pixel is cloudy or cloud-free, it therefore retrieves the optical depth that is used to estimate the cloud emissivity, that is used to determine the cloud-top pressure. The key limitation in comparisons with models is that partly cloudy pixels are treated in ISCCP data as fully cloudy, and therefore ISCCP tends to overestimate clouds. The ISCCP

simulator used in COSP is described in Rossow et al. (1996).

5.2.2 MODIS

The Moderate Resolution Imaging Spectroradiometer (MODIS) is one of five instruments on board the Terra Earth Observing System (EOS) platform and the Aqua (EOS) satellites launched by NASA respectively in 1999 and in 2002. The instruments capture data in 36 spectral bands ranging in wavelength from 0.4 μm to 14.4 μm, and is able to determine whether a cloud is composed of ice or water particles (or both of them), the effective radius of the cloud particles, the temperature and altitude of cloud tops. In particular MODIS observes thin cirrus clouds with unprecedented sensitivity. A limitation of MODIS is that partly clouds pixels are excluded in current product version (Collection 5) and thus complicates comparisons with models. The algorithm used by MODIS to detect clouds is described in Platnick et al. (2003) and is based on a combination of two techniques: for clouds above about 700 hPa it determines the cloud top pressure through a CO_2 slicing technique while for low clouds the cloud top pressure is determined in a similar way to ISCCP, using NCEP Global Data Assimilation System temperature profiles (Menzel et al., 2008). The MODIS simulator used in COSP is described in Pincus et al. (2012).

5.2.3 MISR

As clouds do not reflect solar radiation uniformly in all directions, the Multi-angle Imaging SpectroRadiometer MISR, using nine cameras that span much of the range of angles over which cloud reflectivity varies, gives rise to a more accurate retrieved albedo than those observed from similar measurements with only a single camera looking straight down. Launched by NASA in 2000, MISR also flies aboard the Terra satellite and determines the cloud-top height and the cloud optical depth (only over ocean). MISR determines the cloud top height (CTH) using a stereo-imaging technique described in Muller et al. (2002). The MISR retrieval for optical depth is similar to that of ISCCP but it is only run over ocean surfaces and is based on observations at 865 nm. Naud et al. (2002) found that in case of multilayered clouds MISR stereo height often "sees" through the thin upper level clouds and refer to lower clouds lay-

ers. The MISR simulator used in COSP is described in Marchand et al. (2010).

5.2.4 CALIPSO

The Cloud-Aerosol Lidar and Infrared Pathfinder Satellite Observations CALIPSO satellite is a joint NASA (USA) and CNES (France) launched in April 2006. It comprises three instruments: (1) the Cloud-Aerosol Lidar with Orthogonal Polarization (CALIOP Lidar) that provides vertical profiles of aerosol and cloud backscatter, (2) an Imaging Infrared Radiometer (IIR) with three channels in the infrared window region optimised for retrievals of cirrus particle size, and (3) the Wide Field Camera (WFC), a low resolution imager with one visible channel which provides the meteorological context.
CALIOP operates with three channels: two at 532 nm and one at 1064 nm and provides three vertical profiles of the energy scattered back by aerosol and cloud particles at a range resolution of 15 m. The amount of energy scattered back is a measure of the concentration of scattering particles. The CALIPSO simulator used in COSP is described in Chepfer et al. (2008)

5.3 Evaluation of Tropical Cloud Properties

The implementation of the new microphysics scheme allows an evaluation of the mean state clouds in the RegCM4 model using multiple independent satellite datasets and their corresponding instrument simulators in COSP. The main goal of this study is to give an overview of how the model is able to represent the vertical and horizontal distribution of clouds and their optical depths.
In order to get a general overview of the model's ability in representing different types of clouds the chosen domain for the evaluation is the tropical band (180°W-180°E, 47°S-47°N). The model outputs analysed in this study are from the period May 2006-September 2007 at 100 km grid spacing and 23 vertical sigma levels and the initial and lateral boundary conditions are obtained from the new ERA-Interim 0.75°x0.75° reanalysis (Simmons et al., 2007; Dee et al., 2011). Of specific relevance to this study is the use of the mass flux convection scheme by Tiedtke (1989), the Biosphere-Atmosphere Transfer Scheme, BATS (Dickinson et al., 1993b) for land surface processes and the boundary layer scheme of Bretherton et al. (2004) that permits a realistic treatment of stratocumulus-capped boundary layers. The periods chosen for the analysis are the north-hemisphere winter season December 2006 to February 2007 (DJF) and the north-hemisphere summer season June to August 2007 (JJA), taking cue from the evaluation of clouds in ACCESS model by Franklin et al. (2013). The monthly mean COSP outputs are produced analysing each 6-hourly RegCM4 output and then averaging over the seasons. The number of subcolumns used does not depend on the horizontal resolution but on the amount of averaging on the outputs, and is set to 20, following the rule of thumb recommended by the authors.

5.3.1 ISCCP simulator

The ability of models to represent the space-time distribution of total cloud amount is perhaps the most important aspect of a model's ability to simulate clouds. The first evaluation of the total cloud cover was carried using the ISCCP D1 data sets (Rossow et al., 1996), averaged over JJA and DJF 2007 during the daytime, at a horizontal resolution of 2.5°x2.5°. Figure 5.2 illustrates observed ISCCP total cloud amounts for JJA and for DJF, a) and

c), and the clouds modelled by RegCM4 and then postprocessed with COSP's ISCCP simulator for the same seasons, b) and d). The mean cloud fraction

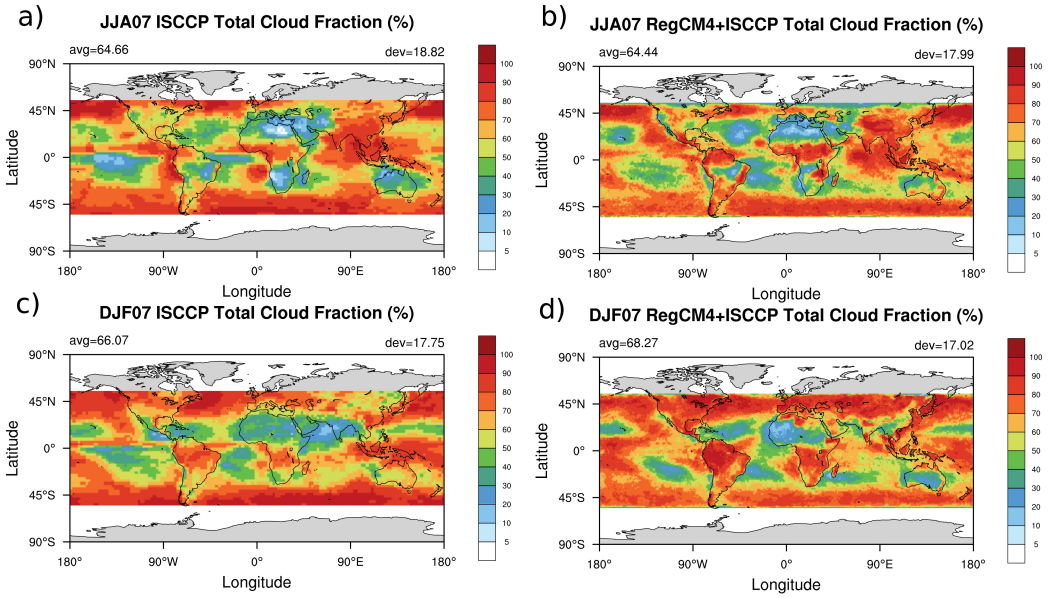

Figure 5.2: Satellite observations of ISCCP total cloud amounts for JJA (a) and DJF (c). RegCM4 simulations using the ISCCP simulator for JJA (b) and DJF (d)

has a good spatial agreement with ISCCP observations for both the seasons: the model mean total cloud fraction for JJA is 64.44 versus the 64.66 observed (+0.3%), and for DJF is 68.27 versus the 66.07 observed (+3%). However, relative to ISCCP the model tends to overestimate clouds preferentially over the land in both JJA and DJF seasons, especially over the North and South America and over South Africa in DJF. The overestimation is balanced by an underestimation of the total cloud cover over Austrialia, over the Southern Indian Ocean and over the Saharan region.

5.3.2 CALIPSO simulator.

The GCM-Oriented CALIPSO Cloud Product, GOCCP data (Chepfer et al., 2010) are used as they are designed for comparisons with output from the CALIPSO satellite simulator. For the seasons DJF and JJA the CALIPSO's observed total cloud fraction is respectively 0.65 and 0.64. The values for RegCM4, simulated with COSP's CALIPSO simulator are respectively 0.69 and 0.73 (+7% in JJA and +10% in DJF). Even if the total amount of clouds is overestimated by the model in both the seasons, the horizontal distribution

of clouds over the the band is well represented. Figures 5.3 a) and c) show the geographical distribution of the total cloud fraction observed for JJA and DJF, while Figures 5.3 b) and d) show the simulated total cloud fraction for the two seasons. Several major features can be clearly identified: both observations and model exhibit maximum cloud cover for JJA and for DJF over the InterTropical Convergence Zone (ITCZ), over the North Atlantic and North Pacific Oceans and over the entire Southern Ocean. Both observations and model exhibit minimum cloud amount in the subtropics of both hemispheres. The model, however, represents the same clouds with a more amplified extension and higher values. There is also a tendency to produce too many clouds throughout the trade wind regions and in the western Pacific warm pool and over the Australia in JJA.

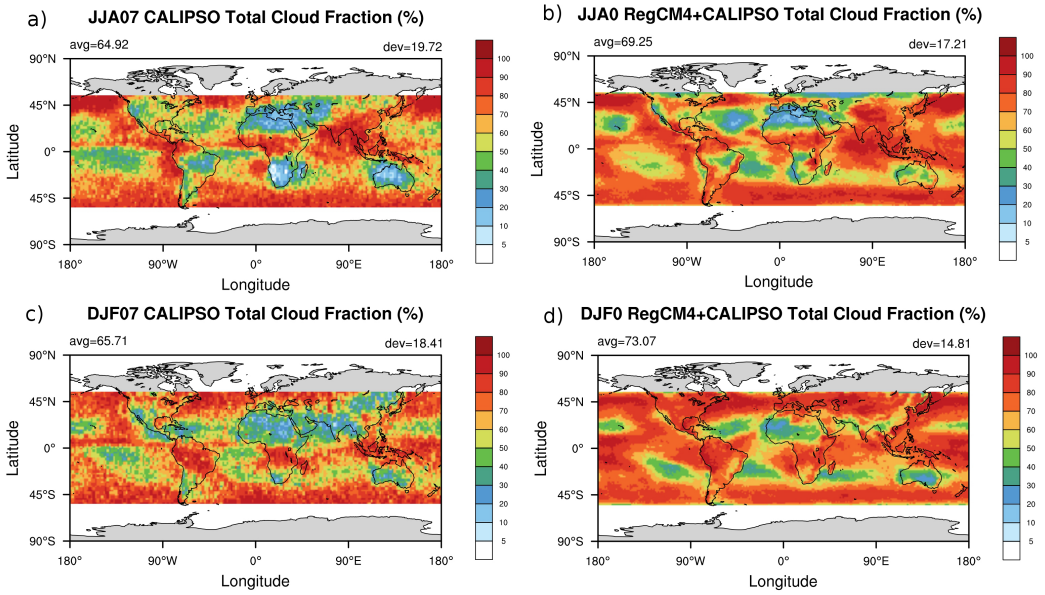

Figure 5.3: Satellite observations of CALIPSO total cloud amounts for JJA (a) and DJF (c). RegCM4 simulations using the CALIPSO simulator for JJA (b) and DJF (d)

In order to investigate more in detail the model cloud representation, three plots with the contributions from the high (50-440 hPa, mainly cirrus and deep cumulus clouds), midlevel (440-680 hPa) and low (>680 hPa, mainly shallow cumulus and stratocumulus) clouds are shown for the season JJA in Figures 5.4 a), c) and e) from the lidar observations and in Figures 5.4 b), d) and f) from the model. High clouds occur near the equator and over tropical continents, and can be seen in the midlatitudes storm track regions. Mid-level

clouds are prominent in the storm tracks and some occur in the Intertropical Convergence Zone. Low clouds, including shallow cumulus and stratiform clouds, are prevalent over cooler subtropical oceans in correspondence of the descending branch of the Hadley Cells. RegCM4 is able to produce low-cloud fractions with very good spatial agreement with the observations. It slightly underestimates them during the JJA, with an average of 31.64 compared to the 35.59 observed (-12%) and shows instead an excellent agreement during the DJF (Figure 5.5), with an average of 35.41 versus the 35.70 observed (-0.8%). The maxima of low clouds in both model and observations occur at the eastern edges of the ocean basins in the subtropical oceanic regions both during JJA and DJF and over the northern Atlantic and Pacific Ocean during the JJA season.

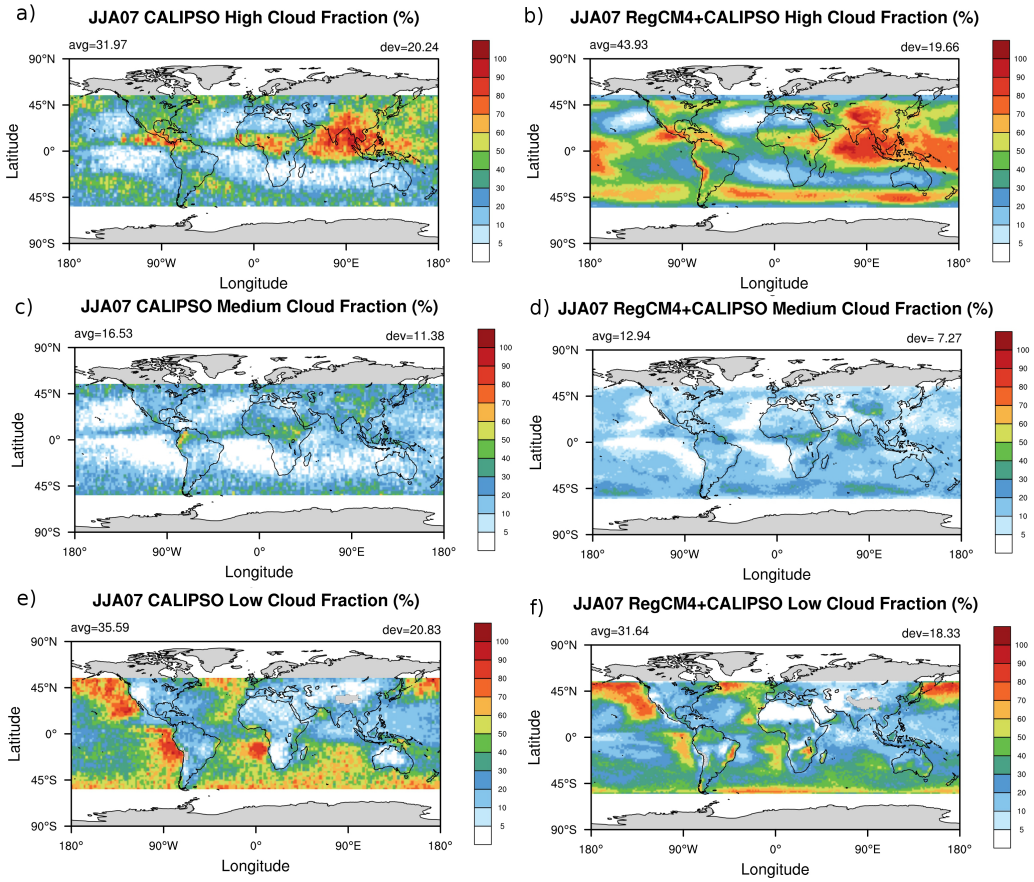

Figure 5.4: (left panels) Satellite observations of CALIPSO cloud amounts for (from top to bottom) high, middle, and low clouds during JJA 2007 (unit in %). Gray represents undefined values. (right) Same as left but for the RegCM4 simulations using the CALIPSO simulator.

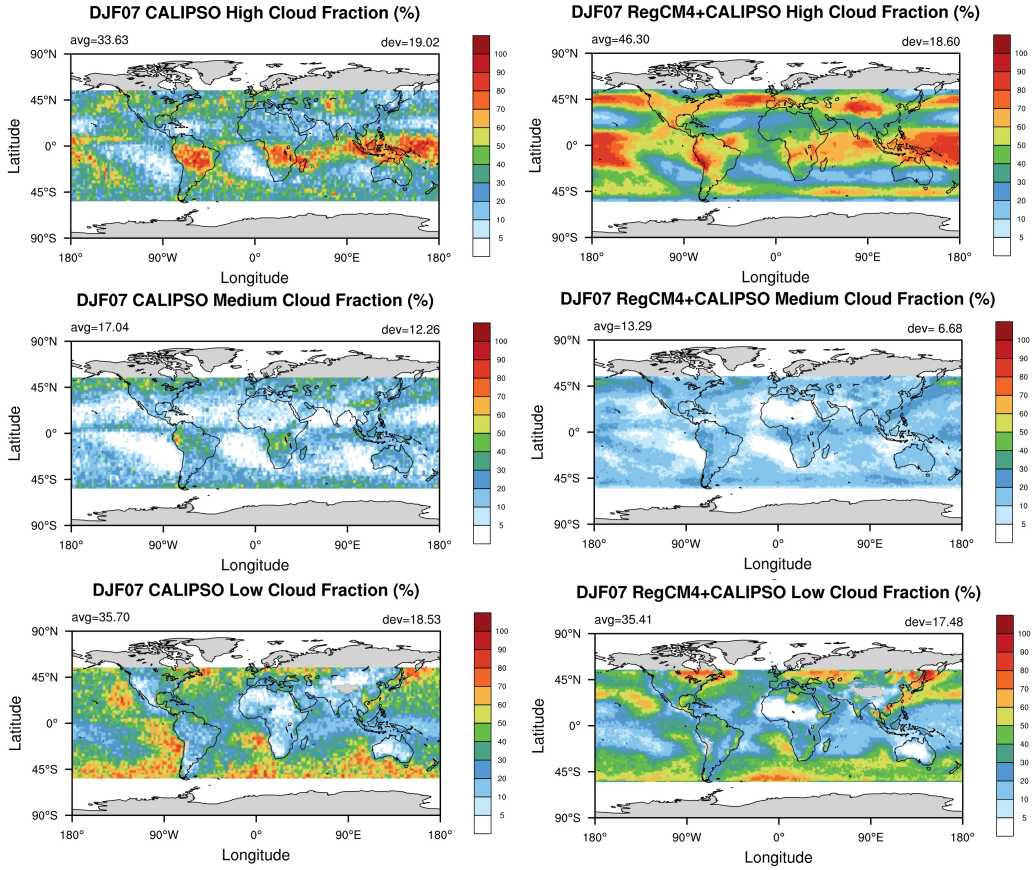

Figure 5.5: Same as 5.4 but for DJF 2007

The model strongly underestimates the medium clouds with an average of 12.94 versus the 16.53 observed during JJA (-30%) and 13.29 versus the 17.04 observed during DJF (-30%).

Another main difference between model and observations concerns the high clouds, both in the amount and in the spatial distribution: although maxima over the Indian region, Central American and Central Africa for JJA and over South America, South Africa and South East Asia for DJF are common for both the model and observations, an excess of high clouds is located over the Southern Ocean. High clouds are overestimated by the model with an average of 43.93 versus 31.97 for JJA and 46.60 versus 33.63 for DJF (+28% for both the seasons).

While the comparison of the total cloud cover with ISCCP was showing an excellent agreement with observations, the comparison with CALIPSO observation gives different results. This difference is helpful in understanding the

reasons of the model biases as it mainly arises from the difference in the sensitivities of the two instruments to the optical depth: while ISCCP is able to detect clouds with an optical depth greater than 0.15 over ocean and 0.25 over land (Rossow and Schiffer, 1999), CALIPSO detects also optically thinner clouds with optical depths greater than 0.03 (Chepfer et al., 2010). Therefore, optically high thin clouds, that are detectable for CALIPSO but not for ISCCP, seem to be overestimated by RegCM4. Other reasons for the overestimation of high clouds might be that the value used for the ice fall speed (0.1 m/s) is too low, letting ice residing in the upper troposphere, or that the relative humidity in the radiative tropopause region is too high. Sensitivity tests need to be done in the future in order to investigate this bias.

5.3.3 ISCCP, MISR and MODIS joint histograms

The climate modelling community uses joint histograms of cloud top pressure (CTP) and optical depth (τ) derived by the ISCCP to validate climate models (e.g. Webb et al., 2001; Zhang et al., 2005; Lin and Zhang, 2004). These histograms have six categories of τ and seven categories of CTP and reproduce the cloud fractions (from 0 to 1) in each of the histogram "bin". The NASA Multiangle Imaging Spectroradiometer (MISR) and Moderate Resolution Imaging Spectroradiometer (MODIS) retrievals can be processed to produce similar joint histograms of cloud top height (CTH) and optical depth. While the ISCCP, MISR histograms and MODIS histograms are conceptually similar, the instruments and the algorithms used are contrasting. Therefore the results can differ quite significantly for observations of the same clouds systems. The comparison between different instruments histograms can allow a more detailed understanding of the observed clouds than any one data set by itself (Marchand et al., 2010). The main difference between the retrievals concerns the response of the algorithms to stratocumulus, trade cumulus and multilayer clouds (Marchand et al., 2010). A key difference also concerns the spatiotemporal sampling of the datasets: while ISCCP uses data produced by geostationary satellites and sun-synchronous satellites that are able to resolve the diurnal cycle, MISR and MODIS fly on sun-synchronous satellites.
Figure 5.6 shows the MISR histograms of optical depth with cloud top height, both observed (a) and simulated (b), for the tropical band in JJA 2007.

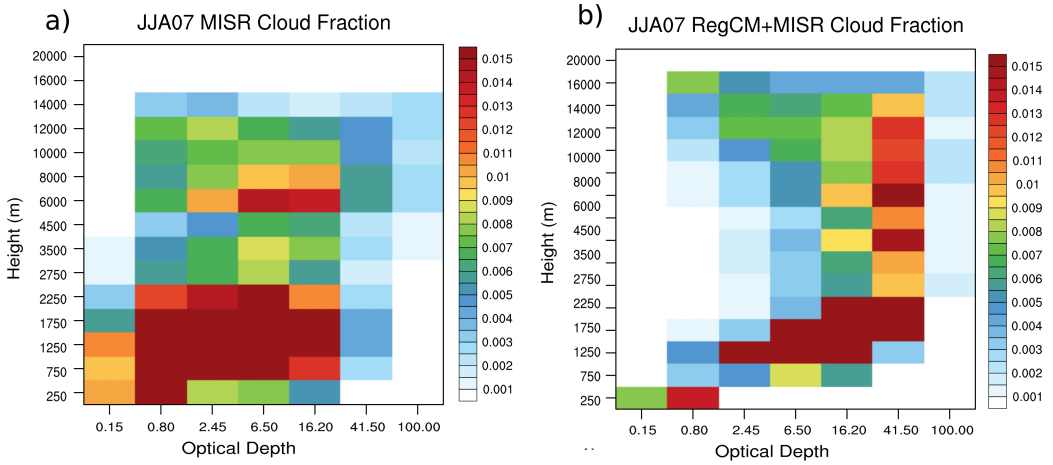

Figure 5.6: a) Joint histograms of cloud top height and optical depth for MISR observations for JJA. b) Joint histograms of cloud top height and optical depth for RegCM4 using MISR simulator for JJA. The color scale represents the cloud fraction in adimensional units, from 0 to 1

Observed MISR reports a bimodal distribution of cloud elevations, with maxima cloud fractions occurring at lower altitudes, between 0.5 and 2.5 km, across a range of optical depths from 0.8 to 16.2 and at higher levels, between 6 and 9 km with optical depths of 2.45-16.2. The MISR simulator compared to observations reports an overestimation of optical depths for both low and medium clouds. Furthermore, the optical depth distribution is narrower than in the observations, with a lack in the representation of optically thin clouds with $0.15<\tau<2.45$.

Figure 5.7 shows the ISCCP histograms of optical depth with cloud top pressure for the tropical band. Observed ISCCP, shown in 5.7 a), reports large fractions of optically thick clouds with cloud-top pressures at the bottom of the troposphere (τ=2.45-6.5 at 740-950 hPa) and of optically thin clouds with cloud-top pressures at the top of the troposphere (τ=0.8 at 90 hPa). It also detects an occurrence of middle-level clouds with top pressures between 350 and 600 hPa.

The ISCCP simulator (Figure 5.7 b), compared to observations, detects the occurrence of low and high clouds at the same cloud-top pressures but it overestimates their optical depths: modelled high clouds cover the entire range of optical depths, from 0.8 to 100, with maximum cloud fractions with $16.2<\tau<41.5$ rather than the 0.8 observed. Low clouds are, instead, underestimated in the occurrence and overestimated in the optical depth: the maxima cloud fractions

occur with optical depth between 6.5 and 41.5, versus the 2.45-16.20 observed. In contrast with MISR simulator, ISCCP simulator does not detect a relevant occurrence of middle level clouds, underestimating them.

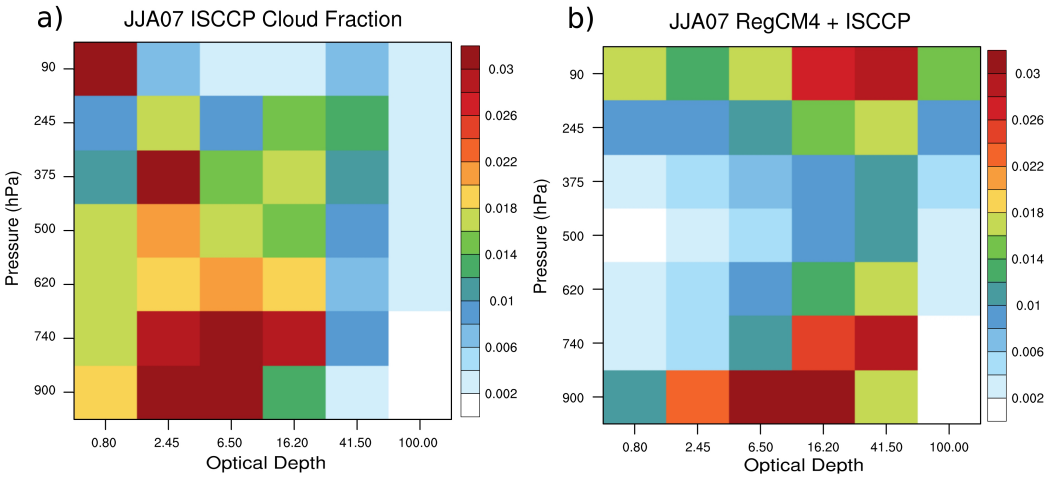

Figure 5.7: a) Joint histograms of cloud top height and optical depth for ISCCP observations for JJA. b) Joint histograms of cloud top height and optical depth for RegCM4 using ISCCP simulator for JJA.

Figure 5.8 shows the MODIS histograms of optical depth with cloud top pressure for the tropical band. Observed MODIS, Figure 5.8 a), reports a bimodal distribution of cloud elevations, with maxima observed cloud fractions at high cloud-top pressures, between 700 and 950 hPa, across a range of optical depths from 2.45 to 16.2 and at cloud-top pressures between 200 and 370 hPa with optical depths between 2.45 and 41.5. MODIS simulator, Figure 5.8 b), is able to detect the bimodal distribution, producing the maxima of cloud fractions between 700 and 950 hPa, and above 245 hPa underestimating occurrences and optical depths of high clouds. A possible reason for this underestimation of high clouds resides in the fact that MODIS simulator algorithm, unlike MISR and ISCCP, uses the effective radii of liquid and of ice particles to retrieve the cloud fraction. RegCM4, in the radiation scheme, uses a fixed effective radius for liquid water particles set to 10μm over the ocean. Over the land the liquid effective radius $r_{l,eff}$ is calculated as a function of temperature as follows:

$$r_{l,eff} = 5 + 5 * (T_i - T) * 0.05 \tag{5.2}$$

where $T_i = 263.16$ is the threshold temperature below which liquid is converted into ice in the radiation scheme. The ice effective radius is calculated

as a function of the normalised pressure, assuming a range of values between 10 and 30μm.

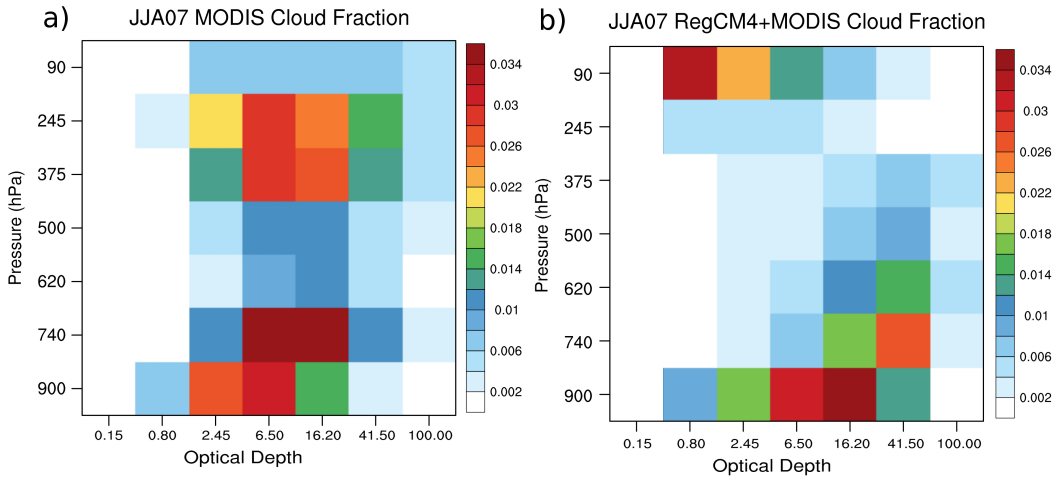

Figure 5.8: a) Joint histograms of cloud top height and optical depth for MODIS observations for JJA. b) Joint histograms of cloud top height and optical depth for RegCM4 using MODIS simulator for JJA.

To test the sensitivity of high clouds to the ice effective radius a sensitivity test has been performed doubling the ice size in the MODIS simulator for the tropical band. Figure 5.9 shows the MODIS histograms of optical depth with cloud top pressure obtained with the modified ice effective radius and it is clear that with this change the amount of high clouds has improved, even if still underestimating the observed amount.

The underestimation of high clouds by the MODIS simulator suggests the need to review the way the effective radii are calculated in the model, and to consider the implementation of a new algorithm that improves the representation of the ice particle size distribution (e.g. Franklin et al., 2013; Wilson and Ballard, 1999).

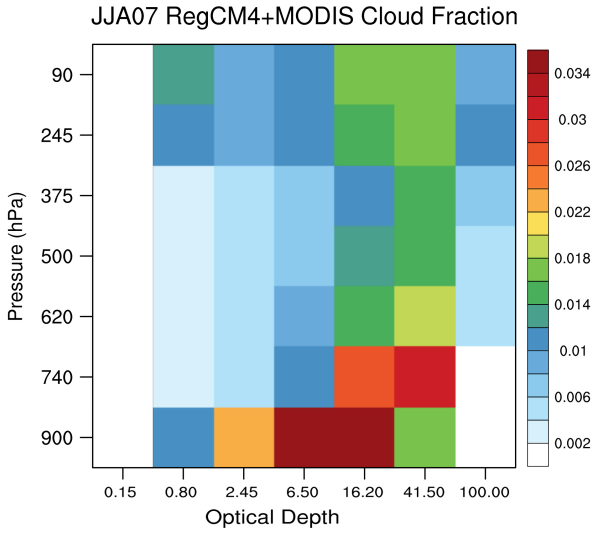

Figure 5.9: Same as 5.8(b) but doubling the ice size within the MODIS simulator.

5.4 Regional Evaluation of RegCM4 Clouds

In order to analyse the modelled cloud properties in more detail, joint histograms from MISR and MODIS are compared with observations in two regions with two different typical cloud types: the SouthAmerican stratocumulus region, where clouds are formed by subtropical subsidence and the Tropical Warm Pool, where clouds are produced by deep convection. The choice of MISR and MODIS simulators for this analyses is tied to the fact that while MODIS is better in seeing high cirrus clouds but can have issues in detecting what is below if their optical depths are too high, MISR is better in penetrating clouds, resolving what is underneath Naud et al. (2002). The combination of the two simulators therefore guarantees an almost complete characterisation of the vertical cloud structure.

5.4.1 SouthAmerican Stratocumulus (25°S-10°N,70°E-115°E)

As already introduced, stratocumulus clouds are important because of their large cloud fractions (Klein and Hartmann, 1993), and because of their impact on the atmospheric radiation budget. According to Bony and Dufresne (2005) they are the main responsible for the model differences in representing the cloud feedbacks. It is therefore important to understand how the model is able to simulate the structure of persistent stratocumulus clouds. For this

region only the JJA season is analysed as the SouthAmerican stratocumulus cloud fractions are larger during JJA rather than during DJF and also because in JJA there are less occurrences of cirrus clouds that might obscure the satellite observations of low clouds. Figure 5.10 shows cloud fractions observed by MISR (a) and RegCM4 cloud fractions postprocessed by MISR simulator (b).

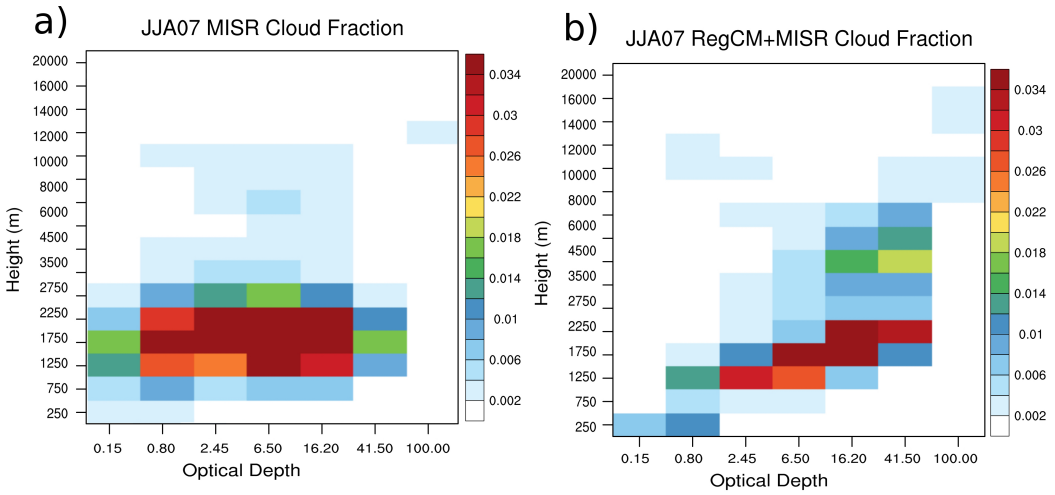

Figure 5.10: Observed clouds by MISR (a) and modelled clouds as reproduced by MISR simulator (b) for JJA 2007 in the SouthAmerican stratocumulus region (25°S-10°N,70°E-115°E).

The MISR observations in the SouthAmerican stratocumulus region in JJA show a low-level stratocumulus cloud between 500 m and 2.5 km with optical depths between 0.8 and 16.2. The model has a narrower layer of clouds, ranging from 500 m to 2 km with higher optical depths assuming values between 2.45 and 41.5.

The MODIS comparison, Figure 5.11 a) and b), shows optically thicker clouds simulated by RegCM4 in the low levels. The stratocumulus cloud occurring with higher cloud fractions in the observations occur with cloud tops of 600 hPa and optical depths between 2.45 and 16.20. In the model the low level cloud top heights reach higher levels, 450 hPa, but the maxima of cloud fraction occur at 100 hPa.

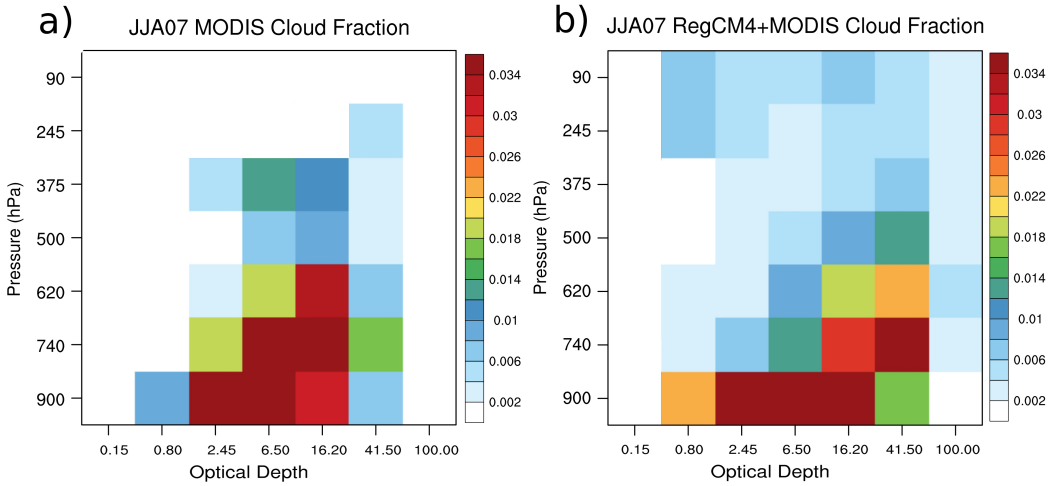

Figure 5.11: Observed clouds by MODIS (a) and modelled clouds as reproduced by MODIS simulator (b) for JJA 2007 in the SouthAmerican stratocumulus region (25°S-10°N,70°E-115°E).

5.4.2 Western Pacific Warm Pool (15°S, 15°N, 120°E-170°E)

The Western Pacific Warm Pool is a region characterised by deep convection activity, that is forced by a wide range of spatial and temporal scales (from localised thunderstorms to the Madden-Julian oscillation) and represents a critical source of heat and moisture for the tropical climate system. Given the importance of this region to the global climate (Neale and Slingo, 2003) it is important to understand how the model is able to represent the complex clouds structures observed in this region.

Figure 5.12 shows the JJA modelled clouds as observed by MISR (a) and as reproduced by MISR simulator (b). The MISR histograms of observed cloud top height and optical depth show a bimodal distribution of clouds, with larger cloud fractions between 0 and 2 km, and less occurrence of high clouds in the layer between 4 and 13 km. The model confirms the trend for the whole band, shown in 5.6, as it is able to reproduce the same vertical distribution overestimating the optical depth of both the low and the high clouds.

Figure 5.13 shows the same clouds as observed by MODIS (a) and as reproduced by MODIS simulator (b). MODIS confirms what found for the entire tropical band shown in 5.8, as it still underestimates the occurrence of deep convective high clouds. There is however a discrepancy for the low-level clouds with cloud tops below 800 hPa as at this level the occurrence of clouds with

optical depth of 2.45 is overestimated by the model.

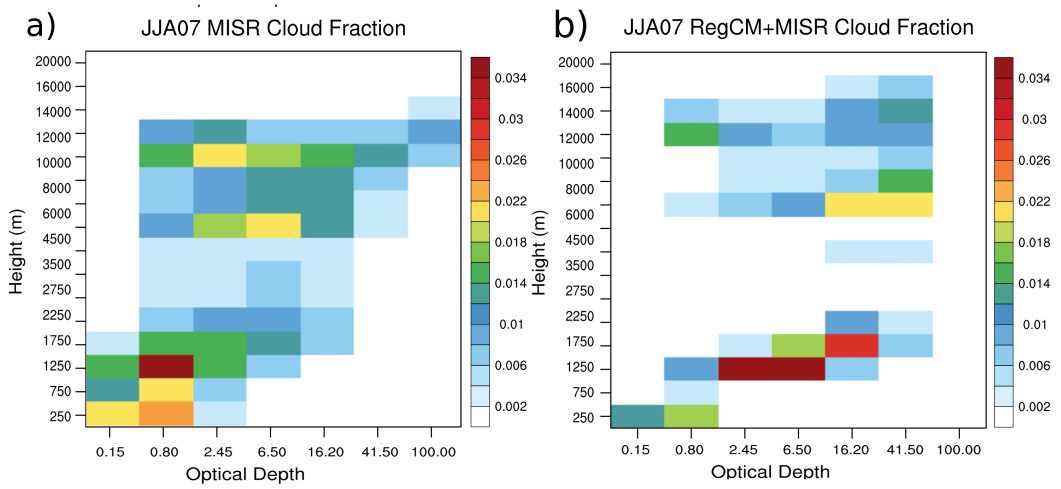

Figure 5.12: Observed clouds by MISR (a) and modelled clouds as reproduced by MISR simulator (b) for JJA 2007 for JJA 2007 in the Western Pacific Warm Pool region (15°S, 15°N, 120°E-170°E).

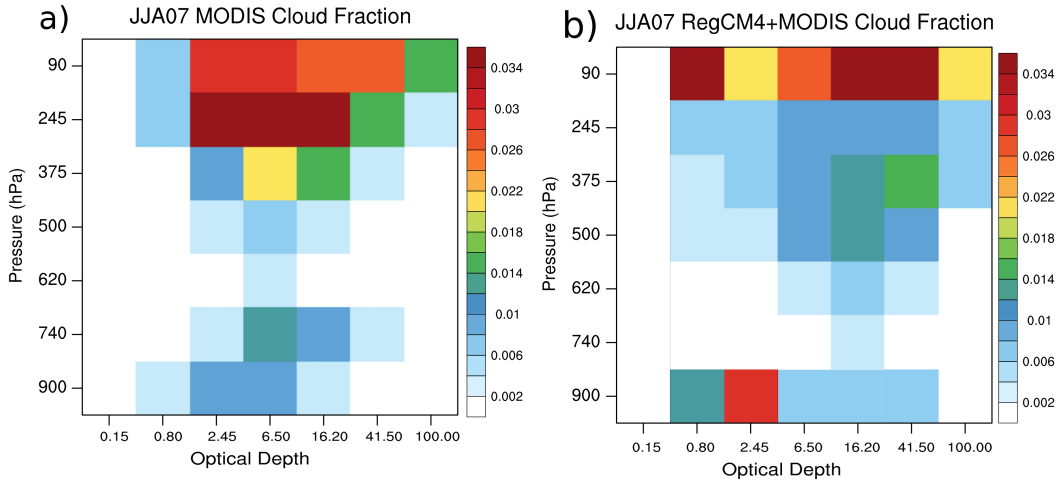

Figure 5.13: Observed clouds by MODIS (a) and modelled clouds as reproduced by MODIS simulator (b) for JJA 2007 in the Western Pacific Warm Pool region (15°S, 15°N, 120°E-170°E).

5.4.3 Discussion of the results

For both ISCCP, MISR and MODIS simulators histograms referring to the whole band it is possible to summarise the following biases for RegCM4:

(i) overestimation of high optically thick clouds,

(ii) overestimation of low and middle optically thick clouds, and

(iii) underestimation of optically thin low and middle clouds.

Zhang et al. (2005), to assess the current status of climate models in simulating clouds, compared the cloud climatologies from ten atmospheric general circulation models (two versions of the UKMO GCM, three of the NCAR CAM, ECHAM5, GFDL, GISS, GSFC and LMD) with satellite measurements from the International Satellite Cloud Climatology Project (ISCCP) showing that overestimation of thick clouds is common to the considered models and it does not depend on the used microphysics cloud scheme. They also showed that most of the considered models underestimate optically intermediate and thin clouds. Webb et al. (2001) showed that there is a general tendency in models for higher cloud top to have larger optical depths, an indication of larger liquid and ice water paths associated with deeper clouds. RegCM4 produces overestimated optically thick middle clouds both in the analysed convective region and in the stratocumulus region. A further analysis needs to be done to understand these biases, using different convection schemes and higher vertical and horizontal resolutions. Williams et al. (2003), to find an explanation for common model's biases in the overestimation of optically thick clouds, showed that tropical optically thick clouds are associated with strong vertical motions due to large-scale convective systems. They therefore highlighted that global and regional's cloud schemes do represent partial cloud coverage but do not account for the subgrid distribution of temperature and moisture tendencies due to the subgrid circulations. A reason for the overestimation of thick clouds may reside in the fact that even if only part of the grid box is subjected to a strong upward motion, the mean vertical velocity for the grid box is upward, leading to an updraft of the entire gridbox. A reason for the overestimation of low optically thick clouds can be related to the poor horizontal resolution (100 km) that is not able to resolve surface-heterogeneity and topography shallow mesoscale and further analyses need to be done in order to investigate this aspect.

While, according to Zhang et al. (2005), models generally experience a lack in the representation of stratocumulus clouds, the use of the recent boundary layer scheme of Bretherton et al. (2004) allows RegCM4 to represent the low clouds. The model, however tends to overestimate their optical depths and the overestimation concerns both the stratocumulus and shallow convective

clouds. This might be associated with very weak vertical motions at low levels as found by Lin and Zhang (2004), suggesting the need of future investigations on the vertical velocity simulated by the model.

Underestimation of optically thin low and middle clouds can be associated to a lack of the convection scheme in simulating shallow convections, or to a lack of moisture in low and middle troposphere for which small droplets tend to evaporate once formed, and needs to be further investigated.

Conclusions

This thesis presents the new microphysical parameterization cloud scheme implemented in the Regional Climate Model RegCM4 and the key aspects of the improvements the new scheme brings to the model. The general aim of the study has been to present an overview of the new features of the scheme and of the investigations that need to be done in the close future to address the new revealed RegCM4 biases in the ability of reproducing clouds.
A brief history of cloud parameterization in climate models and the importance of improving cloud representation has been introduced in Chapter 1. Chapter 2 gives an overview of the microphysical processes involved in both the warm and cold clouds and Chapter 3 presents the new microphysics cloud scheme and the way the microphysical processes are treated within its numerical framework. Chapter 4 contains a first discussion of the results by means of an evaluation of the vertical distributions of the main microphysical quantities, such as the liquid and ice water mixing ratios and the relative fractions, and through a quantitative evaluation of the effects of having a precipitation subjected to the wind advection. It also presents a series of sensitivity tests to understand how the moisture and radiation quantities respond to the variation of the microphysical parameters used in the scheme, such as the fall speeds of the falling categories, the autoconversion scheme and the evaporation coefficient. Finally, Chapter 5 presents the implementation for RegCM4 of the new cloud evaluation COSP tool, developed by the Cloud Feedback Model Intercomparison Project (CFMIP), that facilitates the comparison of simulated clouds with observations from passive and active remote sensing by diagnosing from model outputs the quantities that would be observed from satellites if they were flying above an atmosphere similar to that predicted by the model.

As outlined at the end of Chapter 1, the large-scale cloud and precipitation scheme previously implemented in RegCM4, described in Pal et al. (2000), includes a simple representation for the formation of rain drops and solves diagnostically the precipitation, not accounting for the cold clouds microphysics. The new cloud microphysics scheme, built upon the European Centre for Medium Weather Forecast's Integrated Forecast System (IFS) (Tiedtke, 1993; Tompkins, 2007; Forbes et al., 2011), solves implicitly 5 prognostic equations for the water vapour, the liquid water, the rain, the ice and the snow mixing ratios. Treating separately liquid and ice phases it allows the co-existence of supercooled liquid water and of ice crystals. The first section of Chapter 4 shows that the new scheme, with its separate treatment of liquid water and ice, allows the representation of the mixed-phase clouds, clouds located in the range of temperature between 0°C and -38°C, where the water droplets remain in a supercooled liquid phase and coexist with ice crystals. The third section of Chapter 4 presents the results of a set of numerical experiments aiming to test the sensitivity of moisture and radiation variables to the change of the coefficients used in the autoconversion, evaporation and sedimentation parameterizations. The parameter to which both the columnar water contents and the cloud radiative forcing seem to be more sensitive is the value of the ice fall speed. Increasing the fall speed of ice the total columnar ice and water contents decrease in the medium and upper levels (from 100 to 700 hPa) but the columnar water content increases in the low levels entailing a decrease of the cloud radiative forcing. The ice and the snow fall speeds play a decisive role in the amount of large scale precipitation, while sensitivity to the rain fall speed and to evaporation rate are not evident as the rain fall speeds are so fast that the majority of rain falls out the column within the timestep. This would not be the case for higher resolution simulations and a further analyses needs to be done in view of the forthcoming increasing resolution due to the inclusion of a non-hydrostatic core for RegCM4. Another parameter to which the precipitation is sensitive is the threshold coefficient for the autoconversion, that represents the threshold at which cloud droplets are converted to rain. Precipitation is relatively insensitive to evaporation rate.

Chapter 5 contains the description of the Cloud Feedback Model Intercomparison Project (CFMIP) observational Package COSP implemented for RegCM4 and the preliminary results of an evaluation of modelled clouds for a one-year

simulation. ISCCP, CALIPSO, MODIS and MISR simulators have been used to quantify the ability of the model in producing the horizontal and vertical distributions of clouds over the tropical band, and to identify biases in the representation of their optical depths. The analysis starts with the comparison of the horizontal distribution of clouds for both JJA 2007 and DJF 2007 seasons with ISCCP dataset, that represent the first dataset built with the aim of inferring the global distribution of cloud radiative properties in order to improve the modelling of clouds effects on climate. The comparison of the total cloud cover with ISCCP gives impressive results, with overestimations of 0.3% and 3% of the model for JJA and DJF respectively. The comparison with the CALIPSO total cloud cover gives, on the other hand, different results, as the model shows important overestimations of the 30% for the high clouds (50-440 hPa) and a related underestimation of the middle clouds (440-680 hPa). The difference of the results between ISCCP and CALIPSO suggests that the model tends to overestimate optically thin clouds, that are not detected by ISCCP. In fact ISCCP is able to detect clouds with optical depths greater than 0.15-0.25 (over ocean and land), while CALIPSO detects optically thinner clouds with optical depths greater than 0.03.

A further analysis is presented using the joint histograms of cloud top pressures and heights and optical depths derived by ISCCP, MODIS and MISR simulators. The analysis is driven over the whole band and over two regions experiencing two different typical cloud types: the Southamerican stratocumulus region, and the Tropical Warm Pool where clouds are produced by deep convection. Also for this analysis a combination of different simulators guarantees a more complete characterisation of the vertical cloud structure and of the model biases.

Looking at both ISCCP, MISR and MODIS simulators histograms it is possible to identify the following biases for RegCM4:

(i) overestimation of high optically thick clouds,

(ii) overestimation of low and middle optically thick clouds, and

(iii) underestimation of optically thin low and middle clouds.

RegCM4 is in line with what found by Zhang et al. (2005) trying to assess the status of climate models in simulating clouds. Zhang et al. (2005) compared the cloud climatologies from ten atmospheric general circulation models (two versions of the UKMO GCM, three of the NCAR CAM, ECHAM5, GFDL,

GISS, GSFC and LMD) with satellite measurements from the International Satellite Cloud Climatology Project (ISCCP) and showed that overestimation of thick clouds is common to the general circulation models considered in his study and it does not depend on the used microphysics cloud scheme, but it is still left as an open question. He also showed that most of the considered models underestimate optically intermediate and thin clouds.
Webb et al. (2001) found that there is a general tendency in models for higher cloud top to have larger optical thicknesses, an indication of larger liquid and ice water paths associated with deeper clouds. RegCM4 produces overestimated optically thick middle clouds not only in the analysed convective region but also in the stratocumulus region. A further analysis therefore still needs to be done to understand these biases, using different convection schemes and higher vertical and horizontal resolutions.
The comparison with MODIS data suggests that an improvement is necessary in the calculation of the effective radii of ice and cloud droplets, for example by considering the implementation of a new algorithm that enhances the representation of the ice particle size distribution separating the ice water variable into a large ice category (aggregates) and a small ice category (crystals) by a diagnostic function of temperature (e.g. Franklin et al., 2013; Wilson and Ballard, 1999). Another possible, but more computationally expensive, solution to improve the cloud properties would be the choice of moving to a two-moment microphysics scheme with the inclusion of new prognostic equations governing the number concentration of the hydrometeor categories. Two-moment schemes have been widely used in cloud-resolving and mesoscale models (e.g. Khairoutdinov and Kogan, 2000; Milbrandt and Yau, 2005; Seifert and Beheng, 2001) and simplified two-moment schemes have been developed for GCMs (e.g. Ghan et al., 1997; Lohmann et al., 1999). The two-moment method is known to produce significant improvements in the treatment of the sedimentation of particles (e.g. Milbrandt and Yau, 2005) and the prognostic number concentration N should lead not only to a more realistic representation of the effective radius but also to an improved treatment of the optical properties of the modelled clouds and to a more robust interaction between clouds and aerosols (Morrison and Gettelman, 2008). However this solution introduces the potential of inconsistencies because of the separate treatment of the predicted number concentrations and of the mixing ratios, resulting in the diagnosis of extreme

hydrometer diameters and unrealistic mean clouds and mean particle size distribution. For consistency, N is adjusted to ensure that the particles diameters remain within a specified range of values for each species, re-diagnosing the concentration if the diameters are out of bounds (e.g. Morrison and Gettelman, 2008; Meyers et al., 1997).

In addition to the described advantages given by a more physical representation of the cloud microphysics, the new scheme constitutes a major tool to support new research on cloud representation and on the climatological fields.

Appendix A

The Regional Climate Model RegCM

A.1 Introduction to the model

Limited area models (LAMs) are widely used in numerical weather and regional climate predictions, and allow the use of a higher spatial resolution. To aim this goal LAMs require lateral boundary conditions that are normally provided by Global Circular Models (GCMs). RegCM4 is the evolution of the first version, developed in 1980s (RegCM1; Dickinson et al. 1989, Giorgi 1990) of the first limited area model developed for long-term regional climate simulations.
RegCM4 is an hydrostatic, compressible, sigma-p vertical coordinate model run on an Arakawa B-grid (Figure A.2) in which wind and thermodynamical variables are horizontally staggered. As for the MM5 (Grell et al., 1994), a time-splitting explicit integration scheme is used, for which the fastest gravity modes are first separated from the model solutions and then integrated with smaller time steps, allowing the use of a longer time step for the rest of the model. Following, only a framework of the model physics will be presented, while a more detailed description of RegCM4 is provided in Giorgi et al. (2012).
The vertical coordinate is terrain-following (Figure A.1) : levels are more dense at the bottom of the atmosphere, allowing a more detailed treatment of the small scale processes occurring close to the surface, and progressively flatten as the pressure decreases towards the top of the model.
A dimensionless vertical coordinate σ is defined in terms of pressure:

$$\sigma = \frac{p - p_t}{p_s - p_t} \tag{A.1}$$

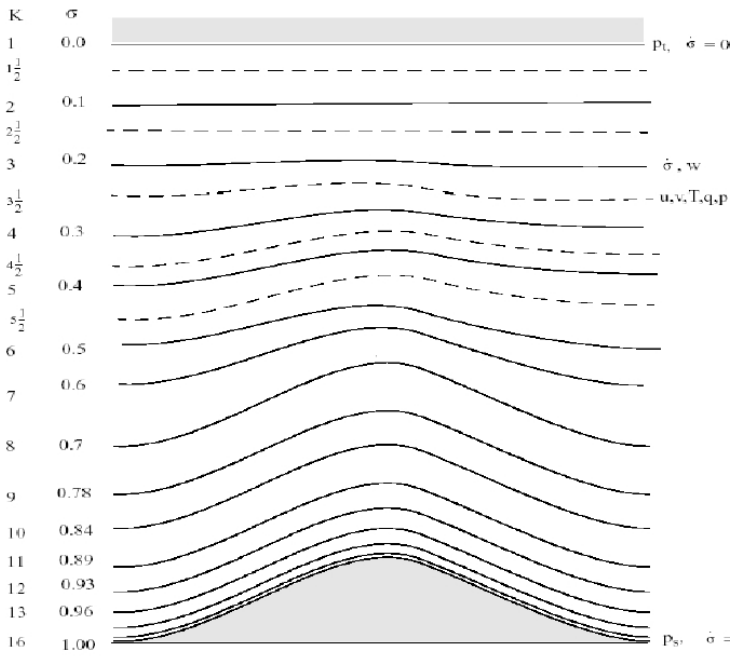

Figure A.1: Schematic representation of the vertical structure of the model, for 16 vertical layers. Dashed lines denote half-sigma levels, solid lines denote full-sigma levels.

where p_s is the surface pressure and p_t is a fixed pressure chosen for the top of the troposphere (usually equal to 0 or $5mb$).
The horizontal grid (Figure A.2) has an Arakawa B-staggering of the velocity variables (u and v)

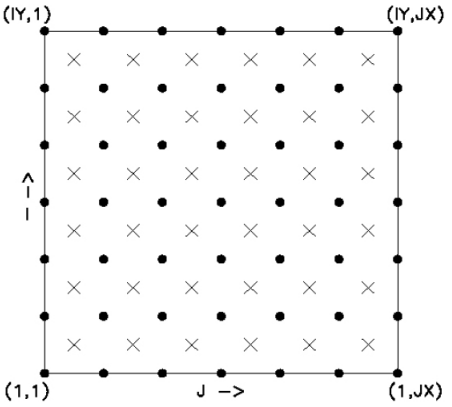

Figure A.2: Schematic representation showing the horizontal Arakawa B-grid staggering of the dot and cross grid points.

with respect to the scalar variables (T, q, p, etc) that are defined at the centre of the gridbox, while the wind components are calculated at the corners.
All the above variables are defined in the middle of each vertical layer, referred to as half-levels.

A.2 Model Physics

A list of the model equations follows, their numerical discretisation is described by Grell et al. (1994).

A.2.1 Horizontal Momentum Equations

$$\frac{\partial p^* u}{\partial t} = -m^2\Big(\frac{\partial p^* uu/m}{\partial x} + \frac{\partial p^* vu/m}{\partial y}\Big) - \frac{\partial p^* u\dot{\sigma}}{\partial \sigma} - mp^*\left[\frac{RT_v}{(p^* + p_t/\sigma)}\frac{\partial p^*}{\partial x} + \frac{\partial \phi}{\partial x}\right] + fp^* v + F_H u + F_V u, \tag{A.2}$$

$$\frac{\partial p^* v}{\partial t} = -m^2\Big(\frac{\partial p^* uv/m}{\partial x} + \frac{\partial p^* vv/m}{\partial y}\Big) - \frac{\partial p^* v\dot{\sigma}}{\partial \sigma} - mp^*\left[\frac{RT_v}{(p^* + p_t/\sigma)}\frac{\partial p^*}{\partial y} + \frac{\partial \phi}{\partial y}\right] + fp^* u + F_H v + F_V v, \tag{A.3}$$

where u and v are the eastward and northward component of the horizontal wind, $T_v = T(1 + 0.608q_v)$ is the virtual temperature, ϕ is the geopotential height, f is the Coriolis parameter, R is the gas constant for dry air, m is the map scale factor for either the Polar Stereographic, Lambert Conformal, or Mercator map projections and F_H and F_V represent the effects of horizontal and vertical diffusion and $p^* = p_s - p_t$.

A.2.2 Continuity and Sigmadot Equations

$$\frac{\partial p^*}{\partial t} = -m^2\Big(\frac{\partial p^* u/m}{\partial x} + \frac{\partial p^* v/m}{\partial y}\Big) - \frac{\partial p^* \dot{\sigma}}{\partial \sigma} \tag{A.4}$$

The vertical integration of (A.4) is used to compute the tendency of the surface-pressure $\frac{\partial p^*}{\partial t}$ and the vertical velocity sigma coordinates $\dot{\sigma}$ at each level:

$$\dot{\sigma} = -\frac{1}{p^*}\int_0^\sigma \left[\frac{\partial p^*}{\partial t} + m^2\Big(\frac{\partial p^* u/m}{\partial x} + \frac{\partial p^* v/m}{\partial y}\Big)d\sigma', \tag{A.5}$$

A.2.3 Thermodynamic Equation and Equation for ω

The thermodynamic equation is

$$\frac{\partial p^* T}{\partial t} = -m^2\Big(\frac{\partial p^* uT/m}{\partial x} + \frac{\partial p^* vT/m}{\partial y}\Big) - \frac{\partial p^* T\dot{\sigma}}{\partial \sigma} + \frac{RT_v\omega}{c_{pm}(\sigma + P_t/p_{ast})} + \frac{p^* Q}{c_{pm}} + F_H T + F_V T, \tag{A.6}$$

where c_{pm} is the specific heat for moist air at constant pressure, Q is the diabatic heating and F_H and F_V represent the effects of vertical mixing and dry convective adjustment.
ω is given by:

$$\omega = p^*\dot{\sigma} + \sigma\frac{dp^*}{dt} \tag{A.7}$$

A.2.4 Hydrostatic Equation

In order to compute the geopotential heights, the hydrostatic equation is used:

$$\frac{\partial \phi}{\partial \ln(\sigma + p_t/p^*)} = -RT_v\left[1 + \frac{q_c + q_r}{1 + q_v}\right]^{-1}, \tag{A.8}$$

where q_v, q_c and q_r are the water vapour, cloud water or ice, and rain water or snow mixing ratios.

A.3 Physics Parameterizations

A.3.1 Radiative transfer

The radiation scheme is described in Kiehl et al. (1996). The solar component, which accounts for the effect of O_3, H_2O, CO_2, and O_2, includes 18 spectral intervals from 0.2 to 5 μm.
According to the parameterization described in Slingo (1989) the optical properties of the cloud droplets (the extinction optical depth, the single scattering albedo, etc.) are expressed in terms of the cloud liquid water content and of the droplet radius. The thickness of the cloud layer is assumed to be equal to that of the model layer, and a different cloud water content is specified for middle and low clouds.

A.3.2 Land Surface Models

- BATS. The Biosphere-Atmosphere Transfer Scheme (Dickinson et al., 1993a) is used to describe the role of vegetation and of soil moisture in modifying the surface-atmosphere exchanges of momentum, energy and water vapour. The model considers 3 soil layers (a snow layer, a surface soil layer 10 cm thick, and a deep soil layer 3 m thick) and a vegetation layer, accounting for 7 prognostic variables: canopy temperature surface, soil temperature subsurface, soil temperature, surface soil water, root-zone soil water , total soil water and canopy water store.
  Snow depth is prognostically calculated from snowfall, snowmelt, and sublimation. Precipitation is assumed to fall in the form of snow if the temperature of the lowest model level is below 271 K.
  The Biosphere-Atmosphere Transfer Scheme (BATS) has 20 vegetation types that are described in Dickinson et al. (1986).
- CLM. The Community Land Model CLM (Oleson, 2008) contains 5 possible snow layers with an additional representation of trace snow and 10 unevenly spaced soil layers with explicit solutions of temperature, liquid water and ice water in each layer.
  CLM uses a tile approach to capture surface heterogeneity: each CLM gridcell contains up to 4 different land cover types (glacier, wetland, lake, and vegetated), where the vegetated fraction can be further divided into 17 different plant functional types. Hydrological and energy balance equations are solved for each land cover type and aggregated back to the gridcell level.

A.3.3 Planetary boundary layer.

In the atmospheric boundary layer motions result from the interaction of three distinct factors that act over three different scales:

- the synoptic scale forcing and the thermal stratification in the lower troposphere;
- the semi-organised structures having a length scale of the same order of the boundary layer height, conventionally indicated as large eddies;
- the small scale turbulence.

Since atmospheric motions are characterised by a high Reynolds number ($\approx$ 10^6-10^7) the third factor is constantly active. When the first is weak respect to the second, a regime of free convection develops and the transport is governed essentially by turbulent advection (through the large eddies) and turbulent diffusion (through the small-scale turbulence). Non local vertical fluxes then develop and depend on the dynamic of the entire motion field and not on the singular local values. The planetary boundary layer scheme is fully described in Holtslag et al. (1990).

A.3.4 Cumulus convection.

Since the model resolves only scales that are larger than the cumulus scale, a parameterization is needed to represent the contribution of cumulus clouds on the temperature and moisture fields of the atmosphere.
Convective precipitation is computed using one of the four following schemes:

- Modified-Kuo scheme (Anthes, 1977);
- Grell scheme (Grell, 1993);
- MIT-Emanuel scheme (Emanuel, 1991; Emanuel and Zivkovic-Rothman, 1999);
- Tiedtke (Tiedtke, 1989).

The **Kuo Scheme** initiates the convective activity when the moisture convergence M exceeds a threshold and the column is thus convectively unstable.
A fraction of the moisture convergence is converted into rainfall P_{cu} while the rest, β, does not condensate:

$$P_{cu} = M(1 - \beta) \tag{A.9}$$

where β is a function of the column average RH. The latent heating associated with the condensation is distributed between the cloud top and bottom by a function that assigns the maximum heating to the upper portion of the cloud layer.
The **Grell scheme** considers convective clouds as made of two steady-state circulations: an updraft and a downdraft, with no mixing with the environment occurring along the column but only at the top and at the bottom.

The circulations are simulated to take place where there is a maximum (updraft) and a minimum (downdraft) of moist static energy.
The downdraft mass flux (m_0) depends on the updraft mass flux (m_b) according to the following relation:

$$m_0 = \frac{\beta I_1}{I_2} m_b \tag{A.10}$$

where I_1 and I_2 are the normalised updraft condensation and downdraft evaporation and β is the fraction of updraft condensation that re-evaporates in the downdraft.
Rainfall is given by

$$P^{CU} = I_1 m_b (1 - \beta) \tag{A.11}$$

Heating and moistening in the Grell scheme are determined both by the mass fluxes and the detrainment at the cloud top and bottom.
The **MIT-Emanuel scheme** considers the effect of mixing but assumes it is highly episodic and inhomogeneous.
Convection activates when the level of neutral buoyancy is higher than the cloud base level. Within the two levels air is lifted and condenses forming precipitation. Air is allowed to mix with the air from the environment and the mixing entrainment and detrainment rates are functions of the vertical gradients of buoyancy in clouds.
Respect to the other schemes the MIT-Emanuel scheme offers a more physical representation of convection as it includes a formulation of the autoconversion of cloud water into precipitation inside cumulus clouds. The precipitation is added to a single hydrostatic unsaturated downdraft that transports heat and water.
The **Tiedtke scheme** considers both cumulus scale updraft and downdraft and is applied separately to the two processes, with different bulk properties for different types of convection (i.e. penetrative, shallow and midlevel convections).
The updraft is assumed to be in a steady state. Freezing and melting processes are not considered and the cloud water conversion into rain droplets is proportional to the cloud water amount. It is assumed that the liquid water detrained into the environment evaporates instantaneously once outside the cloud. The entrainment of mass into convective plumes occurs through turbulence at cloud edges and through large-scale convergence.

The turbulent entrainment/detrainment has a fixed value for each type of convection:

$$\epsilon = \delta = \begin{cases} 1 \cdot 10^{-4}, & \text{for penetrative and midlevel convection} \\ 3 \cdot 10^{-4}, & \text{for shallow convection in suppressed conditions} \end{cases} \tag{A.12}$$

Cumulus downdrafts are considered to be associated with the precipitation caused by the condensation in the updraft and their mass flux is proportional to the upward fluss max.

Appendix B

Nomenclature

Acronyms

CALIPSO	Cloud-Aerosol Lidar and Infrared Pathfinder Satellite Observations
CCN	Cloud Condensation Nuclei
CERES	Clouds and the Earth's Radiant Energy System
CFMIP	Cloud Feedback Model Intercomparison Project
COSP	CFMIP Observation Simulator Package
CRF	Cloud Radiative Forcing
ECMWF	European Centre for Medium Range Weather Forecasts
ERA	ECMWF Re-Analysis
ERBE	Earth Radiation Budget Experiment
IFS	Integrated Forecast System
ISCCP	International Satellite Cloud Climatology Project
ITCZ	InterTropical Convergence Zone
MISR	Multiangle Imaging Spectroradiometer
MODIS	Moderate Resolution Imaging Spectroradiometer
PDF	Probability Density Function
RegCM4	Regional Climate Model version 4
SUBEX	Subgrid Explicit Moisture Scheme SUBEX
TOA	Top of the Atmosphere

Variables

C	=	cloud Fraction
D	=	Detrainment input from the convection scheme
e	=	Partial pressure of water vapour
e_s	=	Saturation vapour pressure
e_{sw}	=	Saturated vapour pressure with respect to water
e_{si}	=	Saturated vapour pressure with respect to ice
G	=	Gibbs free energy
H	=	Enthalpy
p	=	pressure
P	=	precipitation rate
P_{loc}	=	local precipitation rate
q_{sat}	=	Saturation mixing ratio
q_v	=	grid-mean specific humidity (kg kg^{-1})
q_c	=	grid-mean specific cloud liquid water content (kg kg^{-1})
q_r	=	grid-mean specific precipitating rain water content (kg kg^{-1})
q_i	=	grid-mean specific cloud ice water content (kg kg^{-1})
q_s	=	grid-mean specific precipitating snow water content (kg kg^{-1})
q_{sat}	=	saturation specific humidity (kg kg^{-1})
q_e	=	environmental specific humidity (kg kg^{-1})
q_v	=	grid-mean specific humidity (kg kg^{-1})
q_l	=	grid-mean specific cloud liquid water content (kg kg^{-1})
q_l^{cld}	=	in-cloud specific cloud liquid water content (kg kg^{-1})
q_i^{cld}	=	in-cloud specific ice water content (kg kg^{-1})
RH	=	Relative Humidity
S	=	Entropy
T	=	Temperature
T_L	=	liquid water temperature
ρ	=	density of moist air (kg m^{-3})
ρ_l	=	density of cloud water (kg m^{-3})
ρ_{rain}	=	density of rain in air (kg m^{-3})
ω	=	mean grid-box vertical velocity

Parameters

α_l	=	Specific volume of liquid water
α_i	=	Specific volume of ice
c_P	=	specific heat at constant pressure
D	=	Diffusion coefficient for water vapour
ϵ	=	R_d/R_v
L_f	=	latent heat of fusion
L_s	=	latent heat of sublimation
L_v	=	latent heat of vaporization
M_s	=	Mass of the solute
m_s	=	Molecular weight of the solute
M_w	=	Mass of the water
m_w	=	Molecular weight of the water
N_0	=	Avogadro's number
N_{tot}	=	Total number of molecules
N_l	=	Number of molecules of liquid
μ_v	=	Free Gibbs energy per molecule of water vapour
μ_l	=	Free Gibbs energy per molecule of liquid
R_d	=	Gas constant for dry air
R_v	=	Gas constant for water vapour
ρ_w	=	Density of water
ρ_v	=	Density of water vapour
p, α_0, γ	=	Constants used for the Cloud Cover parameterization
RH_{crit}	=	threshold value of the relative humidity
RH_{homo}	=	threshold relative humidity for homogeneous nucleation
T_0	=	273.16K
T_{ice}	=	250.16K
T_{melt}	=	0°C

Bibliography

Andrews, T., Gregory, J., Webb, M., and Taylor, K. (2012b). Forcing, feedbacks and climate sensitivity in cmip5 coupled atmosphere-ocean climate models. *Geophysical Research Letters*, 39(9).

Anthes, R. (1977). A cumulus parameterization scheme utilizing a one-dimensional cloud model. *Mon. Wea. Rev.*, 105:270–286.

Barkstrom, B. and Smith, G. (1986). The earth radiation budget experiment: Science and implementation. *Rev. Geophys.*, 24(2):379–390.

Beheng, K. (1994). A parameterization of warm cloud microphysical conversion processes. *Atmos. Res.*, 33:193–206.

Bodas-Salcedo, A., Webb, M., Bony, S., Chepfer, H., Dufresne, J.-L., Klein, S., Zhang, Y., Marchand, R., Haynes, J., Pincus, R., et al. (2011). Cosp: Satellite simulation software for model assessment. *Bulletin of the American Meteorological Society*, 92(8):1023–1043.

Bodas-Salcedo, A., Webb, M., Brooks, M., Ringerand, M., Williams, K., Milton, S., and Wilson, D. (2008). Evaluating cloud systems in the met office global forecast model using simulated cloudsat radar reflectivities. *Journal of Geophysical Research: Atmospheres (1984–2012)*, 113(D8).

Bony, S. and Dufresne, J.-L. (2005). Marine boundary layer clouds at the heart of tropical cloud feedback uncertainties in climate models. *Geophysical Research Letters*, 32(20).

Bony, S., Lau, K., and Sud, Y. (1997). Sea surface temperature and large-scale circulation influences on tropical greenhouse effect and cloud radiative forcing. *J. Climate*, 10:2055–2077.

Bretherton, C., McCaa, J., and Grenier, H. (2004). A new parameterization for shallow cumulus convection and its application to marine subtropical cloud-topped boundary layers. part i: Description and 1d results. *Monthly weather review*, 132(4):864–882.

Budyko, M. (1969). The effect of solar radiation variations on the climate of the earth. *Tellus*, 21:611–619.

Cess, R., Zhang, M., Ingram, W., Potter, G., Alekseev, V., Barker, H., Cohen-Solal, E., Colman, R., Dazlich, D., Genio, A. D., et al. (1996). Cloud feedback in atmospheric general circulation models: An update. *Journal of Geophysical Research: Atmospheres (1984–2012)*, 101(D8):12791–12794.

Charney, J., Arakawa, A., Baker, F., Bolin, B., Dickinson, R., Goody, R., Leith, C., Stommel, H., and Wunsch, C. (1979). *Carbon dioxide and climate: a scientific assessment.* Washington, DC: National Academy of Sciences Press.

Chepfer, H., Bony, S., Winker, D., Cesana, G., Dufresne, J., Minnis, P., Stubenrauch, C., and Zeng, S. (2010). The GCM-Oriented CALIPSO Cloud Product (CALIPSO-GOCCP). *Journal of Geophysical Research: Atmospheres (1984–2012)*, 115(D4).

Chepfer, H., Bony, S., Winker, D., Chiriaco, M., Dufresne, J.-L., and Sèze, G. (2008). Use of calipso lidar observations to evaluate the cloudiness simulated by a climate model. *Geophysical Research Letters*, 35(15).

Davis, M. and Sartor, J. (1967). Theoretical collision efficiencies for small cloud droplets in stokes flow.

Dee, D., Uppala, S., Simmons, A., Berrisford, P., Poli, P., Kobayashi, S., Andrae, U., Balmaseda, M., Balsamo, G., Bauer, P., et al. (2011). The era-interim reanalysis: Configuration and performance of the data assimilation system. *Quarterly Journal of the Royal Meteorological Society*, 137(656):553–597.

DelGenio, A., Yao, M., Kovari, W., and Lo, K. (1996). A prognostic cloud water parameterization for global climate models. *J. Climate*, 9:270–304.

Dickinson, R., Henderson-Sellers, A., and Kennedy, P. (1993a). *Biosphere-atmosphere transfer scheme (bats) version 1e as coupled to the ncar community climate model*. Tech. Rep., National Center for Atmospheric Research.

Dickinson, R., Henderson-Sellers, A., and Wilson, M. (1986). *Biosphere-atmosphere transfer scheme (bats) for the ncar community climate model*. Tech. Rep. NCARE/TN-275+STR, National Center for Atmospheric Research.

Dickinson, R., Kennedy, P., and Henderson-Sellers, A. (1993b). *Biosphere-atmosphere transfer scheme (BATS) version 1e as coupled to the NCAR community climate model*. National Center for Atmospheric Research, Climate and Global Dynamics Division.

Diner, D., Beckert, J., Reilly, T., Bruegge, C., Conel, J., Kahn, R., Martonchik, J., Ackerman, T., Davies, R., Gerstl, S., Siegfried, A., et al. (1998). Multi-angle imaging spectroradiometer (misr) instrument description and experiment overview. *Geoscience and Remote Sensing, IEEE Transactions on*, 36(4):1072–1087.

Diro, G., Tompkins, A., Giorgi, F., and Bonaventura, L. (2013). Implementation of a semi-lagrangian scheme for water vapour and tracer advection in regcm4. In *EGU General Assembly Conference Abstracts*, volume 15, page 6184.

Dufresne, J.-L. and Bony, S. (2008). An assessment of the primary sources of spread of global warming estimates from coupled atmosphere-ocean models. *Journal of Climate*, 21(19):5135–5144.

Ellis, J. (1978). Cloudiness, the planetary radiation budget, and climate.

Emanuel, K. (1991). A scheme for representing cumulus convection in large-scale models. *J. Atmos. Sci.*, 48:2313â–2335.

Emanuel, K. and Zivkovic-Rothman, M. (1999). Development and evaluation of a convection scheme for use in climate models. *J. Atmos. Sci.*, 56:1766–ĂŞ1782.

Forbes, R. M., Tompkins, A. M., and Untch, A. (2011). *A New Prognastic Bulk Microphysics Scheme for the IFS*. European Centre for Medium-Range Weather Forecasts.

Fowler, L., Randall, D., and Rutledge, S. (1996). Liquid and ice cloud microphysics in the CSU general circulation model. Part I: Model description and simulated cloud microphysical processes. *J. Climate*, 9:489–529.

Franklin, C., Sun, Z., Bi, D., Dix, M., Yan, H., and Bodas-Salcedo, A. (2013). Evaluation of clouds in access using the satellite simulator package cosp: Global, seasonal, and regional cloud properties. *Journal of Geophysical Research: Atmospheres*, 118(2):732–748.

Gates, W. and Schlesinger, M. (1977). Numerical-simulation of January and July global climate with a two-level atmospheric model. *J. Atmos. Sci.*, 34:36–76.

Ghan, S. J., Leung, L. R., Easter, R. C., and Abdul-Razzak, H. (1997). Prediction of cloud droplet number in a general circulation model. *Journal of Geophysical Research: Atmospheres (1984–2012)*, 102(D18):21777–21794.

Giorgi, F., Coppola, E., Solmon, F., Mariotti, L., Sylla, M., Bi, X., Elguindi, N., Diro, G., Nair, V., Giuliani, G., Turuncoglu, U., Cozzini, S., Güttler, I., O'Brien, T., Tawfik, A., Shalaby, A., Zakey, A., Steiner, A., Stordal, F., Sloan, L., and Brankovic, C. (2012). RegCM4: model description and preliminary tests over multiple CORDEX domains. *Climate Res.*, 2(7).

Grell, G. (1993). Prognostic evaluation of assumptions used by cumulus parameterizations. *Mon. Wea. Rev.*, 121:764–787.

Grell, G., Dudhia, A., and Stauffer, D. (1994). *Description of the fifth generation Penn State/NCAR Mesoscale Model(MM5)*. Tech. Rep. TN-398+STR, NCAR, Boulder, Colorado.

Hartmann, D. L., Dennis, L., and Doelling, D. (1991). On the net radiative effectiveness of clouds. *J. Geophys. Res.*, 96:869–891.

Heymsfield, A. J. and Iaquinta, J. (2000). Cirrus crystal terminal velocities. *Journal of the Atmospheric Sciences*, 57(7):916–938.

Hogan, R. J. and Illingworth, A. J. (2000). Deriving cloud overlap statistics from radar. *Quarterly Journal of the Royal Meteorological Society*, 126(569):2903–2909.

Holloway, J. and Manabe, S. (1971). Simulation of climate by a global general circulation model: I. Hydrologic cycle and heat balance. *Mon. Wea. Rev.*, 99:335–370.

Holtslag, A. A. M., M., E. I. F. d. B., and Pan, H.-L. (1990). A high resolution air mass transformation model for shortrange weather forecasting. *Mon. Wea. Rev.*, 118:1561–1575.

Hulme, M. (2001). Climatic perspectives on sahelian desiccation: 1973–1998. *Global Environmental Change*, 11(1):19–29.

Kärcher, B. and Lohmann, U. (2002). A parameterization of cirrus cloud formation: Homogeneous freezing of supercooled aerosols. *J. Geophys. Res.*, 107:10.

Kashchiev, D. (2000). *Nucleation*. Butterworth-Heinemann.

Kessler, E. (1969). On the distribution and continuity of water substance in atmospheric circulation. *Meteor. Monogr.*, 32:84.

Khairoutdinov, M. and Kogan, Y. (2000). A new cloud physics parameterization in a large-eddy simulation model of marine stratocumulus. *Bull. Amer. Meteor. Soc.*, 128:229–243.

Kiehl, J., Hack, J., Bonan, G., Boville, B., Breigleb, B., Williamson, D., , and Rasch, P. (1996). *Description of the NCAR community climate model (CCM3),*. Tech. Rep. NCAR/TN-420+STR, National Center for Atmospheric Research.

King, M., Menzel, W., Kaufman, Y., Tanré, D., Gao, B.-C., Platnick, S., Ackerman, S., Remer, L., Pincus, R., and Hubanks, P. (2003). Cloud and aerosol properties, precipitable water, and profiles of temperature and water vapor from modis. *Geoscience and Remote Sensing, IEEE Transactions on*, 41(2):442–458.

Klein, S. and Hartmann, D. (1993). The seasonal cycle of low stratiform clouds. *Journal of Climate*, 6(8):1587–1606.

Klein, S. and Jakob, C. (1999). Validation and sensitivities of frontal clouds simulated by the ecmwf model. *Monthly Weather Review*, 127(10):2514–2531.

Koop, T., Luo, B., Tsias, A., and Peter, T. (2000). Water activity as the determinant for homogeneous ice nucleation in aqueous solutions. *Nature*, 406:611–614.

Levkov, L., Rockel, B., Kapitza, H., and Raschke, E. (1992). 3d mesoscale numerical studies of cirrus and stratus clouds by their time and space evolution. *Contributions to atmospheric physics*, 65(1):35–58.

Lin, W. and Zhang, M. (2004). Evaluation of clouds and their radiative effects simulated by the ncar community atmospheric model against satellite observations. *Journal of climate*, 17(17):3302–3318.

Lin, Y., Farley, R., and Orville, H. (1983). Bulk parameterization of the snow field in a cloud model. *J. Appl. Meteor. Clim*, 22:1065–1092.

Liu, Y. and Daum, P. (2004). Parameterization of the autoconversion process. part I: Analytical formulation of the Kessler-type parameterizations. *J. Atmos. Sci.*, 61:1539–1548.

Lohmann, U., McFarlane, N., L. Levkov, L., Abdella, K., and Albers, F. (1999). Comparing different cloud schemes of a single column model by using mesoscale forcing and nudging technique. *Journal of climate*, 12(2):438–461.

Lohmann, U. and Roeckner, E. (1996). Design and performance of a new cloud microphysics scheme developed for the echam general circulation model. *Climate Dynamics*, 12(8):557–572.

London, J. (1957). *A study of the atmospheric heat balance*. New York Univeristy College of Engineering, New York, N.Y. (Available from the National Technical Information Service, Springfield, Va.).

Marchand, R., Ackerman, T., Smyth, M., and Rossow, W. (2010). A review of cloud top height and optical depth histograms from misr, isccp, and modis. *Journal of Geophysical Research: Atmospheres (1984–2012)*, 115(D16).

Meehl, G., Washington, W., Arblaster, J., and Hu, A. (2004). Factors affecting climate sensitivity in global coupled models. *Journal of Climate*, 17(7):1584–1596.

Menzel, W. P., Frey, R., Zhang, H., Wylie, D., Moeller, C., Holz, R., Maddux, B., Baum, B., Strabala, K., and Gumley, L. (2008). Modis global cloud-top pressure and amount estimation: Algorithm description and results. *Journal of Applied Meteorology and Climatology*, 47(4):1175–1198.

Meyers, M., Walko, R., Harrington, J., and Cotton, W. (1997). New rams cloud microphysics parameterization. part ii: The two-moment scheme. *Atmospheric Research*, 45(1):3–39.

Milbrandt, J. and Yau, M. (2005). A multimoment bulk microphysics parameterization. part i: Analysis of the role of the spectral shape parameter. *Journal of the atmospheric sciences*, 62(9):3051–3064.

Morrison, H., Curry, J., and Khvorostyanov, V. (2005). A new double-moment microphysics parameterization for application in cloud and climate models. part i: Description. *Journal of the atmospheric sciences*, 62(6):1665–1677.

Morrison, H. and Gettelman, A. (2008). A new two-moment bulk stratiform cloud microphysics scheme in the community atmosphere model, version 3 (cam3). part i: Description and numerical tests. *Journal of Climate*, 21(15):3642–3659.

Muller, J.-P., Mandanayake, A., Moroney, C., Davies, R., Diner, D., and Paradise, S. (2002). Misr stereoscopic image matchers: Techniques and results. *Geoscience and Remote Sensing, IEEE Transactions on*, 40(7):1547–1559.

Murray, F. (1967). On the computation of saturation vapor pressure. *J. Appl. Meteor.*, 6:203–204.

Naud, C., Muller, J.-P., and Clothiaux, E. (2002). Comparison of cloud top heights derived from misr stereo and modis co2-slicing. *Geophysical Research Letters*, 29(16):42–1.

Neale, R. and Slingo, J. (2003). The maritime continent and its role in the global climate: A gcm study. *Journal of Climate*, 16(5):834–848.

Oleson, K. (2008). Improvements to the Community Land Model and their impact on the hydrological cycle. *J. Geophys. Res. Biogeosci.*, 113:.

Ose, T. (1993). An examination of the effects of explicit cloud water in the UCLA GCM. *J. Meteor. Soc. of Japan*, 71:93–109.

Pal, J., Small, E., and Eltahir, E. (2000). Simulation of regional-scalewater and energy budgets: representation of subgridcloud and precipitation processes within RegCM. *J. Geophys. Res.*, 105:29579–29594.

Pincus, R. and Klein, S. (2000). Unresolved spatial variability and microphysical process rates in largescale models. *J. Geophys. Res.*, 105:27059–27065.

Pincus, R., Platnick, S., Ackerman, S. A., Hemler, R. S., and Hofmann, R. (2012). Reconciling simulated and observed views of clouds: Modis, isccp, and the limits of instrument simulators. *Journal of Climate*, 25(13):4699–4720.

Platnick, S., King, M., Ackerman, S., Menzel, W., Baum, B., Riédi, J., and Frey, R. (2003). The modis cloud products: Algorithms and examples from terra. *Geoscience and Remote Sensing, IEEE Transactions on*, 41(2):459–473.

Ramanathan, V. (1976). Radiative transfer within the earth's troposphere and stratosphere: A simplified radiative-convective model. *J. Atmos. Sci.*, 33:1330–1346.

Ramanathan, V. (1987). The role of Earth Radiation Budget studies in climate and general-circulation research. *J. Geophys. Res.*, D4:4075–4095.

Ramanathan, V., Cess, R., Harrison, E., Minnis, P., Barkstrom, B., Ahmad, E., and Hartmann, D. (1989). Cloud-radiative forcing and climate: Results from the earth radiation budget experiment. *Science*, 243(4887):57–63.

Randall, D., Fichefet, T., et al. (2007). Climate models and their evaluation.

Randall, D., Harshvardhan, D., Dazlich, D., and Corsetti, T. (1989). Interactions among radiation, convection, and large-scale dynamics in a general-circulation model. *J. Atmos. Sci.*, 46:1943–1970.

Randel, D., Greenwald, T., Vonder Haar, T., Stephens, G., Ringerud, M., and Combs, C. (1996). A new global water vapor dataset. *Bulletin of the American Meteorological Society*, 77(6):1233–1246.

Reisner, J., Rasmussen, R., and Bruintjes, R. (1998). Explicit forecasting of supercooled liquid water in winter storms using the mm5 mesoscale model. *Quarterly Journal of the Royal Meteorological Society*, 124(548):1071–1107.

Rogers, R. and Yau, M. (1989). *A Short Course in Cloud Physics*. 3d ed. Pergamon Press.

Rossow, W., Beuschel, D., and Roiter, M. (1996). International Satellite Cloud Climatology Project (ISCCP) documentation of new cloud datasets. *World Climate Research Programme, NASA, Goddard Institute of Space Studies*, page 15.

Rossow, W. and Schiffer, R. (1999). Advances in understanding clouds from isccp. *Bulletin of the American Meteorological Society*, 80(11):2261–2287.

Rotstayn, L. (1997). A physically based scheme for the treatment of stratiform clouds and precipitation in large-scale models. i: Description and evaluation of the microphysical processes. *Quarterly Journal of the Royal Meteorological Society*, 123(541):1227–1282.

Rotstayn, L., Ryan, B., and Katzfey, J. (2000). A scheme for calculation of the liquid fraction in mixed-phase stratiform clouds in large-scale models. *Mon. Wea. Rev.*, 128:1070–1088.

Rutledge, S. and Hobbs, P. (1983). The mesoscale and microscale structure and organization of clouds and precipitation in midlatitude cyclones. viii: A model for the seeder-feeder process in warm-frontal rainbands. *Journal of the Atmospheric Sciences*, 40(5):1185–1206.

Ryan, B., Wishart, E., and Shaw, D. (1976). The growth rates and densities of ice crystals between-3 c and-21 c. *Journal of the Atmospheric Sciences*, 33:842–850.

Schaaf, C., Gao, F., Strahler, A., Lucht, W., Li, X., Tsang, T., Strugnell, N., Zhang, X., Jin, Y., Muller, J.-P., et al. (2002). First operational brdf, albedo nadir reflectance products from modis. *Remote sensing of Environment*, 83(1):135–148.

Schneider, S. (1972). Cloudiness as a Global Climatic Feedback Mechanism: The Effects on the Radiation Balance and Surface Temperature of Variations in Cloudiness. *J. Atmos. Sci.*, 29:1413–1422.

Seifert, A. and Beheng, K. D. (2001). A double-moment parameterization for simulating autoconversion, accretion and selfcollection. *Atmospheric research*, 59:265–281.

Sellers, W. (1976). A two-dimensional global climatic model. *Mon. Wea. Rev.*, 104:233–248.

Simmons, A., Uppala, S., Dee, D., and Kobayashi, S. (2007). Era-interim: New ecmwf reanalysis products from 1989 onwards. *ECMWF newsletter*, 110(110):25–35.

Slingo, J. (1980). A cloud parametrization scheme derived from GATE data for use with a numerical-model. *Q. J. R. Meteorol. Soc.*, 106:747–770.

Slingo, J. (1989). A gcm parameterization for the shortwave radiative properties of water clouds. *J. Atmos. Sci.*, 46:1419–1427.

Smagorinsky, J. (1960). *On the Dynamical Prediction of Large-Scale Condensation by Numerical Methods*. Physics of Precipitation: Proceedings of the Cloud Physics Conference, Woods Hole, Massachusetts, June 3-5, 1959, Wiley Online Library.

Smagorinsky, J., Manabe, S., and Holloway, J. (1965). Numerical results from a nine-level general circulation model of the atmosphere 1. *Mon. Wea. Rev.*, 93:727–768.

Smith, R. (1990). A scheme for predicting layer clouds and their water-content in a general-circulation model. *Q. J. R. Meteorol. Soc.*, 116:435–460.

Somerville, R. and Remer, L. (1984). Cloud optical thickness feedbacks in the CO2 climate problem. *J. Geophys. Res.*, 89:9668–9672.

Stephens, G., Vane, D., Boain, R., Mace, G., Sassen, K., Wang, Z., Illingworth, A., O'Connor, E., Rossow, W., Durden, S., et al. (2002). The cloudsat mission and the a-train: A new dimension of space-based observations of clouds and precipitation. *Bulletin of the American Meteorological Society*, 83(12):1771–1790.

Stevens, B., Feingold, G., Cotton, W., and Walko, R. (1996). Elements of the microphysical structure of numerically simulated nonprecipitating stratocumulus. *Journal of the atmospheric sciences*, 53(7):980–1006.

Sundqvist, H. (1978). A parameterization scheme for non-convective condensation including prediction of cloud water content. *Q. J. R. Meteorol. Soc.*, 104:677–690.

Sundqvist, H., Berge, E., and Kristjansson, J. (1989). Condensation and cloud parameterization studies with a mesoscale numerical weather prediction model. *Mon. Wea. Rev.*, 117:1641–1657.

Tabazadeh, A., Martin, S., and Lin, J.-S. (2000). The effect of particle size and nitric acid uptake on the homogeneous freezing of aqueous sulfuric acid particles. *Geophysical research letters*, 27:1111–1114.

Tiedtke, M. (1989). A comprehensive mass flux scheme for cumulus parameterization on large scale models. *Mon. Wea. Rev.*, 117:1779–1800.

Tiedtke, M. (1991). *Aspects of cumulus parametrization.* Proc. ECMWF Seminar on Tropical Extra-Tropical Interactions, Reading, U.K.

Tiedtke, M. (1993). Representation of clouds in large-scale models. *Mon. Wea. Rev.*, 121:3040–3061.

Tompkins, A. (2002). A prognostic parameterization for the subgrid-scale variability of water vapour and clouds in large- scale models and its use to diagnose cloud cover. *Journal of the atmospheric sciences*, 59(12):1917–1942.

Tompkins, A. (2005). The parameterization of cloud cover. *ECMWF Technical Memorandum*, pages 1–25.

Tompkins, A. (2007). Ice supersaturation in the ECMWF integrated forecast system. *Q. J. R. Meteorol. Soc.*, 133:53–63.

Tompkins, A. and Di Giuseppe, F. (2007). Generalizing cloud overlap treatment to include solar zenith angle effects on cloud geometry. *Journal of the atmospheric sciences*, 64(6):2116–2125.

Vial, J., Dufresne, J.-J., and Bony, S. (2013). On the interpretation of inter-model spread in cmip5 climate sensitivity estimates. *Climate dynamics*, 41(11-12):3339–3362.

Wang, P. (2013). *Physics and dynamics of clouds and precipitation*. Cambridge University Press.

Webb, M., Senior, C., Bony, S., and Morcrette, J.-J. (2001). Combining erbe and isccp data to assess clouds in the hadley centre, ecmwf and lmd atmospheric climate models. *Climate Dynamics*, 17(12):905–922.

Wetherald, R. and Manabe, S. (1980). Cloud cover and climate sensitivity. *J. Atmos. Sci.*, 37:1485–1510.

Williams, K., Ringer, M., and Senior, C. (2003). Evaluating the cloud response to climate change and current climate variability. *Climate Dynamics*, 20(7-8):705–721.

Williams, K. and Tselioudis, G. (2007). Gcm intercomparison of global cloud regimes: Present-day evaluation and climate change response. *Climate dynamics*, 29(2-3):231–250.

Williams, K. and Webb, M. (2009). A quantitative performance assessment of cloud regimes in climate models. *Climate dynamics*, 33(1):141–157.

Wilson, D. and Ballard, S. (1999). A microphysically based precipitation scheme for the uk meteorological office unified model. *Quarterly Journal of the Royal Meteorological Society*, 125:1607–1636.

Winker, D., Pelon, J., Coakley, J. J., Ackerman, S., Charlson, R., Colarco, P., Flamant, P., Fu, Q., Hoff, R., Kittaka, C., et al. (2010). The calipso mission: A global 3d view of aerosols and clouds.

Xu, K. and Randall, D. (1996). A semiempirical cloudiness parameterization for use in climate models. *J. Atmos. Sci.*, 53:3084–3102.

Yu, W., Doutriaux, M., Sèze, G., Le Treut, H., and Desbois, M. (1996). A methodology study of the validation of clouds in gcms using isccp satellite observations. *Climate dynamics*, 12(6):389–401.

Zelinka, M., Klein, S., Taylor, K., Andrews, T., Webb, M., Gregory, J., and Forster, P. (2013). Contributions of different cloud types to feedbacks and rapid adjustments in cmip5. *Journal of Climate*, (2013).

Zhang, M., Lin, W., Klein, S., Bacmeister, J., Bony, S., Cederwall, R., Del Genio, A., Hack, J., Loeb, N., Lohmann, U., et al. (2005). Comparing clouds and their seasonal variations in 10 atmospheric general circulation models with satellite measurements. *Journal of Geophysical Research: Atmospheres (1984–2012)*, 110(D15).